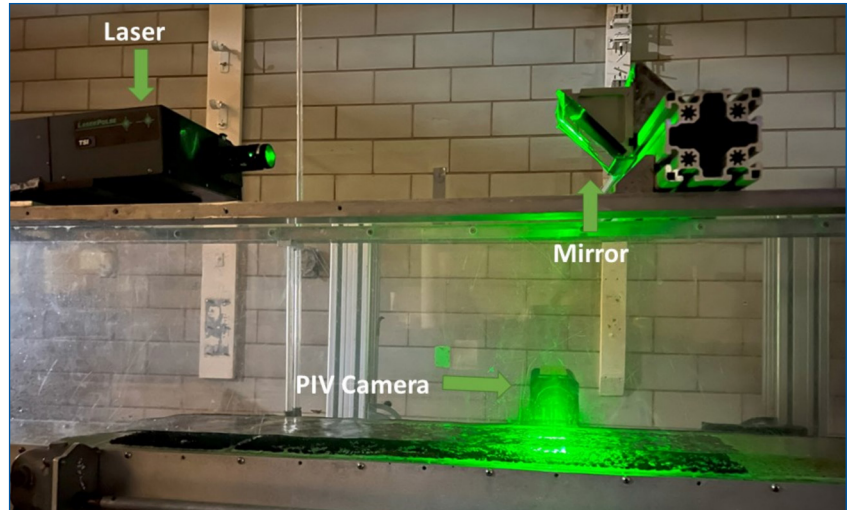# MOUNTAIN-PLAINS CONSORTIUM

MPC 24-567 | M.F. Jamil, F. Ting, and M. Kafle

RESPONSE OF BED
SHEAR STRESS IN OPEN-
CHANNEL FLOW TO A
SUDDEN CHANGE IN BED
ROUGHNESS

MOUNTAIN-PLAINS
CONSORTIUM REGION 8

1. Report No. MPC-688	2. Government Accession No.	3. Recipient's Catalog No.
4. Title and Subtitle Response of Bed Shear Stress in Open-Channel Flow to a Sudden Change in Bed Roughness		5. Report Date October 2024
		6. Performing Organization Code
7. Author(s) Muhammad Farrukh Jamil, M.S. Francis C.K. Ting, Ph.D., P.E. Monika Kafle, Graduate Research Assistant		8. Performing Organization Report No. MPC 24-567
9. Performing Organization Name and Address South Dakota State University Department of Civil & Environmental Engineering Crothers Engineering Hall 301 Brookings, SD 57007		10. Work Unit No. (TRAIS)
		11. Contract or Grant No.
12. Sponsoring Agency Name and Address Mountain-Plains Consortium North Dakota State University PO Box 6050, Fargo, ND 58108		13. Type of Report and Period Covered Final Report
		14. Sponsoring Agency Code

15. Supplementary Notes

Supported by a grant from the US DOT, University Transportation Centers Program

16. Abstract

The determination of bed shear stress plays a pivotal role in understanding the fluid dynamics in both natural and engineered channels. The commonly employed logarithmic law provides a mathematical formula to compute the bed shear stress in open-channel flows. However, its applicability in flow through transition remains relatively unexplored. In this study, laboratory experiments were conducted on smooth-to-rough (STR) and rough-to-smooth (RTS) transitions in an open-channel flume under different composite water surface profiles. The velocity field was measured along the channel centerline using a particle image velocimetry (PIV) system. The bed shear stress was determined from the measured velocity profile and water depth using various methods. The primary objective was to investigate the effects of bed roughness and water surface profile on the variation of bed shear stress in gradually varied flows through the transition. It was found that the evolution of bed shear stress was related to both water surface profile and bed roughness. In both RTS and STR transitions, the bed shear stress adjusted to the new bed condition almost immediately even though the velocity profile away from the bed was still evolving. Unlike external and close-conduit flows, however, the bed shear stress in free-surface flows was also affected by the local water depth and thus the composite water surface profile created by the channel transition. The bed shear stress development closely followed the variation in local water depth, ultimately reaching equilibrium condition when the flow depth became uniform. It was also found that the choice of displacement height of the mean velocity profile played an important role in determining the bed shear stress on a rough bed using the logarithmic law, and thus the development of bed shear stress in STR transitions.

17. Key Word anemometers, channels (waterways), flow, roughness, shear stress	18. Distribution Statement Public distribution		
19. Security Classif. (of this report) Unclassified	20. Security Classif. (of this page) Unclassified	21. No. of Pages 98	22. Price n/a

Form DOT F 1700.7 (8-72)   Reproduction of completed page authorized

Response of Bed Shear Stress in Open-Channel Flow
to a Sudden Change in Bed Roughness

Muhammad Farrukh Jamil, M.S.
Francis C. K. Ting, Ph.D., P.E.
Monika Kafle

Department of Civil and Environmental Engineering
South Dakota State University
Brookings, SD 57007

October 2024

Acknowledgements

Disclaimer

The contents of this report reflect the views of the authors, who are responsible for the facts and the accuracy of the data presented. This document is disseminated under the sponsorship of the Department of Transportation, University Transportation Centers Program, in the interest of information exchange. The U.S. Government assumes no liability for the contents or use thereof.

ABSTRACT

The determination of bed shear stress plays a pivotal role in understanding the fluid dynamics in both natural and engineered channels. The commonly employed logarithmic law provides a mathematical formula to compute the bed shear stress in open-channel flows. However, its applicability in flow through transition remains relatively unexplored. In this study, laboratory experiments were conducted on smooth-to-rough (STR) and rough-to-smooth (RTS) transitions in an open-channel flume under different composite water surface profiles. The velocity field was measured along the channel centerline using a particle image velocimetry (PIV) system. The bed shear stress was determined from the measured velocity profile and water depth using various methods. The primary objective was to investigate the effects of bed roughness and water surface profile on the variation of bed shear stress in gradually varied flows through the transition. It was found that the evolution of bed shear stress was related to both water surface profile and bed roughness. In both RTS and STR transitions, the bed shear stress adjusted to the new bed condition almost immediately even though the velocity profile away from the bed was still evolving. Unlike external and close-conduit flows, however, the bed shear stress in free-surface flows was also affected by the local water depth and thus the composite water surface profile created by the channel transition. The bed shear stress development closely followed the variation in local water depth, ultimately reaching equilibrium condition when the flow depth became uniform. It was also found that the choice of displacement height of the mean velocity profile played an important role in determining the bed shear stress on a rough bed using the logarithmic law, and thus the development of bed shear stress in STR transitions.

TABLE OF CONTENTS

LIST OF FIGURES

LIST OF TABLES

1.   INTRODUCTION

Flow over a sudden change in surface roughness has been studied mostly in external (e.g., atmospheric boundary layer) and close-conduit (e.g., wind tunnel) flows. A recent literature review can be found in Kadivar et al. (2021). When a flow encounters a sudden change in surface roughness, an internal boundary layer (IBL) will start at the roughness transition and grow outward from the wall with distance downstream. If the surface downstream is of sufficient length, a new fully developed turbulent boundary layer will eventually be established. Previous studies have shown that the wall shear stress would attain its new equilibrium value almost immediately, but flow quantities outside the internal boundary layer are determined by conditions before the transition and will change only gradually with distance downstream. In a rough-to-smooth (RTS) transition, for example, experimental and numerical studies have found that the wall shear stress would be underestimated if determined from the mean velocity profile measured outside the internal boundary layer using the logarithmic law (e.g., Antonia and Luxton, 1972; Loureiro et al., 2010; Li et al., 2019).

Free-surface flows with a sudden change in bed roughness are much less well understood compared with external and close-conduit flows. Chen and Chiew (2003) measured the mean velocity, turbulence intensity, and Reynolds stress profiles in an open channel with a sudden change from a smooth bed to a rough bed. They determined the bed shear stress and equivalent bed roughness by fitting the logarithmic law to the measured velocity profile. They found that the equivalent roughness height and bed shear stress increase gradually and take a transitional length of approximately five to six times the flow depth to reach the equilibrium condition downstream. Lee (2018) modeled the laboratory experiment by Chen and Chiew (2003) using the computational fluid dynamics (CFD) model OpenFOAM. His numerical results show a sharp increase in bed shear stress after a sudden transition in bed roughness in contrast to the experimental data by Chen and Chiew (2003). He suggested that the logarithmic law may not be used to compute the bed shear stress under transitional flow condition because the velocity profile outside the IBL is not in equilibrium. Most recently, Rathore et al. (2022) measured the turbulence characteristics due to a sudden change from a smooth bed to a rough bed in open-channel flow using a particle image velocity (PIV) system. They found that the Reynolds stress and turbulence intensity increase with streamwise distance on the rough bed. They estimated the bed shear stress by extending the measured Reynolds stress distribution to the bed surface. They concluded that the bed shear stress does not change abruptly at the roughness transition. In both Chen and Chiew (2003) and Rathore et al. (2022), the flows were subcritical and the bed transitions were from smooth to rough (STR).

Figure 1.1 shows the types of composite water surface profiles that can develop near a channel transition. The different scenarios are often described in hydraulic engineering textbooks for two channels that are identical except for the slope (e.g., Akan, 2006), but the same flow conditions can also be produced by a sudden change in bed roughness. Five different cases (A to E) can be distinguished. When channel 1 is "mild" and channel 2 is "steep," an M2 curve will develop before the transition and an S2 profile will occur in channel 2 (case A). However, if channel 1 is "milder" and channel 2 is "mild" the water surface profile will change immediately from an M2 curve to uniform depth at the transition (case C). Because the flow velocity adjacent to the bed must constantly adjust to the growth of the internal boundary layer, while the flow depth varies according to the water surface profile, the evolution of velocity profile and bed shear stress downstream of a sudden change in bed roughness will be related to both the bed roughness and water surface profile. In both A and C cases, the flow velocity adjacent to the bed will increase after the transition due to the sudden decrease in bed roughness. While the flow velocity near the free surface must decrease in case C to maintain conservation of mass in a uniform depth, it may not happen in case A because the flow depth also decreases in channel 2 due to the S2 profile. Therefore, the evolution of velocity profile and bed shear

stress downstream of a sudden change in bed roughness is more complicated in open-channel flows than in external or close-conduit flows without a free surface.
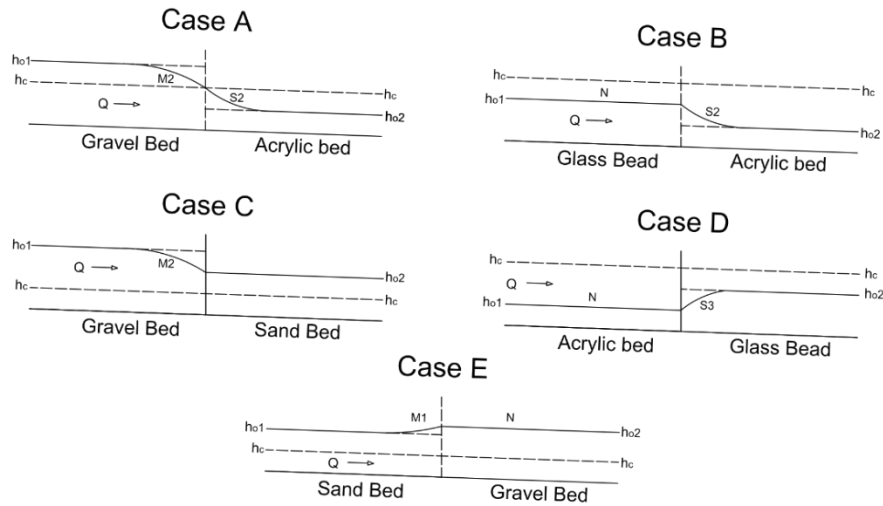
Figure 1.1 Composite water surface profiles in open-channel flows

The presence of composite water surface profiles involving both subcritical and supercritical flows produce flow conditions that are absent in external and close-conduit flows. In this study, laboratory experiments were conducted on smooth-to-rough (STR) and rough-to-smooth (RTS) transitions in an open-channel flume. The velocity field was measured along the centerline of the flume from upstream to downstream using a planar PIV system, and the bed shear stress was determined from the measured velocity profiles and water depths using various methods. The measured data were used to study the evolution of mean velocity profile and bed shear stress through the roughness transition.

2.   EXPERIMENTAL METHODS

2.1   Hydraulic Flume

The experiment was conducted in an A-8 hydraulic flume manufactured by Engineering Laboratory Design (ELD). The working channel was 0.15-m wide, 0.3-m deep, and 1.825-m long fabricated of 13-mm thick clear acrylic. The channel slope was continuously adjustable from 0% to 12% and measured using a digital inclinometer with a precision of $\pm 0.1\%$. The flow was delivered by a 0.5 HP, 1,750 RPM centrifugal pump with a maximum capacity of 5 L/s. The discharge was regulated by a gate value and measured using an orifice meter. Flow depth was controlled by a manually operated tailgate and measured using a point gate with a precision of ± 0.1 mm. Perforated metal screens and flow straighteners were installed in an entrance section before the working channel to dampen flow disturbances.
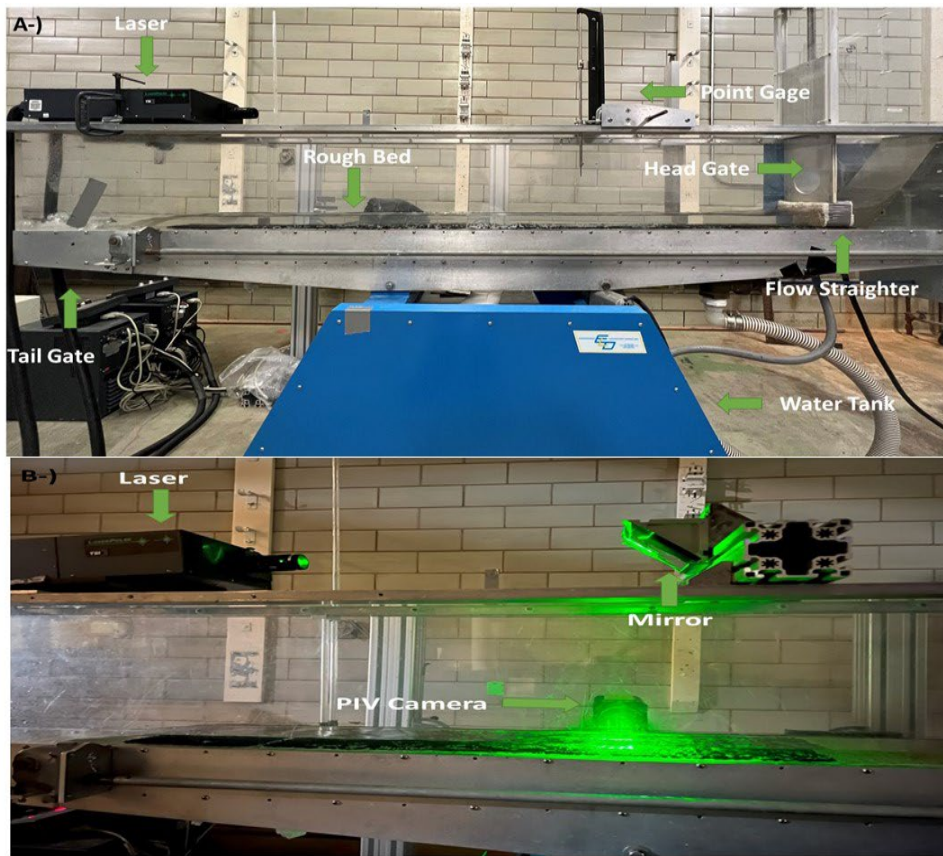
Figure 2.1 A-8 hydraulic flume (top plot) and setup of PIV system (bottom plot)

2.2   Particle Image Velocimetry (PIV) System

The PIV system was manufactured by TSI Incorporated. The system had been described in Ting (2006). Calibration of the PIV camera was conducted before the experiment at each measurement location by placing a calibration target (Figure 2.2) in the laser light sheet plane. An image of the calibration target was taken, and the calibration factor was determined by measuring the distance in pixels between the marker points. The field of view (FOV) was made parallel to the bottom by adjusting the slope of the camera mount before the experiment. The dimensions of the FOV changed

with the flow depth measured and varied from 12 mm × 12 mm to 28 mm × 28 mm. The corresponding image resolutions were about 12 and 28 µm/pixel, respectively.
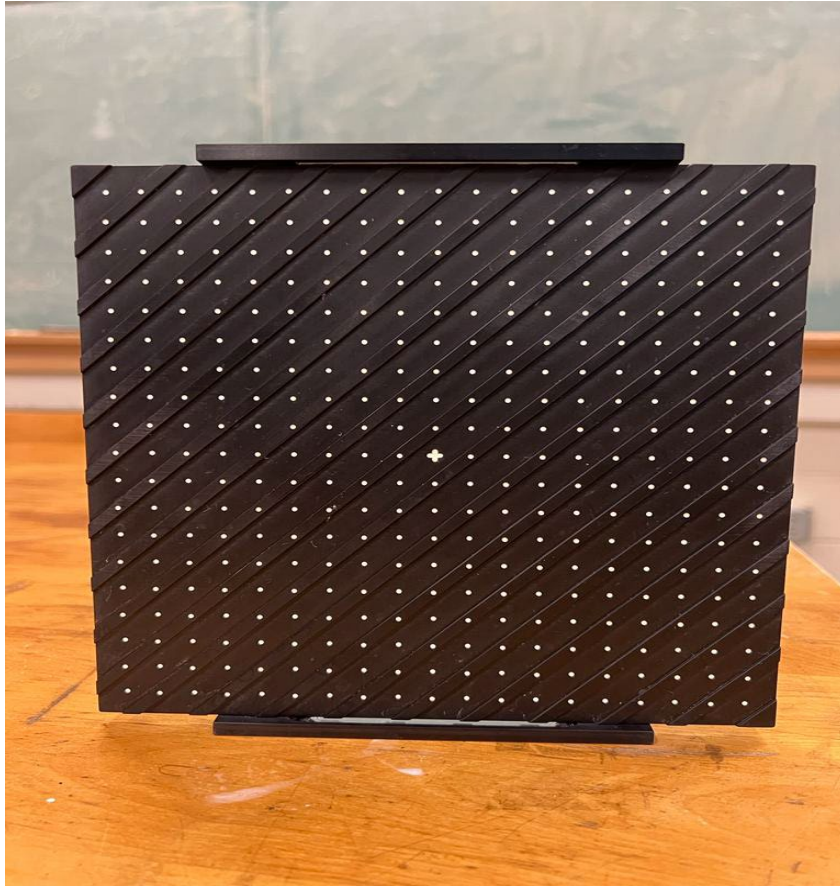
Figure 2.2 PIV calibration target

The flow was seeded with titanium dioxide particles (specific gravity 4.2, mean diameter 3.5 µm) and illuminated using a New Wave Dual Nd: YAG laser (120 mJ/pulse) operated in double pulse mode. The repetition rate was fixed at 10 Hz, but the time interval between straddled frames was varied based on the flow velocities measured to maximize the spatial resolution and minimize the measurement uncertainty. The laser was mounted on top of the flume. A light sheet about 1-mm thick was created using a cylindrical lens and a focusing lens mounted on the laser head. A first surface mirror mounted in front of the laser (Figure 2.1) re-directed the light sheet downward through the water surface to illuminate the measurement area in front of the PIV camera (model PIVCAM 10-30, resolution 1,000 × 1,016 pixels), which viewed the light sheet through the side wall of the flume. The camera was equipped with a 105-mm/f2.8 Nikon lens. In some experiments, two 14-mm extension rings were also mounted on the camera to capture the velocity field close to the bed, as required.

After steady flow was established, either 200 or 300 pairs of PIV images were taken at a repetition rate of 10 Hz, which resulted in 20 or 30 s of velocity measurements. corresponding to 20 or 30 s of velocity measurements. This was performed three or four times at an interval of about 15 minutes. The process was then repeated at other measurement locations. PIV image processing was conducted using the INSIGHT 4G software by TSI. The interrogation region dimensions were 128 pixels by 32 pixels with a 50% overlap. The highest spatial resolution achieved in the measured vector field was about 0.8

mm in the x (streamwise) direction and 0.2 mm in the y (vertical) direction, which allowed velocity measurements to be made down to the buffer layer on the acrylic bed. Because of the laser reflection at the free surface, the fluid velocity field measurements were confined mainly to the lower half of the water column. Laser illumination over the measurement area was not always uniform due to the motion of the free surface. Background image subtraction was used to increase the signal-to-noise ratio of the PIV images. In addition, ensemble correlation processing (INSIGHT 4G User's Guide, 2019) was employed to combine all the images in the same experiment run to create a single vector field representing the time-averaged or mean velocity field. The number of spurious vectors in the ensemble correlation vector fields was typically less than 5%. A global range filter was used to remove spurious vectors, followed by vector validation using the local median. Missing vectors were replaced with neighboring mean values, but no smoothing was performed. Due to the PIV camera's small FOV, the different vector columns in the validated vector fields were averaged to produce a single velocity profile at each measurement location to determine the bed shear stress. The averaging process helped to reduce noise in the measured velocity profile.

The uncertainty in the measured velocities were estimated as $\delta x / \delta t$, where δx is the uncertainty in the water particle displacement and δt is the time interval between straddled frames. PIV correlation peak displacement may be assumed to be accurate to within $1/10^{th}$ of a pixel (Kiger, 2015). At the lowest image resolution of 28 μm/pixel and smallest δt of 250 μs, the measured velocities were resolvable to about 1 cm/s, which is much smaller than the velocity measured at the closest distance from the bed.

Only the mean velocities could be obtained by ensemble correlation processing. To obtain the turbulence velocities for calculating the Reynolds stress, traditional (classic) PIV processing was also performed on the PIV images in the flow-through-roughness-transition experiments. The instantaneous vector field (u, v) was determined at each time step, followed by vector validation as described above. The measured vector fields were then examined individually in Tecplot to assess the data quality. Tecplot displayed the choice code in flood contours together with the velocity vectors. A screening process was then performed following the criteria described in the INSIGHT 4G User Guide (2019). Vectors with a choice code from 1 to 4 were considered valid vectors. Velocity fields with most choice codes (over 95% of the vectors) falling between 1 and 4 were accepted. Conversely, velocity fields with less than 95% of choice codes between 1 and 4 were rejected. Typically, out of an initial set of 900 vector fields at each measurement location, only a few hundred were suitable for further analysis. The average of all selected vector fields represents an ensemble or time average $(\bar{u}, \bar{v})$, which was subtracted from the individual velocity fields to give the turbulent velocity fields (u', v'). The turbulence intensities $\left(u'^2, v'^2\right)$ and Reynolds stress $u'v'$, and their ensemble averages $\left(\overline{u'^2}, \overline{v'^2}\right)$ and $\overline{u'v'}$ were then computed. The results were averaged over all the vector columns to produce a single profile for $\left(\overline{u'^2}, \overline{v'^2}\right)$ and $\overline{u'v'}$ for the entire measurement area.

2.3   Determination of Bed Shear Stress

The bed shear stress was determined using four different methods. For uniform flows, the bed shear stress can be computed from the measured water depth and channel slope (depth-slope method) as follows:

$$\tau_b = \rho g R_b S \qquad\qquad (1)$$

where R_b is the bed related hydraulic radius calculated by employing the sidewall correction method of Cheng (2011), and S is the channel slope. The equations for finding R_b can be found in Ting and Kern (2022) and are given as follows.

$$R_b = \frac{f_b}{f} * R_h \tag{1a}$$

$$f_b = f + \frac{2h}{b}(f - f_w) \tag{1b}$$

$$f = \frac{8gR_hS}{v} \tag{1c}$$

$$f_w = 31 * \ln\left(\frac{1.3*R_e}{f}\right)^{-2.7} \tag{1d}$$

where ρ is the fluid density, v is the kinematic viscosity, g is the acceleration of gravity, f_b is the bed related friction factor, f_w is the friction factor for the Plexiglas side wall, $R_e = (V(4R) * v)$ is the Reynolds number, f is the bulk friction factor, $R = (\frac{bh}{b+2h})$ is the bulk hydraulic radius with b representing the channel width and h the effective flow depth. The latter is calculated using the formula $h = h_m \pm [(1-n) * d_{50}]$ where h_m is the measured flow depth and n is the porosity. A plus sign was used when water depth was measured from the top of the rough bed (glass beads and sand), whereas a minus sign was used when the water depth was measured from the top of the Plexiglas to which the roughness elements (gravels) were adhered.

On the acrylic bed, bed shear stress was determined by fitting the Spalding wall function (Spalding, 1961) to the measured velocity points close to the bed:

$$y^+ = u^+ + 0.1108\left[e^{0.4u^+} - 1 - 0.4u^+ - \frac{(0.4u^+)^2}{2!} - \frac{(0.4u^+)^3}{3!} - \frac{(0.4u^+)^4}{4!}\right] \tag{2}$$

where $y^+ = yu^*/v$ and $u^+ = u/u^*$ are the distance from the bed and mean velocity in the streamwise direction in wall units; $u^* = \sqrt{\tau_b/\rho}$ is the friction velocity; and ρ and v are the water density and kinematic viscosity. Note that the overbar in u has been omitted in Eq. (2) for conciseness. Eq. (2) converges to the logarithmic profile when y^+ is large and a linear profile for u when y^+ is small. The spatial resolution of the PIV measurements is not sufficient to resolve the viscous sublayer. Therefore, Eq. (2) is fitted to the measured velocity points in the buffer layer. For the relatively low flow velocities (< 1 m/s) in open-channel flows investigated in this study, the growth of the internal boundary layer was much more rapid than the high-speed flows encountered in close conduits and wind tunnels. Therefore, the bed shear stress can be estimated using the measured velocity points in the buffer layer with Eq. (2).

On the rough bed, the friction velocity was determined from the measured mean velocity profile $u(y)$ in conjunction with the logarithmic law. The latter may be written as follows (see Middleton and Southard, 1984):

$$\ln(y - y_0) = \frac{\kappa}{u^*}u + (\ln k_s - \kappa B) \tag{3}$$

In Eq. (3), y_0 is the elevation of the theoretical bed or displacement height, κ (≈ 0.4) is the von Kármán constant, and B has a value of 8.5 for a hydraulically rough bed. The traditional method for determining u^* is to plot ln $(y - y_0)$ against u and adjust the value of y_0 to produce the best straight-line fit to as many data points as possible in the region where the logarithmic profile is supposed to exist. The latter is commonly taken as $0.2k_s \lesssim y - y_0 \lesssim (0.2 - 0.3)h$ where h is the flow depth (see Sumer and Fuhrman, 2020). The friction velocity u^* is then found from the slope of the best-fit line and the equivalent grain roughness k_s from the y-intercept. By fixing y_0 at the top of the rough bed, Chen and Chiew (2003) found that both τ_b and k_s increase gradually after a smooth-to-rough (STR) transition and take a transitional length of five to six times the flow depth to reach the equilibrium condition. Loureiro et al. (2010) measured the variation of wall shear stress downstream of an RTS transition in a wind tunnel. They obtained the bed shear stress on the smooth bed using various methods, including an optical microsensor and the measured velocity gradient in the viscous sublayer, both of which do not assume the existence of a logarithmic region. Their results show that the wall shear stress on the smooth bed would attain its new equilibrium value almost immediately. Similar results may be expected to occur on the rough bed downstream of an STR transition. Therefore, the results of Chen and Chiew (2003) are somewhat surprising. In Appendix A, we show that their results were a consequence of holding the value of y_0 constant at different streamwise location x.

Previous studies indicate that the theoretical bed may lie anywhere between 0.15 and 0.35 grain diameters below the top of the roughness elements (see Sumer and Fuhrman, 2020). Ting and Kern (2022) showed that for a given set of velocity points, the value of u^* and k_s will increase if y_0 is decreased. In addition, the value of u^* obtained is very sensitive to the value of y_0 chosen. For uniform flows over a rough bed, Kamphuis (1974) found that the k_s/d_{90} ratio increases with the h/d_{90} ratio and reaches an average value of about 2.5 for $h/d_{90} > 20$. Camenen et al. (2006) presented similar results based on the experimental data from a large database, including Kamphuis (1974). Although developed for uniform flows, those results should also apply to gradually varied flow, at least upstream of the roughness transition. Downstream of the transition, an internal boundary layer (IBL) grows outward from the wall with distance from the transition and a logarithmic region may not exist for some distance downstream. The situation is akin to the wall boundary layer in oscillatory flows, where the logarithmic layer exists only sometime after flow reversal and grows as the wave cycle progresses (e.g., Hino et al., 1983; Jensen et al., 1989). In oscillatory flows, it was found that the larger the wave Reynolds number the earlier the logarithmic layer comes into existence. Furthermore, a temporal variation in the value of k_s is considered unrealistic if the flow is fully turbulent and the bed is hydraulically rough. Therefore, a constant value of k_s is typically assumed for the entire flow cycle (e.g., van der A et al., 2011; O'Donoghue et al., 2021)

In this study, we determine the bed shear stress over the rough bed using the method described in Ting and Kern (2022). The value of k_s is first determined from the results in uniform flows based on the h/d_{90} ratio measured in the flow-through-roughness-transition experiment. Figure 2.3 shows a regression curve of k_s/d_{90} versus h/d_{90} obtained using the data by Ting and Kern (2022), and new data from the present study (Table 2.1 and 2.2). The value of y_0 in Eq. (3) is then varied until the y-intercept (with $\kappa = 0.4$ and $B = 8.5$) of the best-fit line yields the same value of k_s obtained with the measured h/d_{90} ratio. Last, the friction velocity u^* is found from the slope of the best-fit line. The above procedure is equivalent to that employed in Ting and Kern (2022) where k_s is held constant and y_0 is varied until the value of κ in the y-intercept of the best-fit line is equal to 0.4.
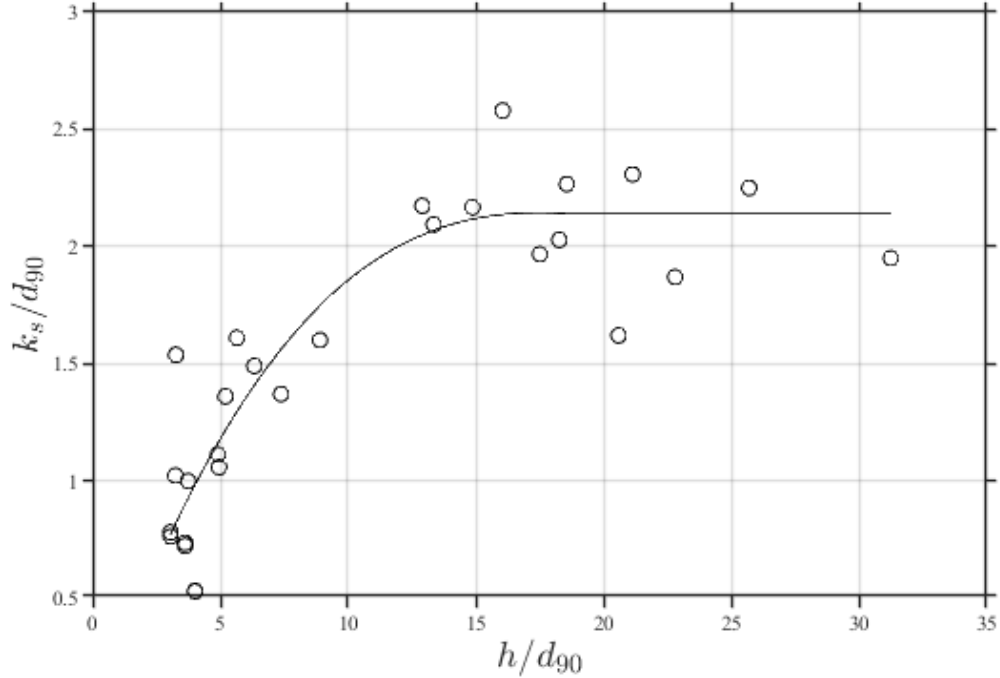
Figure 2.3 Relationship between k_s/d_{90} and h/d_{90} ratios

In steady uniform flows, the total shear stress, which includes the viscous shear stress and Reynolds stress, varies linearly from the bed shear stress to zero at the free surface as follows (Nezu et al., 1993):

$$-\overline{u'v'} + \mu \frac{\partial \bar{u}}{\partial y} = u^{*2}\left(1 - \frac{y}{h}\right) \qquad (4)$$

where h is the flow depth and the overbar denotes time averaging. Since the viscous shear stress is negligible outside the viscous sublayer and buffer layer, the bed shear stress $\tau_b (= \rho u^{*2})$ may be found by linearly extrapolating the measured Reynolds stress distribution in the outer layer to the bed. Rathore et al. (2022) employed this method to determine the evolution of bed shear stress in open-channel flow downstream of an STR transition. Note that Eq. (4) is valid strictly in uniform flows only. In addition, the Reynolds stress is known to overestimate the bed shear stress downstream of an RTS transition due to turbulence generated by the rough bed upstream (see Loureiro et al., 2010). Auel et al. (2014) showed that secondary currents will affect the Reynolds stress distribution in narrow channels with small width-to-depth (b/h) ratios. For these reasons, the bed shear stress obtained using the Reynolds stress method is less reliable compared with the other methods.

2.4   Bed Materials

Sand, glass beads, and gravel (Figure 2.4) were employed as rough materials to construct the rough bed. All three bed material layers were constructed by gluing a single layer of glass bead, sand, or fine gravel to acrylic sheets using epoxy resin. Loose particles were removed with a brush after drying. The acrylic sheets were fastened to the flume floor using the in-floor threaded inserts. The smooth bed was created by fastening acrylic sheets of similar thickness to the flume floor. Black adhesive tape was affixed to the acrylic sheets to make the top surface even with the top of the rough bed and to reduce laser reflection.

8

Figure 2.4 Various channel bed materials used: (a) sand, (b) glass beads, and (c) gravel

2.5 Grain Size Distribution

The sand was well graded while the glass beads and gravel were uniformly graded. The sand had a d_{90} value of 1.5 mm and d_{50} value of 1.1 mm (Figure 2.5). No d_{90} value was determined for the glass beads and gravel due to their uniform grading. The glass bead material passed through the 1.4-mm sieve and was retained on the 1 mm sieve, while the gravel passed through the 4.75-mm sieve and was retained on the 4-mm sieve. Given that the glass beads and gravel were uniformly graded, traditional particle size metrics such as d_{90} and d_{50} were not applicable. The approximate particle diameters were assumed to be 1 mm for the glass beads and 4 mm for the gravel bed.
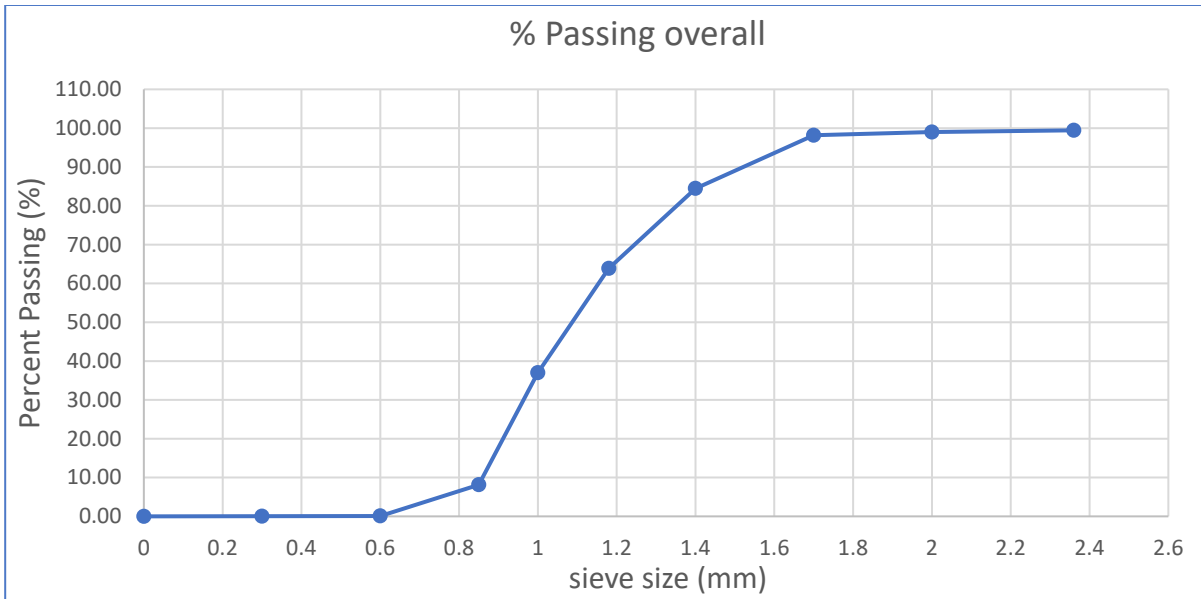
Figure 2.5 Grain size distribution of sand. The results shown is the average of five trials

2.6 Uniform Flow Experiment

A series of flume tests was first performed to determine the equivalent roughness k_s of the glass bead, sand, and fine gravel at different h/d_{90} ratios. The value of k_s was determined from the measured mean velocity profile in conjunction with the logarithmic law, as described in Section 2.3. In a MATLAB script written for this purpose, the bed shear stress τ_b calculated using Eq. (1) served as an input parameter. A straight line was then fitted to the logarithmic law region, and the value of y_0 was adjusted until the bed shear stress from the logarithmic law method matched the value obtained from the depth-slope method. The corresponding k_s value was taken to be the equivalent roughness. The test results are summarized in Tables 2.1 and 2.2.

2.7 Flow-Through-Roughness-Transition Experiment

For the flow-through-roughness-transition experiment, the working channel was divided into an upstream section (Channel 1) and a downstream section (Channel 2). Different bed materials were used in each channel for different tests to achieve the flow conditions for each case shown in Figure 1.1. For Case A, the distance from the head gate to the transition point was equal to approximately 1.25 m, whereas for all the other cases (cases B through E), the distance ranged from around 0.94 m to 0.98 m. The horizontal distances were around 40 times the normal depth. Table 2.3 provides a general description of five cases investigated.

Table 2.1 Summary of test results in uniform flow experiment

Test	S (%)	h (mm)	τ_b (N/m^2)	k_s (mm)	k_s/d_{90}	h/d_{90}	F	Re^*	Bed Material
1	2	31.26	5.12	1.95	1.95	31.26	1.7	150	Glass Bead
2	4	25.71	8.83	2.25	2.25	25.71	2.27	227	Glass Bead
3	6	22.81	11.97	1.87	1.87	22.81	2.72	219	Glass Bead
4	8	21.14	14.98	2.31	2.31	21.14	3.05	303	Glass Bead
5	10	18.27	16.44	2.03	2.03	18.27	3.80	279	Glass Bead
6	12	18.57	19.64	2.27	2.27	18.57	3.70	341	Glass Bead
7	2	30.89	5.03	2.43	1.62	20.59	1.73	185	Sand
8	4	26.27	9.06	2.95	1.97	17.51	2.2	301	Sand
9	6	24.09	12.76	3.87	2.58	16.06	2.51	468	Sand
10	8	22.31	15.95	3.25	2.17	14.87	2.81	440	Sand
11	10	20.03	17.94	3.14	2.09	13.36	3.31	451	Sand
12	12	19.36	21	3.26	2.17	12.91	3.48	506	Sand
13	2	35.59	6.03	6.39	1.6	8.9	1.40	532	Gravel
14	4	29.5	10.37	5.46	1.37	7.38	1.85	596	Gravel
15	8	25.3	18.41	5.97	1.49	6.33	2.33	868	Gravel
16	10	22.6	20.52	6.43	1.61	5.65	2.76	987	Gravel
17	12	20.8	22.67	5.43	1.36	5.20	3.12	876	Gravel

Note: A constant discharge of 4.5 L/s was used in all the tests. An average value of 997.5 kg/m^3 and 9.34×10^{-7} m^2/s (23℃) was used for the density and kinematic viscosity.

Table 2.2 Summary of test results from the uniform flow experiment of Ting and Kern (2022)

Test	S (%)	h (mm)	τ_b (N/m^2)	k_s (mm)	k_s/d_{90}	h/d_{90}	F	Re^*	Bed Material
1	2	36.3	6.23	8.23	1.11	4.91	1.35	507	Gravel
2	2	36.6	6.29	7.83	1.06	4.95	1.34	521	Gravel
3	4	29.7	10.52	3.91	0.53	4.01	1.83	675	Gravel
4	4	29.7	10.56	3.92	0.53	4.01	1.83	675	Gravel
5	5	27.7	12.35	7.39	1.00	3.74	2.04	676	Gravel
6	6	26.8	12.48	5.35	0.72	3.62	2.14	791	Gravel
7	6	26.8	14.50	5.43	0.73	3.62	2.14	791	Gravel
8	8	24	17.35	7.56	1.02	3.24	2.52	811	Gravel
9	8.2	24.1	17.86	11.37	1.54	3.26	2.51	899	Gravel
10	10	22.6	20.61	5.64	0.76	3.05	2.76	945	Gravel
11	10	22.6	20.67	5.77	0.78	3.05	2.76	945	Gravel

Note: Re^* was measured using different temperatures given in Ting and Kern (2022). The gravel bed was well graded with $d_{90} = 7.4$ mm and $d_{50} = 5.6$ mm

Table 2.3 Different cases in flow-through-roughness-transition experiment

Case	Bed Surface (Upstream)	Bed Surface (Downstream)	Water Surface Profile (Upstream)	Water Surface Profile (Downstream)	Flow Condition
A	Rock	Acrylic	M2	S2	Subcritical → Supercritical
B	Glass Bead	Acrylic	N	S2	Supercritical → Supercritical
C	Rock	Sand	M2	N	Subcritical → Subcritical
D	Acrylic	Grass Bead	N	S3	Supercritical → Supercritical
E	Sand	Rock	M1	N	Subcritical → Subcritical

Flow depth was measured at multiple locations along the channel to record the water surface profile. For the gravel bed, the measured flow depth (h_m) was taken from the top of the Plexiglass, while for the glass bead and sand bed, the measured flow depth was taken from the top of the rough bed. Table 2.4 provides a summary of the water surface profile measurements. The flow depth in Table 2.4 represents the effective flow depth assuming a 50% bed porosity.

Table 2.4 Effective water depth at various distance x from roughness transition

Case A		Case B		Case C		Case D		Case E	
x (mm)	h (mm)	x (mm)	h (mm)	x (mm)	h (mm)	x (mm)	h (mm)	x (mm)	h (mm)
-374	31.02	-312	23.36	-305	20.61	-310	27.94	-635	24.68
-64	31.02	-242	23.36	-255	21.11	-260	27.94	-575	24.426
-54	29.75	-212	22.85	-205	21.11	-200	28.19	-415	24.68
-44	28.23	-182	23.36	-165	20.86	-140	27.94	-355	24.68
-34	27.72	-132	23.36	-125	20.61	-80	27.43	-305	24.68
-24	27.21	-102	23.36	-95	20.86	-30	28.70	-285	23.156
-14	25.69	-82	22.09	-75	19.59	-10	28.70	-185	25.95
-4	23.40	-72	22.85	-55	20.10	0	30.73	-115	25.95
0	24.13	-62	22.85	-45	20.35	10	30.98	-75	26.966
6	23.62	-52	22.60	-35	20.35	20	30.47	-35	27.982
16	23.11	-42	22.85	-25	20.23	40	30.98	-5	27.474
26	22.86	-32	23.61	-20	20.10	60	32.50	0	27.21
36	21.84	-22	22.60	-15	20.10	90	32.50	15	27.21
46	21.84	-12	22.60	-10	19.84	120	32.25	45	25.94
56	21.34	-2	23.36	-5	19.59	160	32.50	75	25.432
66	20.45	0	22.86	0	22.14	200	32.25	135	25.94
76	20.32	3	22.61	5	18.33	300	32.25	205	26.448
96	20.07	13	22.35	10	17.06	360	31.49	295	24.67
116	19.81	18	22.23	15	16.81	410	31.23	365	25.94
306	19.81	23	21.84	20	15.79	500	32.00	455	25.94
		28	21.72	25	16.81	580	32.00	585	25.432
		33	21.59	35	15.79				
		38	21.34	45	16.81				
		48	21.08	55	16.55				
		58	20.83	75	16.81				
		68	20.83	105	16.81				
		78	20.57	145	17.06				
		88	20.45	175	17.06				
		98	20.32	205	16.55				
		108	19.56	275	18.33				
		148	19.56	295	17.06				
		178	20.07	335	19.09				
		228	20.07	375	17.82				
		268	19.30	395	16.81				
		298	19.18	435	16.81				
		338	19.30	545	19.60				
		418	19.56	605	19.60				

PIV measurements were conducted in the longitudinal-vertical plane along the centerline of the flume. In cases A and E, PIV measurements were taken at four locations (1 to 4). Locations 2 and 3 were captured immediately before and after the roughness transition while locations 1 and 4 were situated at the upstream and downstream ends of the flow transition, respectively. For cases B through D, PIV measurements were conducted at five locations, following a similar approach to cases A and E. The only difference was an additional location in Channel 2 downstream of the roughness transition.

Table 2.5 presents the experimental parameters used in the flow-through-roughness-transition experiment. Flow depths were measured to a location upstream and downstream where the water surface profile approached uniform conditions, and the measured flow depths at the most upstream and downstream locations were taken as the normal depths h_{01} and h_{02}. The computed Froude numbers, listed in Table 2.5 together with other relevant flow parameters, are used to define the flow regimes in the different cases shown in Figure 1.1.

Table 2.5 Experimental parameters in flow-through-roughness-transition experiment

Case	Q (L/s)	S (%)	U_1 (m/s)	U_2 (m/s)	h_{01} (mm)	h_{02} (mm)	Fr_1	Fr_2	Water Temp. (°C)
A	1.8	0.8	0.354	0.59	31	19.81	0.63	1.35	27
B	1.9	0.9	0.54	0.64	23.36	19.55	1.15	1.46	30
C	1.0	0.9	0.31	0.39	20.86	16.25	0.69	0.95	32
D	3.36	0.9	0.790	0.683	27.94	31.48	1.51	1.21	29
E	1.33	0.6	0.34	0.35	24.67	25.95	0.66	0.71	28

3.   UNIFORM FLOW RESULTS

3.1   Relationship Between k_s/d_{90} and h/d_{90} Ratios

Experiments were performed in a uniform channel at different slopes to investigate the relationship between k_s/d_{90} and h/d_{90}. Kamphuis (1974) found that the k_s/d_{90} ratio increases with the h/d_{90} ratio for h/d_{90} below 20 and approaches a value between 2 and 2.5. Our results, shown in Figure 2.3, which is reproduced in this section as Figure 3.1, agree with Kamphuis's findings. A regression curve was applied to our data showing the relationship between k_s/d_{90} and h/d_{90}, which was subsequently employed to determine the values of k_s in the flow-over-roughness-transition experiment. In the tests performed to obtain this regression curve, no discernible trend was observed in the $\Delta y/d_{90}$ values, where Δy is the distance of the virtual bottom below the top of the rough bed. The range of $\Delta y/d_{90}$ was 0.1 to 0.48 for the gravel, 0.31 to 0.83 for the glass beads, and 0.35 to 1.01 for the sand.
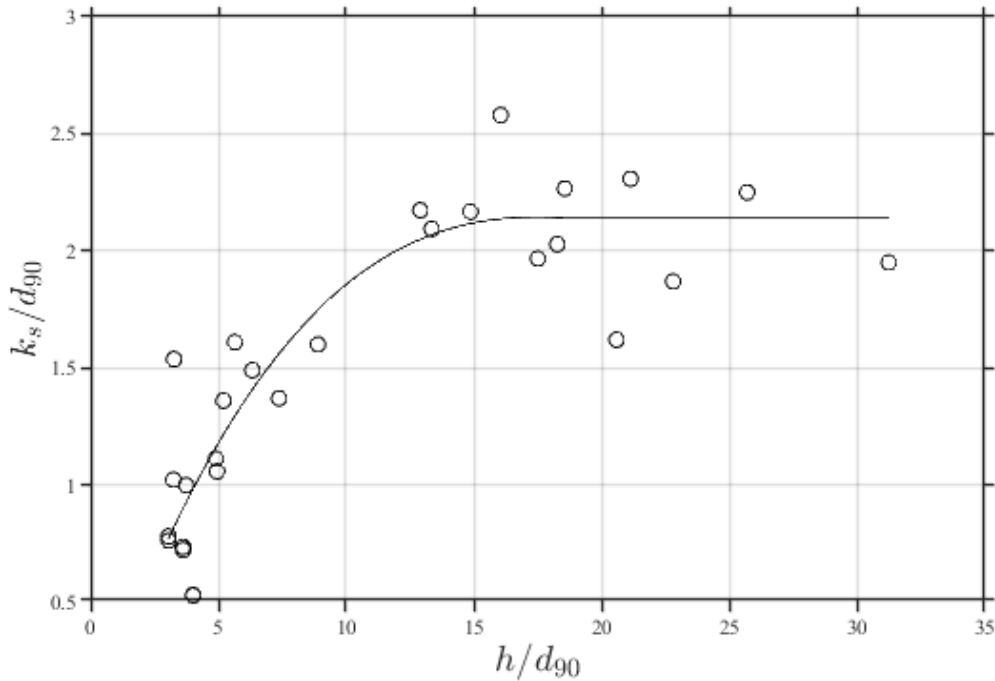
Figure 3.1 Relationship between k_s/d_{90} and h/d_{90} ratios

The following best-fit line was obtained from the measured data:

For (h/d_{90})<15.8

$$(k_s/d_{90}) = 0.0002241(h/d_{90})^3 - 0.01562\left(\frac{h}{d_{90}}\right)^2 + 0.3394\left(\frac{h}{d_{90}}\right) - 0.207 \qquad (5)$$

For $15.8 < (h/d_{90})$<31.26:

(k_s/d_{90}) =2.14

3.2 Effect of Channel Width

Uniform flow experiments were performed with the acrylic bed by varying the Froude number, channel slope, and channel width. These experiments were intended to compare the bed shear stress obtained using the depth-slope method (Eq. 1) and from the measured velocity profile (Eq. 2) in different channel-width-to-flow-depth ratios. Table 3.1 presents the experimental conditions and test results. A false wall was used to reduce the channel width in Test 5.

Table 3.1 Effect of channel width

Test	w (mm)	h (mm)	$\dfrac{w}{h}$	τ_{b1} (N/m^2) (Eq. 1)	τ_{b2} (N/m^2) (Eq. 2)	$\dfrac{\tau_{b1} - \tau_{b2}}{\tau_{b1}} * 100$	Fr
1	152.4	20.62	7.39	9.53	4.96	47.95	3.18
2	152.4	24	6.35	7.14	3.86	45.94	2.53
3	152.4	25.65	5.94	6.01	3.26	45.76	2.29
4	152.4	26.87	5.67	3.89	2.63	32.39	2.14
5	101.6	35.76	2.84	1.64	1.64	0	0.88

Note: w is the channel width. An average value of 997.5 kg/m^3 is used for the water density and 9.34×10^{-7} m^2/s (23℃) for the kinematic viscosity, respectively.

Table 3.1 shows that the τ_b values obtained from the depth-slope method are larger than the values obtained from the wall function method. This could be because that when employing Eq. (1) to compute the bed shear stress in an open channel, the hydraulic radius is calculated assuming an even distribution of bed shear stress on both the channel bed and side walls. As the w/h ratio decreases, the disparity between the τ_b values obtained from the two methods diminishes. These results indicate that the boundary shear stress is not uniformly distributed around the wet perimeter in shallow water depth even when the channel bed and side walls are built of the same materials.

4. FLOW-THROUGH-ROUGHNESS-TRANSITION RESULTS

4.1 Case A

In case A, the water surface profile changes from an M2 to an S2 curve as the flow transitions from a rough bed to a smooth bed. Table 4.1 summarizes the flow conditions at the four PIV measurement locations, and Figure 4.1 shows the measured water surface profile. Channel 1 (upstream) has a gravel bed and Channel 2 (downstream) has an acrylic bed. In Figure 4.1, negative distance indicates the upstream direction from the transition point, and positive distance indicates the downstream direction from the transition point. The roughness transition serves as the reference point.

Table 4.1 Experimental conditions in case A

Location	1	2	3	4
Distance from Transition Point (mm)	-144.7	-17.7	13.9	167
Bed Material	Gravel	Gravel	Acrylic	Acrylic
Water Surface Profile	N	M2	S2	N
Flow Condition	Subcritical	Subcritical	Supercritical	Supercritical
Froude Number	0.63	0.96	1.04	1.35
Flow Depth h (mm)	31	24.7	23.4	19.8
$\dfrac{w}{h}$	4.9	6.2	6.5	7.7

Note: Distance is measured from the roughness transition to the center of FOV of the PIV camera
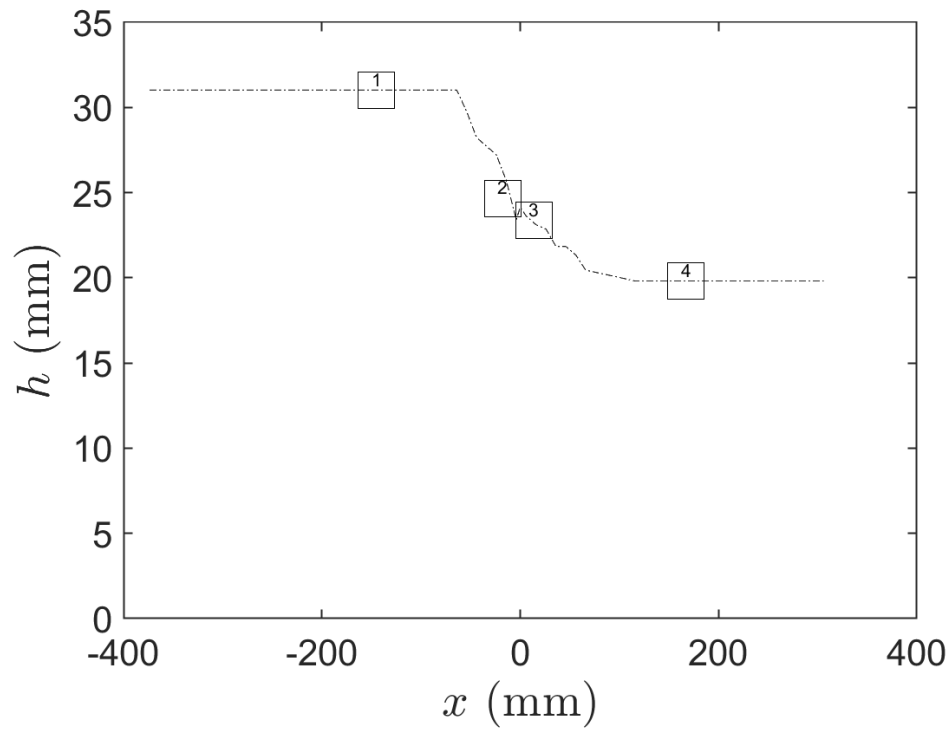
Figure 4.1 Measured water surface profile in case A. The origin $x = 0$ represents the transition point, and h is the effective depth. Negative distance indicates the gravel bed section when going upstream, and positive distance represents the smooth bed section when going downstream. The locations of PIV measurements are marked in the figure
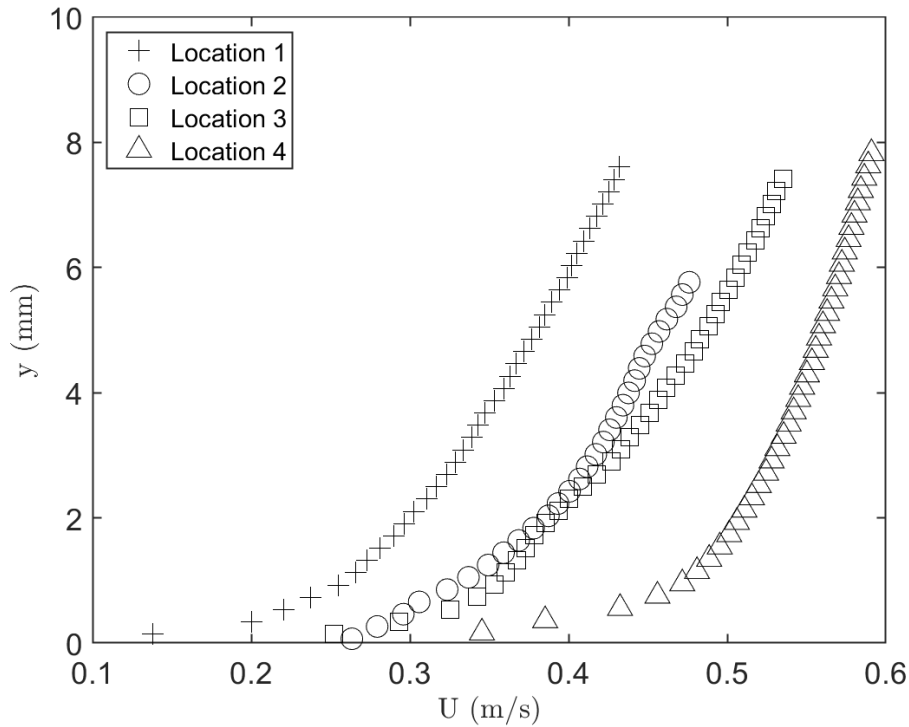
Figure 4.2 Mean velocity profiles at different channel locations

PIV measurements were conducted at four different locations from upstream (location 1) to downstream (location 4) in case A to study the effect of a rough-to-smooth transition on the velocity distribution. Figure 4.2 shows the mean velocity profiles at the different locations. The results are as expected. From location 1 to 2, flow velocity increases throughout the water column due to the decrease in flow depth. Around the transition from location 2 to 3, flow velocity increases adjacent to the bed due to the sudden decrease in bed roughness, but also away from the bed due to the continued decrease in flow depth. This behavior is different from that observed in Chen and Chiew (2003) on an STR transition. Since the flow was subcritical in their experiment, the water surface profile must change from an M1 curve to an N curve at the roughness transition. As the flow velocity decreases adjacent to the bed due to a sudden increase in bed roughness, the flow velocity away from the bed must increase to maintain conservation of mass in a uniform depth (see Figure 3 in their paper). Therefore, the development of velocity profile depends on the water surface profile as well as changes in the bed roughness, and it is more complicated in open-channel flows than in close-conduit and external flows without a free surface. From location 3 to 4, flow velocity over the smooth bed increases throughout the water column due to the decrease in flow depth associated with the S2 profile.
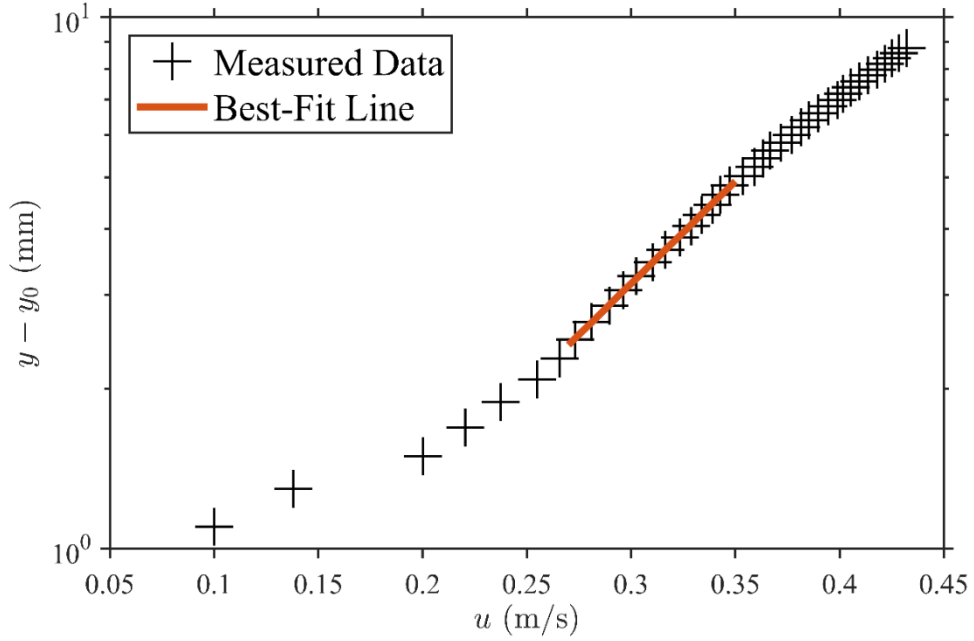
Figure 4.3 Mean velocity profile at location 1 in semi log plot; $u^* = 0.0451$ m/s, $\tau_b = 2.024$ N/m^2, $r^2 = 0.9993$, *rmse* $= 0.005991$, $k_s = 6.6$ mm, *n1=9, n2=21*

Figure 4.3 shows the result of fitting the log law to the mean velocity profile at location 1. The measured flow depth is uniform at this location. Therefore, the bed shear stress computed using the log law can be compared to the value obtained using the depth-slope method (Eq. 1). To determine the friction velocity u^*, the mean velocities are plotted on a semi log plot of $y - y_0$ versus u. A best-fit line is found by fitting Eq. (3) to the largest segment of the measured data that can be represented by a straight line in a region up to about $0.2h$ from the bed. The value of y_0 is varied until the y-intercept $\ln k_s - \kappa B$ (with $\kappa = 0.4$ and $B = 8.5$) yields the same value of k_s obtained from Figure 3.1. The results for $\Delta y / d_{90}$, k_s, and τ_b are 0.29, 6.6 mm and 2.024 N/m^2, respectively, where Δy is the distance of the virtual bottom below the top of the gravel. The bed shear stress determined using the log law method is about 10% lower than the value of 2.21 N/m^2 obtained using Eq. (1).
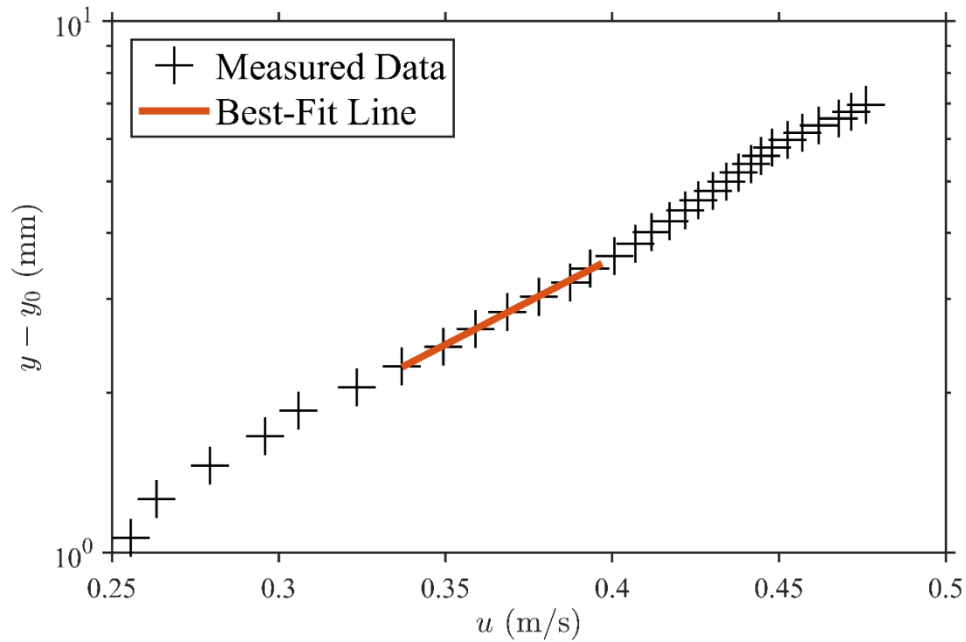
Figure 4.4 Mean velocity profile at location 2 in semi log plot; $u^* = 0.0534$ m/s, $\tau_b = 2.842$ N/m^2, $r^2 = 0.999$, $rmse = 0.005667$, $k_s = 5.37$ mm, $n1=7$, $n2=14$

Location 2 is situated close to the roughness transition. The water surface profile exhibits an M2 curve, and the flow is not uniform. Therefore, the bed shear stress cannot be determined using Eq. (1). Using the log law method (Eq. 3) in conjunction with Eq. (5), the results for $\Delta y/d_{90}$, k_s, and τ_b are 0.285, 5.37 mm and 2.842 N/m^2, respectively. Note that the bed shear stress near the roughness transition is higher than that measured farther upstream due to the decrease in flow depth associated with the M2 profile (Figure 4.1).
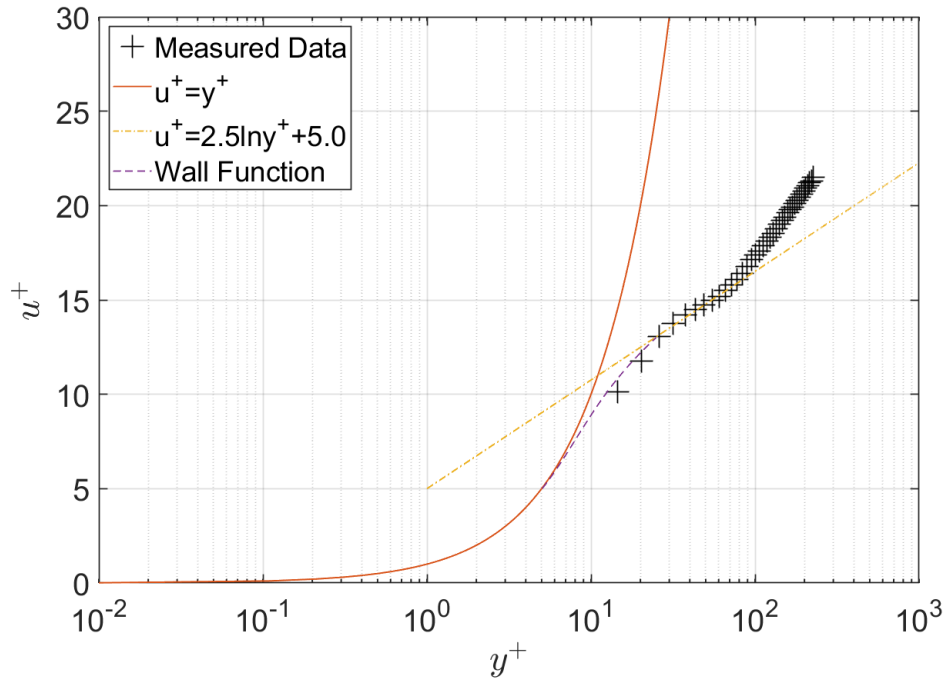
Figure 4.5 Mean velocity profile at location 3 in semi log plot; $u* = 0.0249$ m/s, $\tau_b = 0.6179$ N/m^2

Location 3 is located on the smooth bed close to the roughness transition. The water surface profile exhibits an S2 curve, and the flow is non-uniform. Therefore, Eq. (1) cannot be used to determine the bed shear stress at this location. Furthermore, the log law may not be fully developed close to the transition. Therefore, the bed shear stress was determined from the measured mean velocities in the buffer layer using Eq. (2). The measured data are presented with the Spalding wall function in Figure 4.5. Eq. (2) converges to the linear profile $u^+ = y^+$ when y^+ is small and the logarithmic profile given by:

$$\frac{u}{u^*} = \frac{1}{\kappa} \ln \frac{yu^*}{\nu} + 5.0 \qquad (6)$$

when y^+ is large. The value of u^* is found by minimizing the difference between Eq. (2) and the measured velocities in the buffer layer where $5 \le y^+ \le 30$. This procedure yields a value of 0.62 N/m^2 for τ_b on the smooth bed just downstream of the roughness transition.
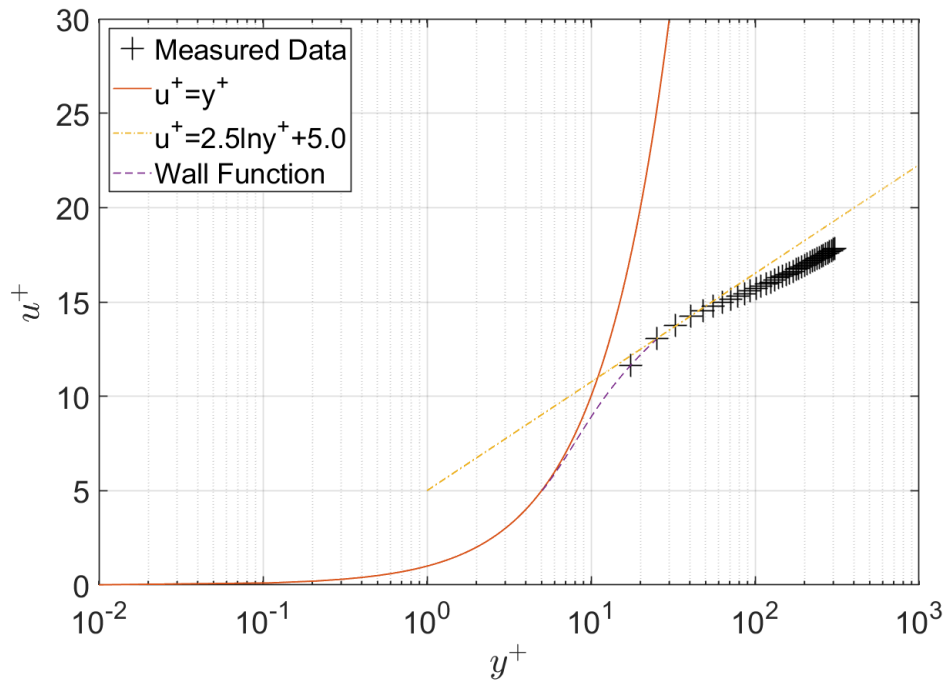
Figure 4.6 Mean velocity profile at location 4 in semi log plot; $u* = 0.0331$ m/s, $\tau_b = 1.092$ N/m^2

Figure 4.6 shows the measured mean velocity profile at location 4 together with the Spalding wall function. The flow depth is uniform, and the bed shear stress can be calculated using Eq. (1). The bed shear stress obtained by fitting the Spalding wall function to the measured velocities in the buffer layer ($\tau_b = 1.092$ N/m^2) is about 20% smaller than the bed shear stress ($\tau_b = 1.23$ N/m^2) obtained using the depth-slope method.
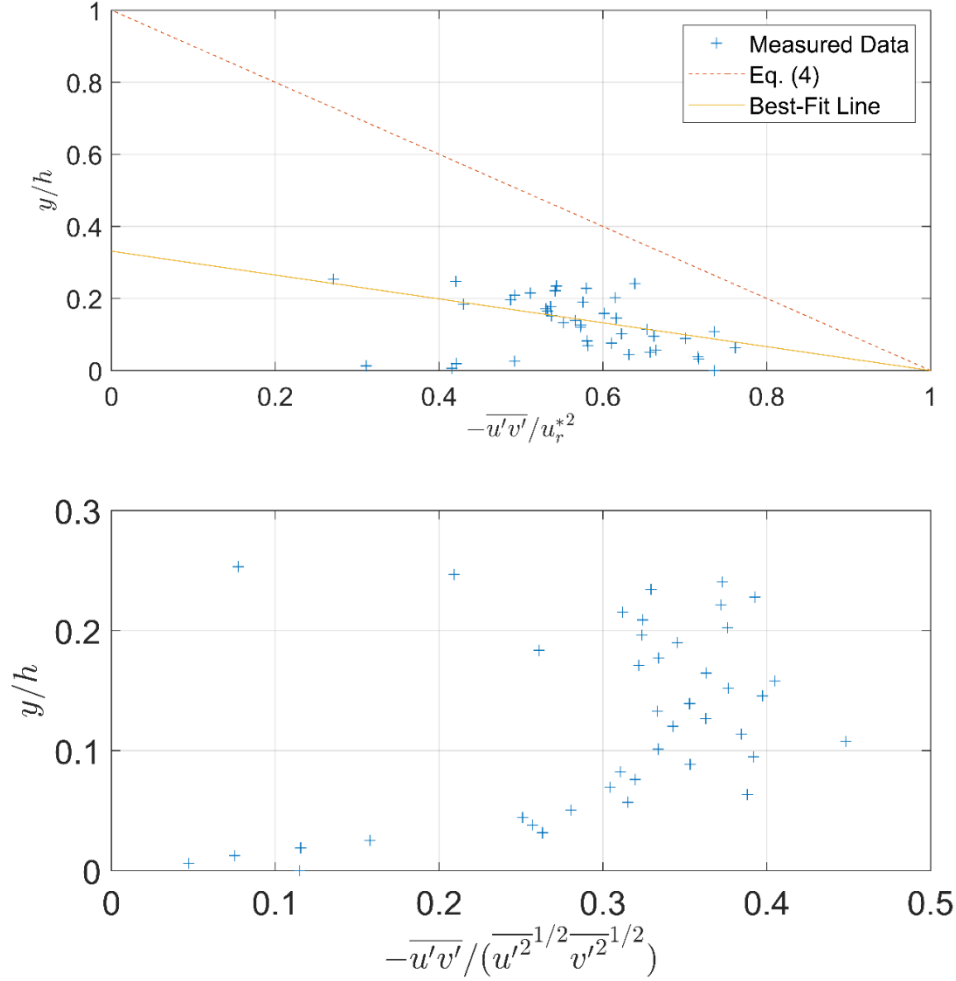
Figure 4.7 Measured Reynolds stress profile at location 1; τ_b = 2.22 N/m² $(u_r^* = 0.0472$ m/s), h = 31.02 mm

Figure 4.7 is a plot of the normalized Reynolds stress $-\overline{u'v'}/u_r^{*2}$ versus dimensionless distance y/h, where h (= 31.02 mm) is the effective flow depth. The origin of the y coordinate is taken at the first data point in the measured velocity profile, which is close to the location of the virtual bottom y_0. This approach is applied throughout to all the Reynolds stress profiles shown in this report.

A value of 2.22 N/m² $(u_r^* = 0.0472$ m/s) for the bed shear stress is found by linearly extrapolating a best-fit line through the measured Reynolds stress data to $y = 0$ (see upper plot). The lower plot shows the distribution of the correlation coefficient $R_{u'v'} = -\overline{u'v'}/\left(\overline{u'^2}^{1/2}\overline{v'^2}^{1/2}\right)$. In steady, uniform flows, the value of $R_{u'v'}$ increases with y/h then remains nearly constant with a value between 0.4 and 0.5 over most of the water column before decreasing again in the free surface region (Nezu et al., 1993). The scattered data in Figure 4.7 show a similar trend with values of $R_{u'v'}$ ranging from 0.3 to 0.4 away from the bed. The lower values of $R_{u'v'}$ observed are likely due to noises in the measured velocities used to compute the ensemble average, which would reduce the Reynolds stress.
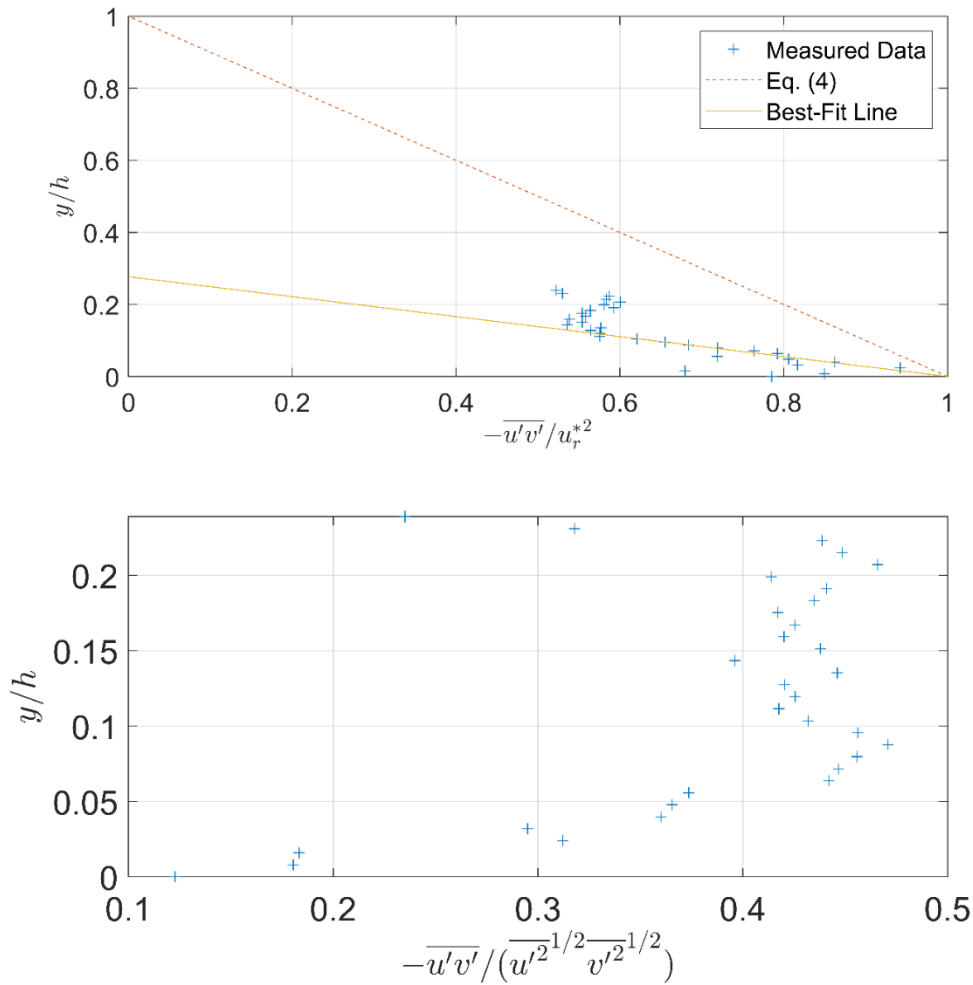
Figure 4.8 Measured Reynolds stress profile at location 2; τ_b = 1.89 N/m^2 ($u_r^* = 0.0435$ m/s), h = 24.67 mm

Figure 4.8 is a plot of $-\overline{u'v'}/u_r^{*2}$ versus y/h at location 2. The bed shear stress of 1.89 N/m^2 ($u_r^* = 0.0435$ m/s) obtained by extrapolating the measured Reynolds stresses to the bed is much lower than the value of 2.84 N/m^2 obtained using the log law method, even though there is good correlation between the turbulence velocities u' and v'; the values of $R_{u'v'}$ away from the bed are between 0.4 and 0.5 (see lower plot). The difference could be the result of a positive pressure gradient in the streamwise direction created by the M2 profile, therefore Eq. (4) is not strictly valid at this location.
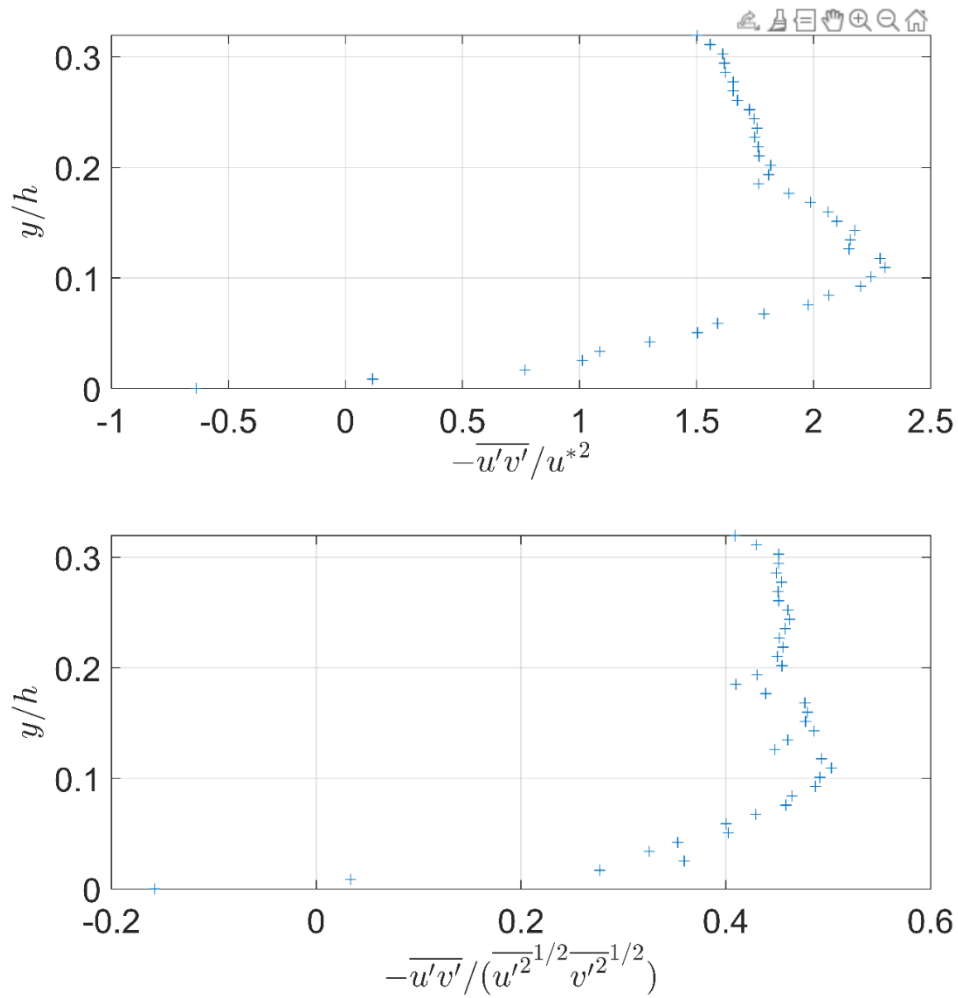
Figure 4.9 Measured Reynolds stress profile at location 3; $u^* = 0.0249$ m/s (from log law), $h = \mathbf{23.37}$ mm

Figure 4.9 presents the distribution of $-\overline{u'v'}/u^*$ at location 3 just after the roughness transition where $h = 23.37$ mm. The measured data cannot be used to determine the friction velocity u_r^* because of memory effect from the flow upstream; therefore, the Reynolds stress distribution was normalized by the friction velocity obtained using the log law method. Note that $-\overline{u'v'}/u^*$ is much larger than unity away from the bed. Therefore, the Reynolds stress method overpredicts the bed shear stress immediately downstream of the RTS transition. This has been observed in external and close conduit flows (e.g., Loureiro et al., 2010) and is due to residual turbulence generated on the rough bed then carried downstream by the flow.
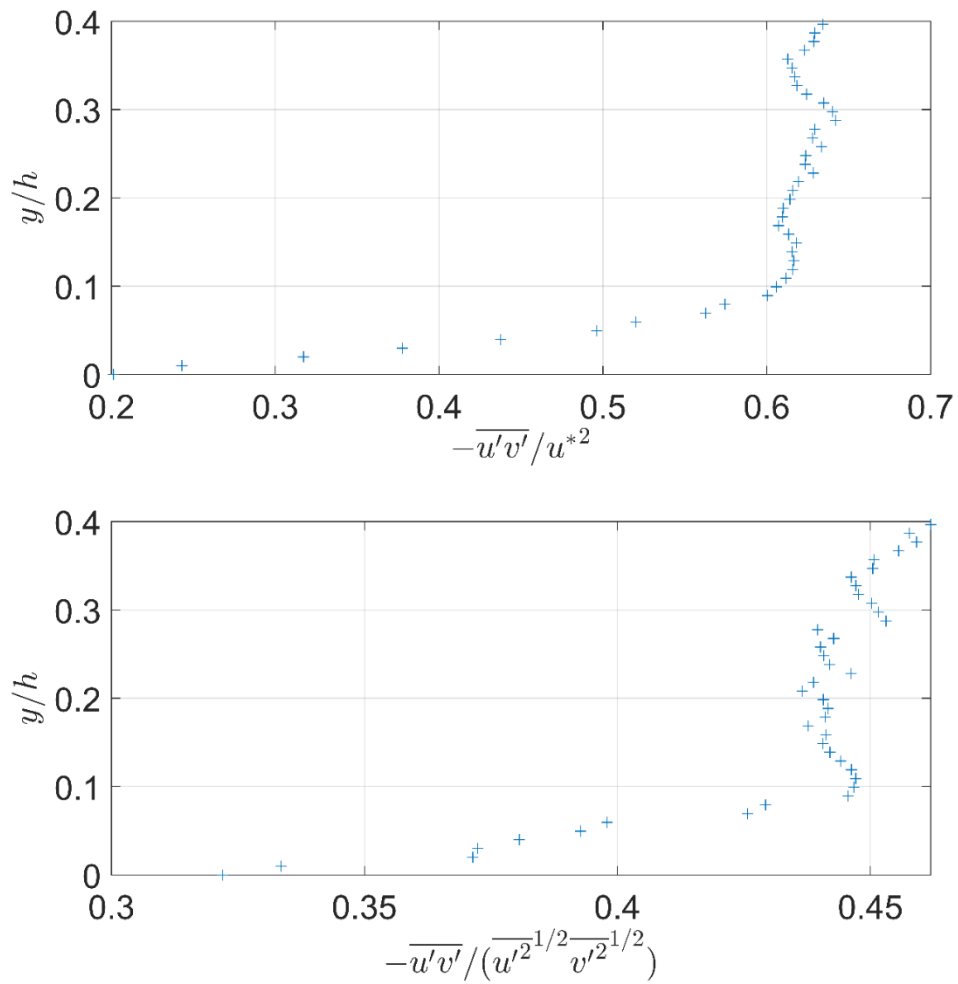
Figure 4.10 Measured Reynolds stress profile at location 4; $u^* = 0.0331$ m/s (from log law), $\boldsymbol{h} = \boldsymbol{19.81}$ mm

Figure 4.10 presents the distribution of $-\overline{u'v'}/u^*$ at location 4 after the roughness transition where $h = 19.81$ mm. These results should be treated with caution because the Reynolds stress was computed with fewer than 300 valid vector fields out of 900 vector fields obtained from the three trials. Consequently, the bed shear stress was not determined using the Reynolds stress method at this location.

Table 4.2 Summary of bed shear stress values (in N/m^2) obtained using various methods in case A

Location	1	2	3	4
Bed Material	Gravel	Gravel	Acrylic	Acrylic
Water Surface Profile	N	M2	S2	N
τ_b (Eq. 1)	2.21	NA	NA	1.23
τ_b (Eq. 2)	NA	NA	0.62	1.09
τ_b (Eq. 3)	2.02	2.84	NA	NA
τ_b (Eq. 4)	2.22	1.89	NA	NA

Table 4.2 summarizes the bed shear stresses at the four measurement locations obtained using the various methods. Eq. (1) is based on the measured flow depth and channel slope and can be used to determine the bed shear stress at locations 1 and 4 where the flow depth approaches uniform conditions. Eq. (2) is only valid on a smooth bed (locations 3 and 4), and the results show that the bed shear stress increases with distance downstream of the roughness transition. Eq. (3) is valid in both uniform and gradually varied flows and can provide a good estimate of the bed shear stress when the logarithmic layer has time to develop, such as at locations 1 and 2 upstream of the roughness transition. The bed shear stress obtained using Eq. (3) at location 1 is about 10% smaller than that obtained from Eq. (1). Eq. (4) is the least reliable method for determining the bed shear stress; it produces a much lower value of τ_b at location 2 and greatly overestimates the bed shear stress downstream of the roughness transition due to memory effect of the flow. For the bed shear stress determined from the measured velocity profiles (Eq. 2 and Eq. 3), the bed shear stress is lower at location 1 than at location 2 due to the M2 profile. Similarly, the bed shear stress is lower at location 3 than at location 4 due to the decreasing flow depth under an S2 profile. In summary, the key observation from the results of case A is that the variation in bed shear stress is related to changes in both bed roughness and flow depth.

4.2 Case B

In case B, the water surface profile changes from an N curve to an S2 curve as the flow transitions from a rough to a smooth bed. Table 4.3 summarizes the flow conditions at the five PIV measurement locations, and Figure 4.11 shows the measured water surface profile. Channel 1 (upstream) has a rough bed made of glass beads, and Channel 2 (downstream) has an acrylic bed.

Table 4.3 Experimental conditions in case B

Location	1	2	3	4	5
Distance from Transition Point (mm)	-110	-20	14	153	434
Bed Material	Glass Bead	Glass Bead	Acrylic	Acrylic	Acrylic
Water Surface Profile	N	N	S2	N	N
Flow Condition	Supercritical	Supercritical	Supercritical	Supercritical	Supercritical
Froude Number	1.15	1.17	1.19	1.45	1.46
Flow Depth h (mm)	23.4	22.6	22.4	19.6	19.6
$\dfrac{w}{h}$	6.5	6.7	6.8	7.8	7.8

Note: Distance is measured from the roughness transition to the center of FOV of the PIV camera
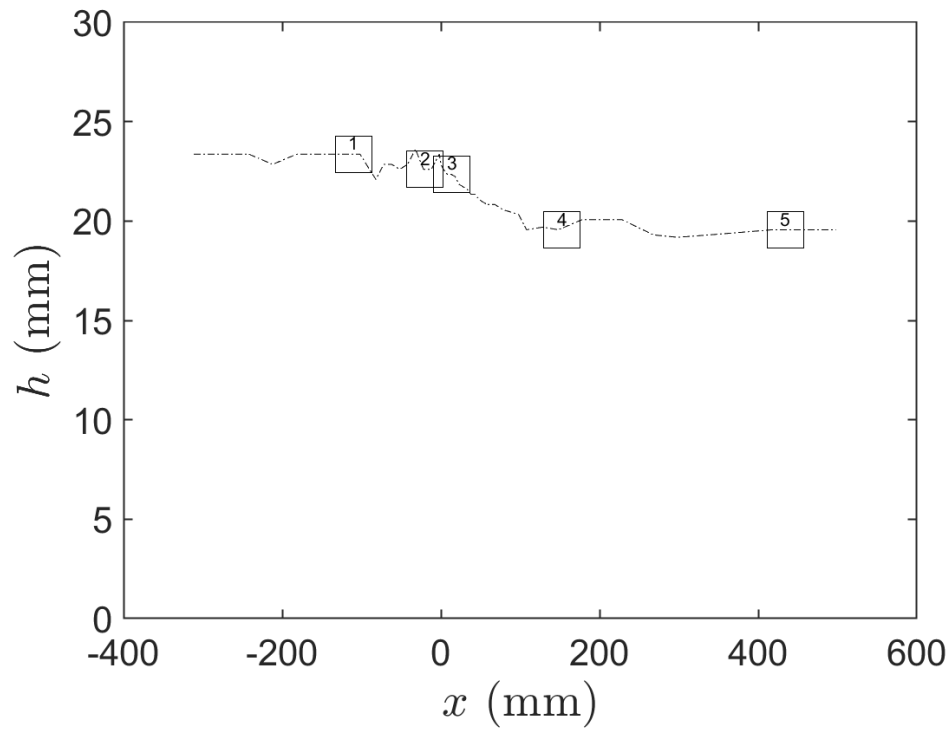
Figure 4.11 Measured water surface profile in case B. The origin $x = 0$ represents the transition point, and h is the effective depth. Negative distance indicates the glass bead section when going upstream, and positive distance represents the smooth bed section when going downstream. The locations of PIV measurements are marked in the figure.
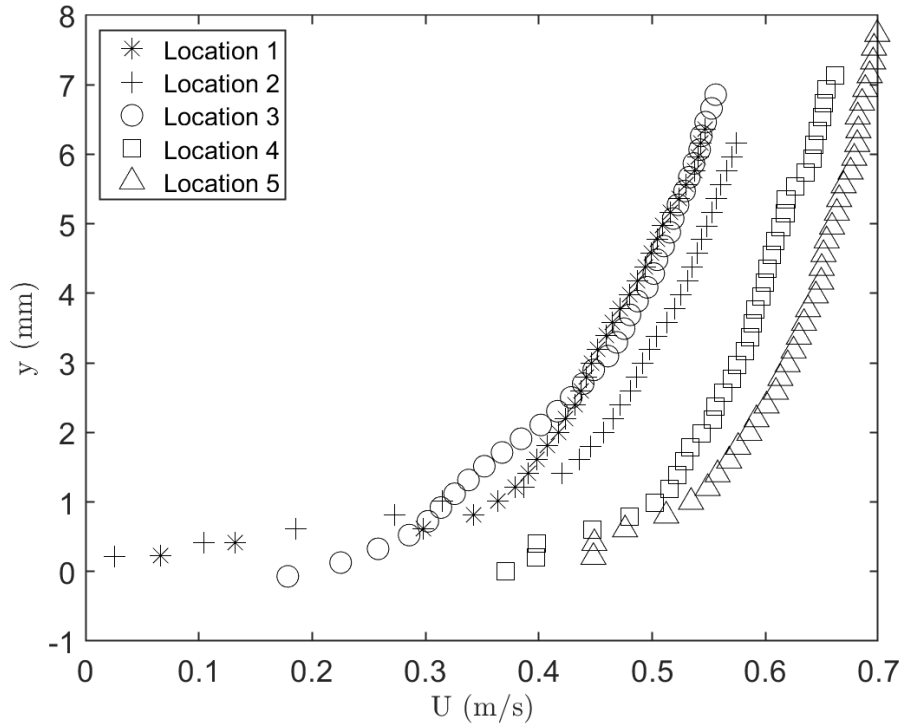
Figure 4.12 Mean velocity profiles at different channel locations

PIV measurements were conducted at five different locations from upstream (location 1) to downstream (location 5) in case B. Figure 4.12 shows the mean velocity profiles at the different locations. The origin of the vertical coordinate ($y = 0$) on the rough bed is taken as the elevation where the measured velocity is close to zero. As the water flows from the rough bed to the smooth bed, the fluid velocity adjacent to the bed increases. The measured velocity profiles near the bed at locations 1 and 2 are similar under the N profile. The velocity is higher at locations 3 and 4 due to the smooth bed and smaller water depth. From location 2 to 3, fluid velocity increases near the bed due to the sudden decrease in bed roughness but decreases away from the bed to maintain conservation of mass. The largest increase in fluid velocity occurs from locations 3 and 4. The increase in fluid velocity is much smaller between locations 4 and 5 as the flow approaches equilibrium condition downstream.
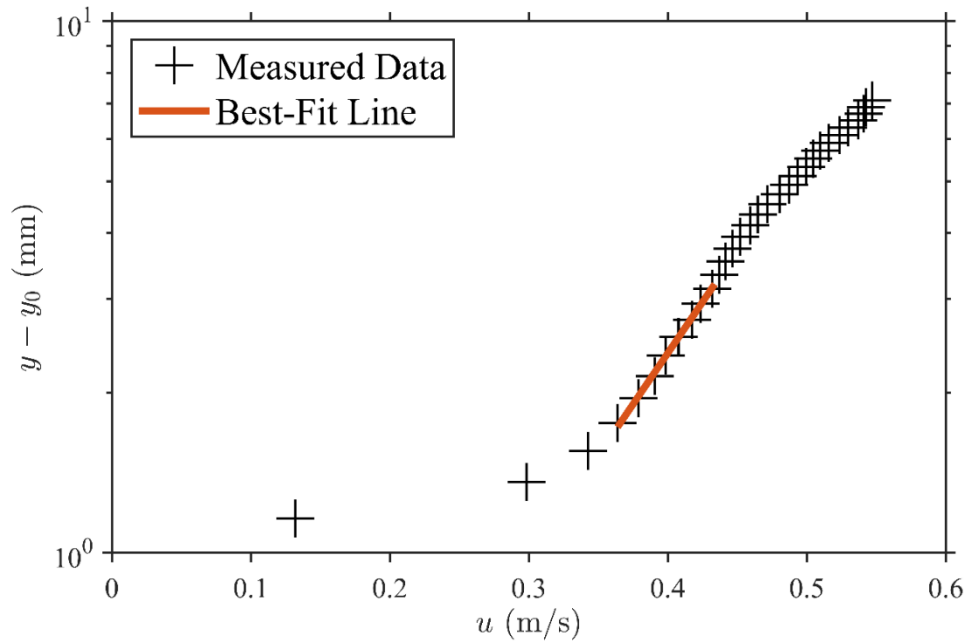
Figure 4.13 Mean velocity profile at location 1 in semi log plot; $u^* = 0.0452$ m/s, $\boldsymbol{\tau_b} = 2.03$ N/m^2, $r^2 = 0.9977$, *rmse* $= 0.01122$, $\boldsymbol{k_s}$=2.06 mm, *n1*=5, *n2*=13

Figure 4.13 shows the result of fitting the log law to the mean velocity profile at location 1. Location 1 is in the upstream region where the water surface profile remains uniform. Consequently, Eq. (1) is valid at this location. The bed shear stress obtained using the log law can be compared to the bed shear stress obtained using the depth-slope method. A similar procedure to that used in case A was employed for the calculation of the bed shear stress. The value of y_0 is varied until the y-intercept $\ln k_s - \kappa B$ (with $\kappa = 0.4$ and $B = 8.5$) yields the same value of k_s obtained from Eq. (5). The results for $\Delta y / d_{90}$, k_s, and τ_b are 0.96, 2.06 mm and 2.03 N/m^2, respectively. The bed shear stress determined using the log law method is about 13% higher than the value of 1.79 N/m^2 obtained using the depth-slope method.
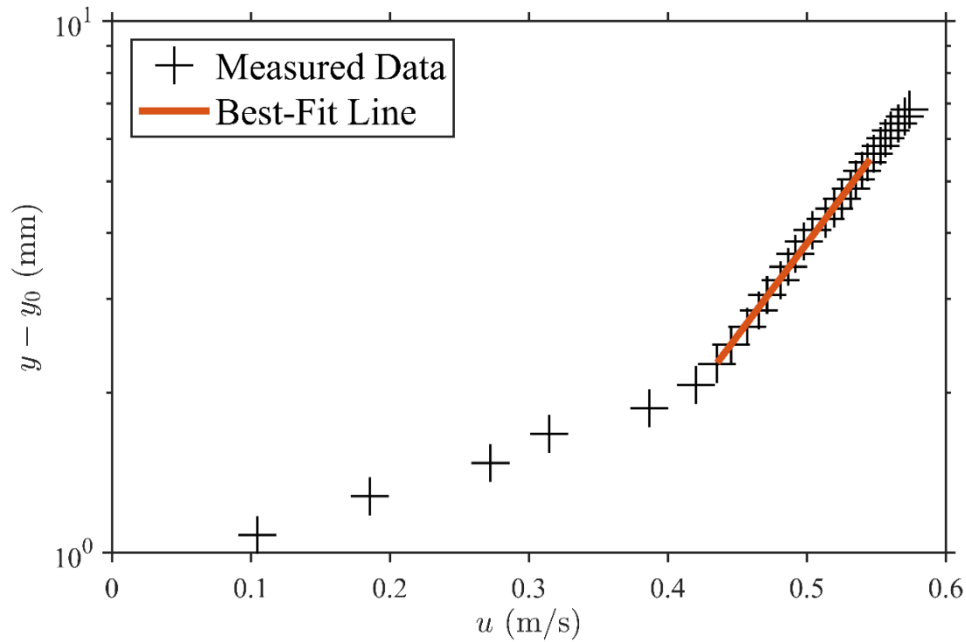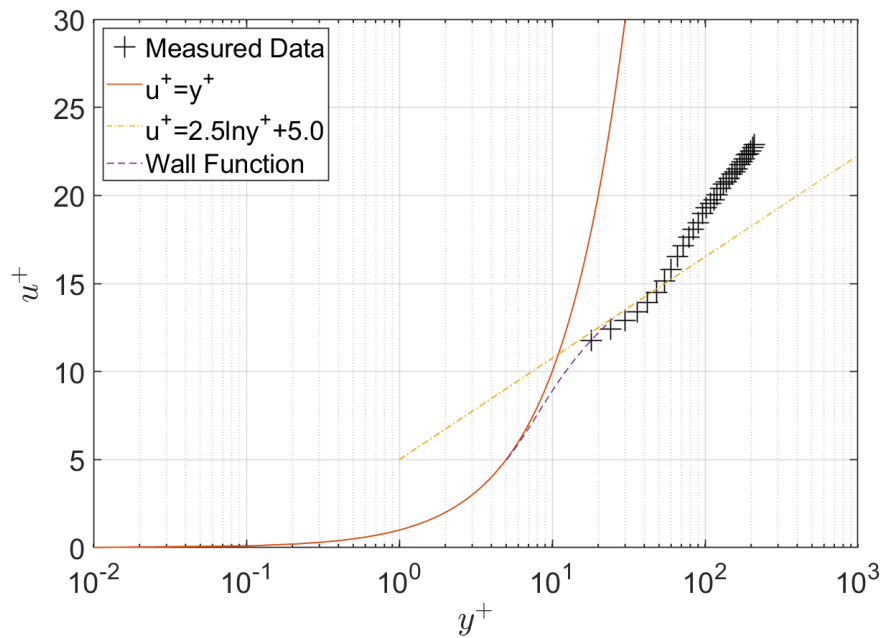
Figure 4.14 Mean velocity profile at location 2 in semi log plot; $u* = 0.0499$ m/s, $\tau_b = 2.48$ N/m^2, $r^2 = 0.9977$, *rmse* $= 0.01379$, $k_s = 2.07$ mm, $n1 = 8$, $n2 = 25$

Location 2 is located right before the transition. The water surface profile exhibits a normal curve. However, the bed shear stress obtained using the log law is different from that calculated using Eq. (1). The results for $\Delta y/d_{90}$, k_s, and τ_b are 0.671, 2.07 mm and 2.48 N/m^2, respectively. The bed shear stress determined using the log law method is about 44% higher than the value of 1.72 N/m^2 obtained using the depth-slope method. A possible explanation for the noticeable difference between these two values is the proximity of location 2 to the roughness transition so that the velocity profile may not be entirely uniform (Figure 4.12).

Figure 4.15 Mean velocity profile at location 3 in semi log plot; $u* = 0.0243$ m/s, $\tau_b = 0.588$ N/m^2

Location 3 is on the smooth bed close to roughness transition. In this region, the water surface profile displays an S2 curve. Figure 4.15 shows that the logarithmic profile is not fully established at this location. Although the lower part of the log law appears to be well established, the upper part of the log law region is still in the process of being formed. The value of u^* is found by minimizing the difference between Eq. (2) and the measured velocities in the buffer layer where $5 \leq y^+ \leq 30$. This procedure yields a value of 0.588 N/m^2 for τ_b on the smooth bed just downstream of the roughness transition.
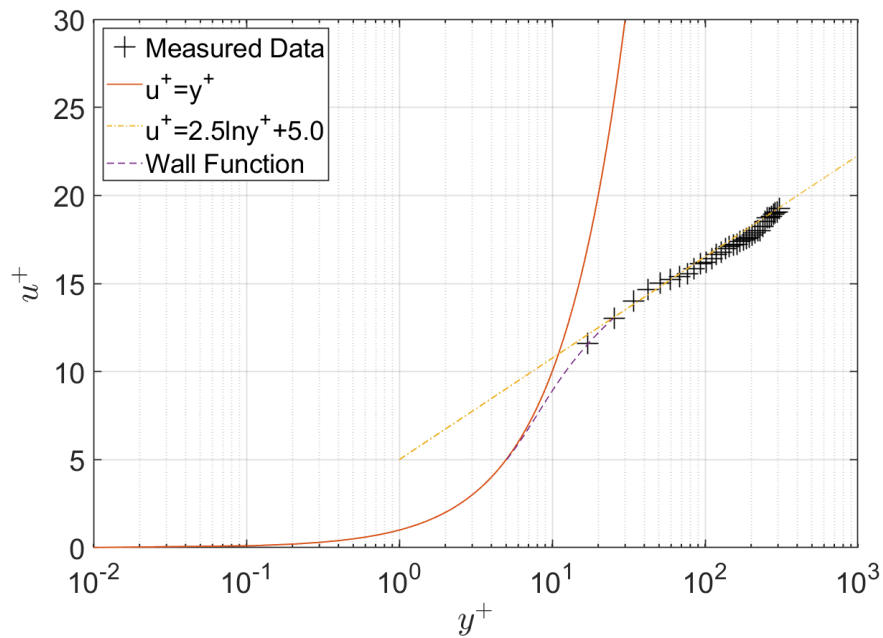
Figure 4.16 Mean velocity profile at location 4 in semi log plot; $u* = 0.0343$ m/s, $\tau_b = 1.17$ N/m^2

At location 4, the water surface profile returns to normal depth. Figure 4.16 shows that the log law is approaching full establishment. The bed shear stress determined using the log law method ($\tau_b = 1.17$ N/ m^2) is 17% lower than the bed shear stress ($\tau_b = 1.37$ N/m^2) obtained using the depth-slope method.
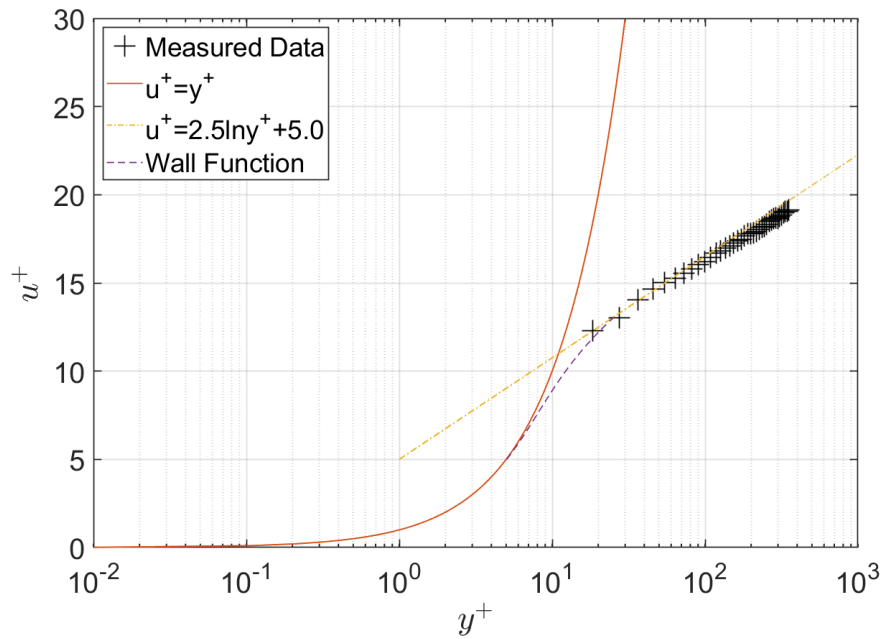
Figure 4.17 Mean velocity profile at location 5 in semi log plot; $u* = 0.0365$ m/s, $\tau_b = 1.33$ N/m^2

At location 5, the measured flow depth is uniform. Figure 4.17 shows that the logarithmic region is well established. The log law region is wider compared with locations 3 and 4. The bed shear stress determined using the log law method (τ_b = 1.33 N/m²) is only 3% lower than the bed shear stress obtained using the depth-slope method (τ_b = 1.37 N/m²).
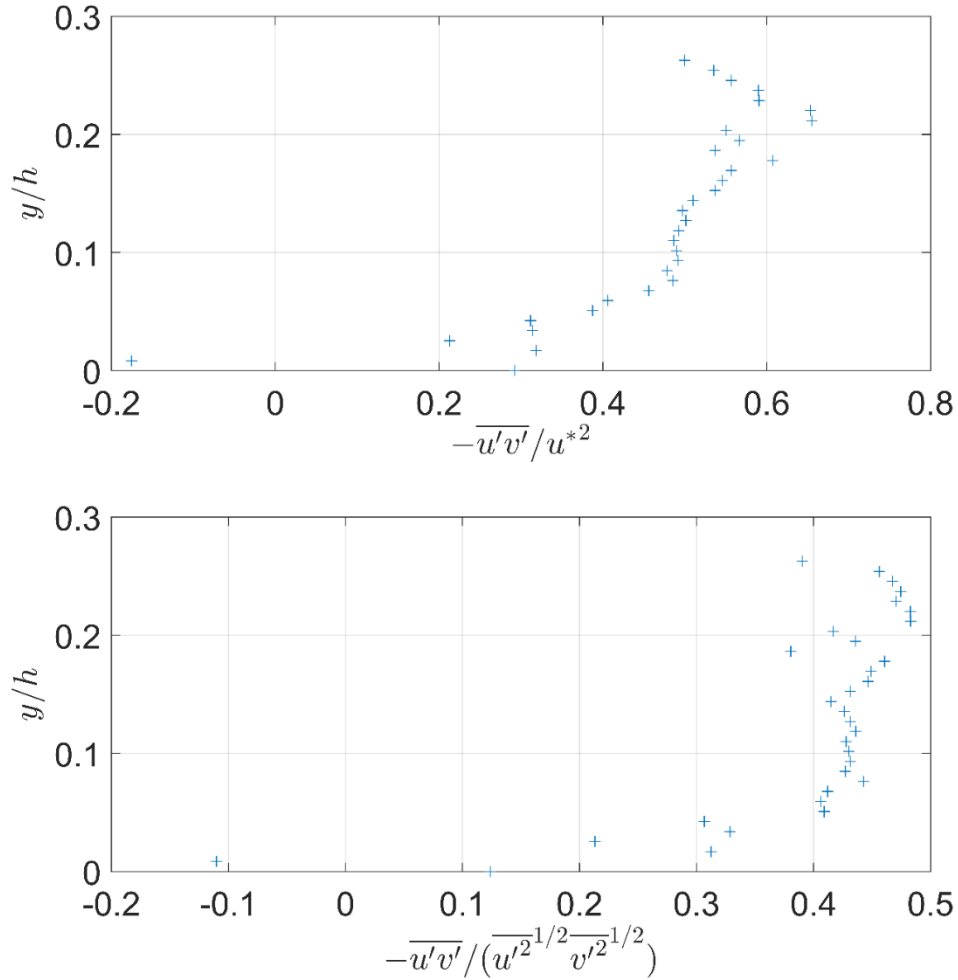
Figure 4.18 Measured Reynolds stress profile at location 1; u^* = 0.0452 m/s (from log law), **h** = 23.36 mm

Figure 4.18 is a plot of the normalized Reynolds stress $-\overline{u'v'}/u^*$ versus dimensionless distance y/h, where h (= 23.36 mm) denotes the effective flow depth based on a 50% porosity. The measured data depicted in this figure should be treated with caution because the Reynolds stress was computed based on fewer than 300 valid vector fields out of 900 obtained from the three trials. Therefore, the bed shear stress was not determined using the Reynolds stress method and the measured data were normalized using the friction velocity obtained using the log law.
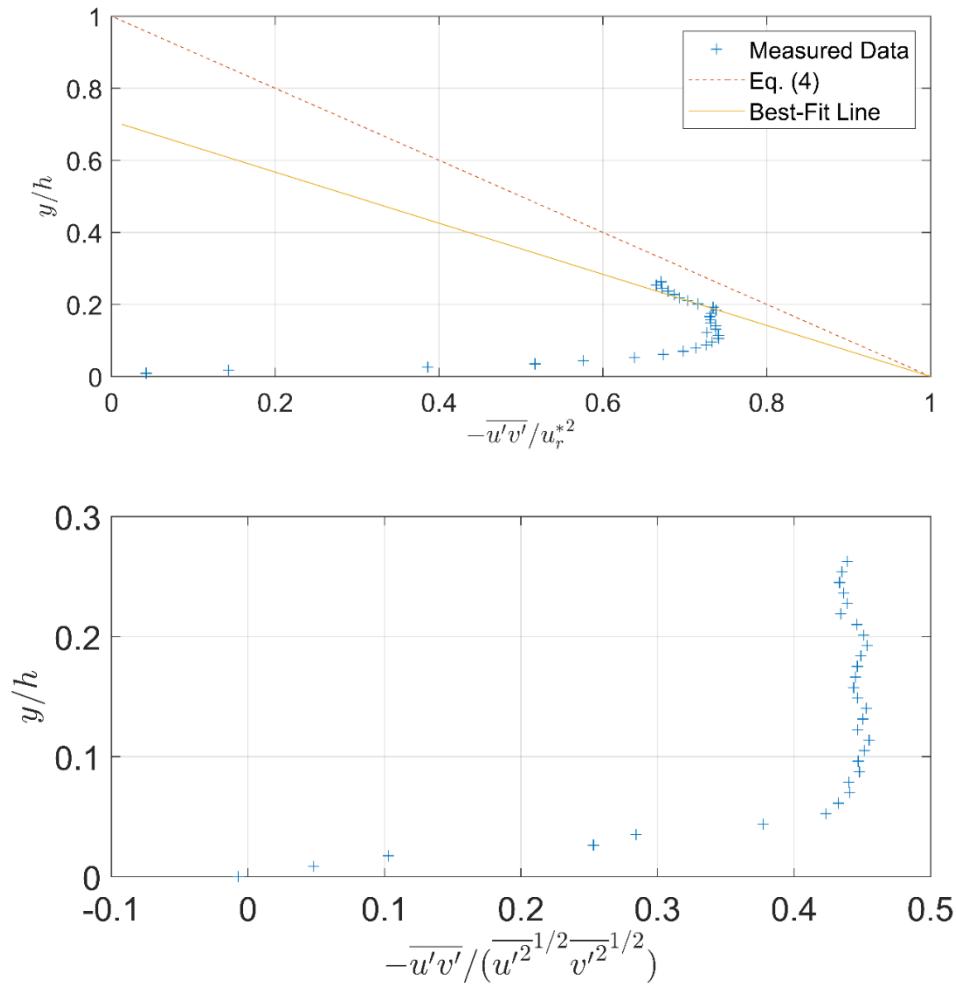
Figure 4.19 Measured Reynolds stress profile at location 2; τ_b = 1.56 N/ m^2 (u_r^* = **0.0396** m/s), h = 22.6 mm

Figure 4.19 is a plot of $-\overline{u'v'}/u_r^{*2}$ versus y/h at location 2, with $h = 22.6$ mm denoting the effective flow depth based on a 50% porosity. The measured Reynolds stresses are much lower than the values obtained using the log law method, even though there is good correlation between the turbulence velocities u' and v'; the values of $R_{u'v'}$ away from the bed are between 0.4 and 0.5 (lower plot). The bed shear stress obtained by extrapolating the measured Reynolds stress to the bed is 1.56 N/m^2(u_r^* = 0.0396 m/s).
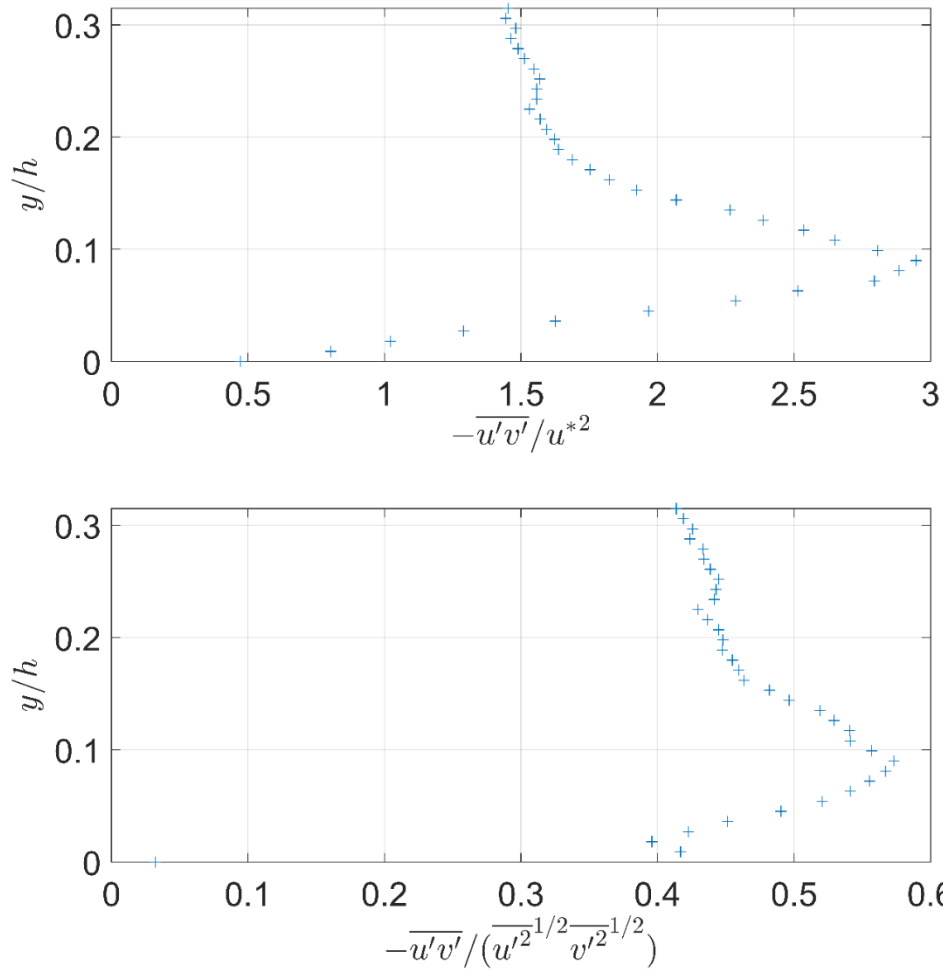
Figure 4.20 Measured Reynolds stress profile at location 3; $u^* = 0.0243$ m/s (from log law), $h = 22.4$ mm

Figure 4.20 presents the distribution of $-\overline{u'v'}/u^*$ at location 3 just after the roughness transition where $h = 22.4$ mm. The measured Reynolds stress significantly overpredicts the bed shear stress immediately downstream of an RTS transition. This has been observed in external and close conduit flows and is due to residual turbulence generated upstream and advected downstream by the flow (e.g., Loureiro et al., 2010). Therefore, the bed shear stress was not determined by Reynolds stress extrapolation, and the measured data were normalized using the friction velocity obtained from the log law.
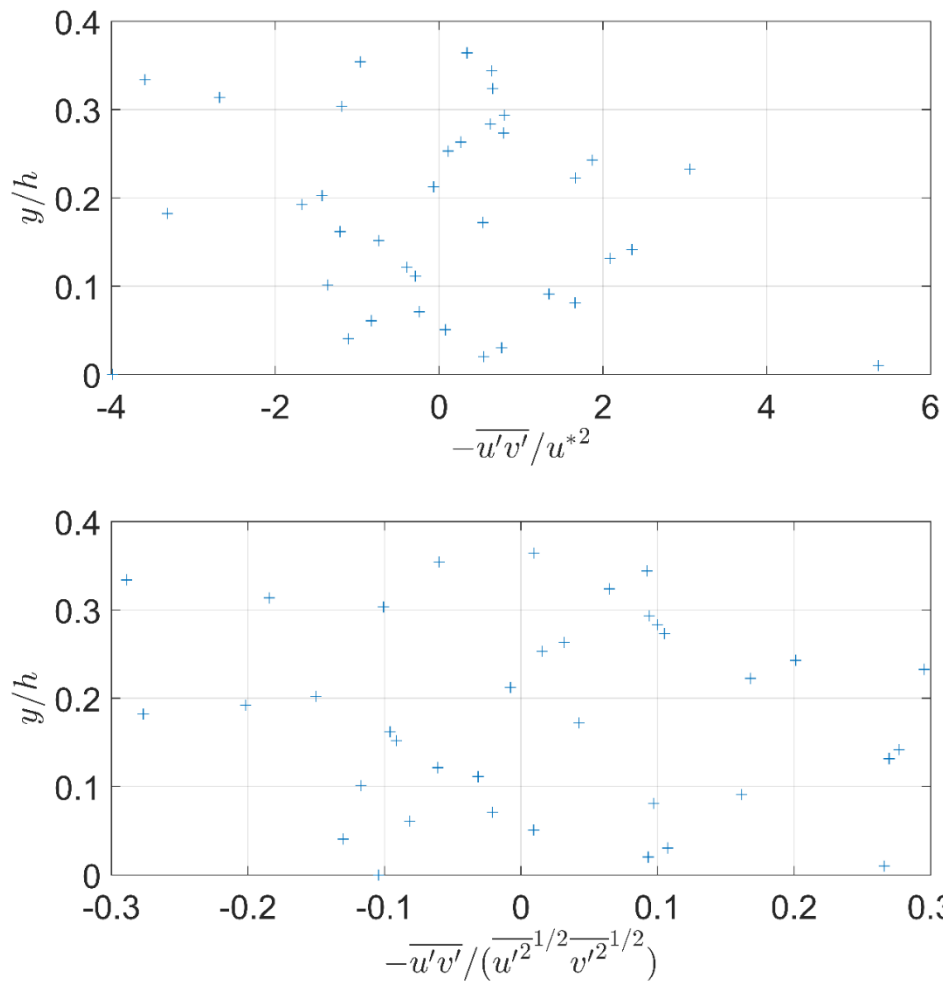
Figure 4.21 Measured Reynolds stress profile at location 4; $u^* = 0.0343$ m/s (from log law), $h = 19.56$ mm

Figure 4.21 presents the distribution of $-\overline{u'v'}/u^*$ at location 4 on the smooth bed where $h = 19.56$ mm. The measured Reynolds stress is $-\overline{u'v'}/u^*$ and exhibits a considerable amount of scatter. Therefore, it is difficult to determine the bed shear stress from the measured data by Reynolds stress extrapolation. Similarly, the correlation between u' and v' exhibits a significant amount of scatter (lower plot) and is considerably smaller than the values of 0.4 to 0.5 observed in turbulent open channel flows.
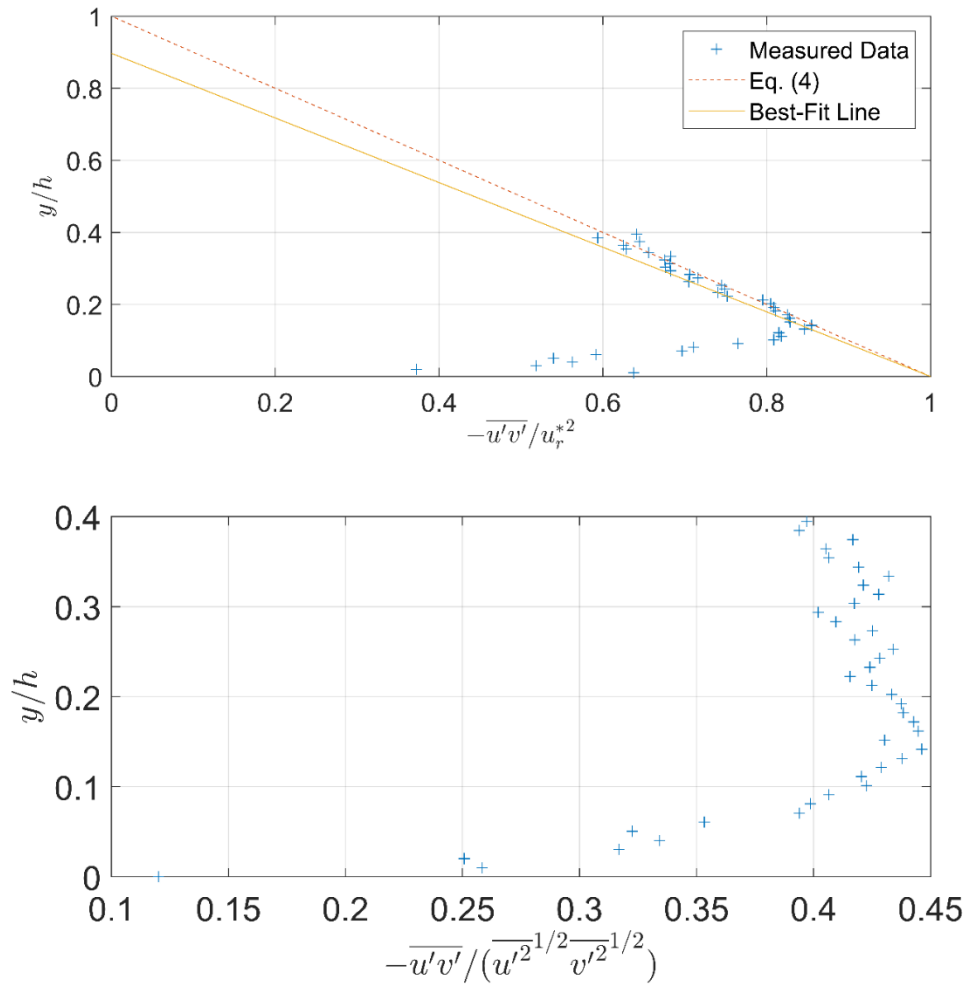
Figure 4.22 Measured Reynolds stress profile at location 5; $u_r^* = 0.0320$ m/s, $h = 19.56$ mm

Figure 4.22 is a plot of $-\overline{u'v'}/u_r^{*2}$ versus y/h at location 5 where $h = 19.56$ mm. The bed shear stress obtained by extrapolating the measured Reynolds stress to the bottom is 1.01 N/m², which is much lower than the value of 1.33 N/m² obtained using the log law method.

Table 4.4 Summary of bed shear stress values (in N/m^2) obtained using various methods in case B

Location	1	2	3	4	5
Bed Material	Glass Bead	Glass Bead	Acrylic	Acrylic	Acrylic
Water Surface Profile	N	N	S2	N	N
τ_b (Eq. 1)	1.79	1.72	NA	1.37	1.37
τ_b (Eq. 2)	NA	NA	0.588	1.17	1.33
τ_b (Eq. 3)	2.03	2.48	NA	NA	NA
τ_b (Eq. 4)	NA	1.56	NA	NA	1.01

Table 4.4 summarizes bed shear stresses at the five measurement locations obtained using the different methods. Like case A, a similar trend can be seen in this case in the variation of the bed shear stress. The latter is affected by the local bed roughness and change in water depth along the channel. The water surface profile in Channel 1 is an N-curve and both locations in Channel 1 should have similar bed shear stress, but as location 2 is situated just upstream of an RTS transition, the flow velocity near the bed may be accelerating and thus creates a higher bed shear stress. In Channel 2, the buffer layer is established at location 3 but the logarithmic region has not yet developed. Location 3 has a lower flow velocity and higher water depth than locations 4 and 5, which may explain why the measured bed shear stress is smaller, as the flow depth is still decreasing. There is not as large a difference in the measured bed shear stress at locations 4 and 5 because the flow depth is uniform and the velocity profile is approaching equilibrium condition.

4.3　Case C

In case C, the water surface profile changes from an M2 to an N curve as the flow passes from a gravel bed to a sand bed. Table 4.5 summarizes the flow conditions at the five PIV measurement locations, and Figure 4.23 shows the measured water surface profile. Channel 1 (upstream) has a gravel bed, and Channel 2 (downstream) has a sand bed.

Table 4.5 Experimental conditions in case C

Location	1	2	3	4	5
Distance from Transition Point (mm)	-105	-15	20	200	425
Bed Material	Gravel	Gravel	Sand	Sand	Sand
Water Surface Profile	N	M2	N	N	N
Flow Condition	Subcritical	Subcritical	Subcritical	Subcritical	Subcritical
Froude Number	0.69	0.74	0.95	0.95	0.95
Flow Depth h (mm)	20.9	19.8	16.8	16.3	16.3
$\dfrac{w}{h}$	7.3	7.7	9.1	9.4	9.4

Note: Distance is measured from the roughness transition to the center of the FOV of the PIV camera
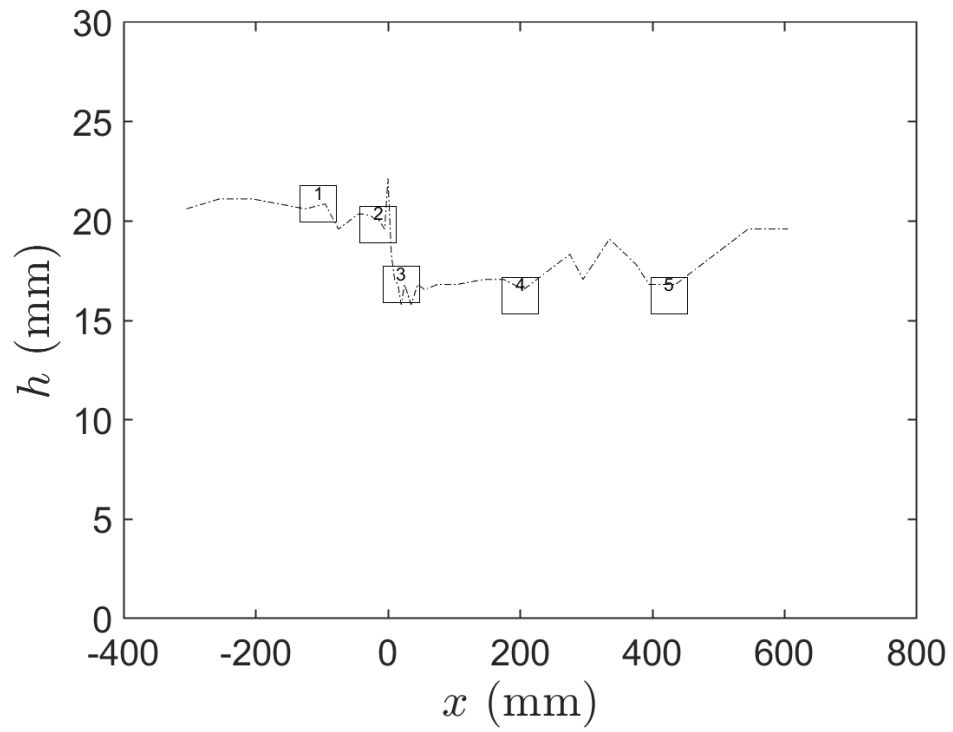
Figure 4.23 Measured water surface profile in case C. The origin $x = 0$ represents the transition point, and $\boldsymbol{h}$ is the effective depth. Negative distance indicates the gravel bed section when going upstream, and positive distance represents the sand bed section when going downstream. The locations of PIV measurements are marked in the figure.
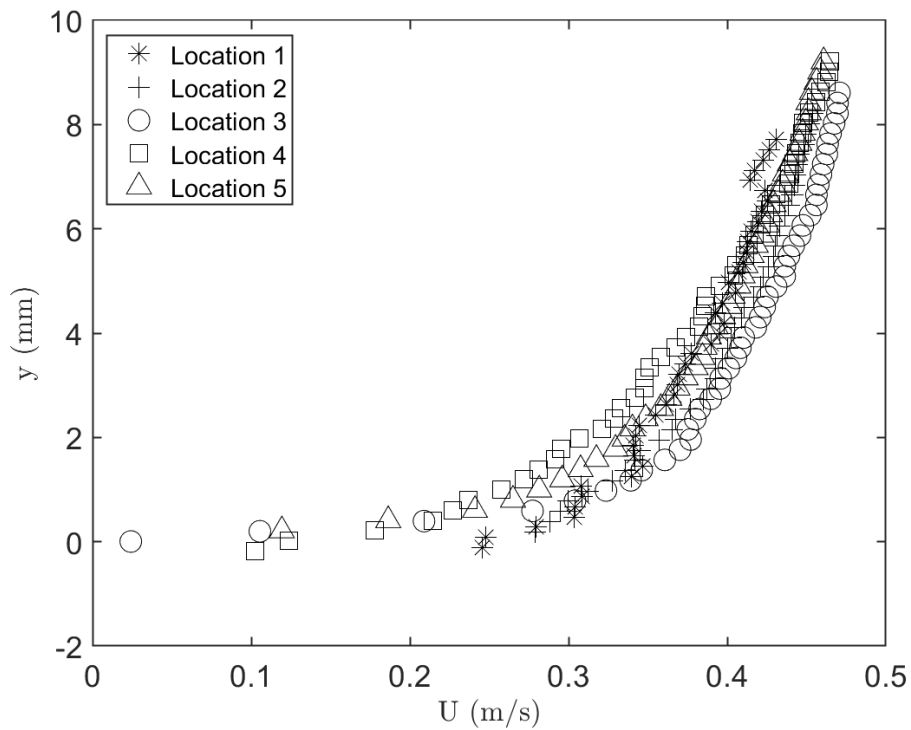
Figure 4.24 Mean velocity profiles at different channel locations

Figure 4.24 presents the mean velocity profiles from upstream (location 1) to downstream (location 5). Note that the measurements cover only the lower half of the water column due to the PIV camera's small FOV. The flow velocity should increase in Channel 1 with downstream distance under the M2 curve, whereas it should remain relatively constant in Channel 2 due to the uniform depth. Figure 4.24 shows that the velocity at location 1 is lower than that at location 2, which is as expected. The increase in flow velocity adjacent to the bed from location 2 to location 3 is consistent with the decrease in bed roughness after the transition. From location 3 to location 4, measured velocities increase adjacent to the bed but decrease away from the bed to maintain conservation of mass in the uniform depth. The measured velocity profiles at locations 4 and 5 are similar, which indicates that equilibrium condition was achieved at these locations.
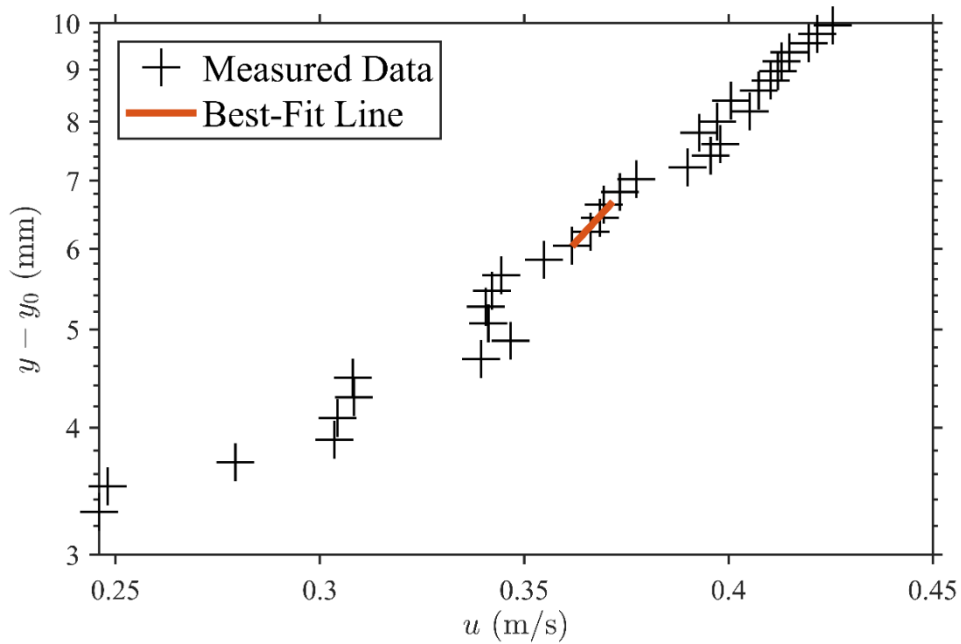
Figure 4.25 Mean velocity profile at location 1 in semi log plot; $u^* = 0.0396$ m/s, $\tau_b = 1.56$ N/m^2, $r^2 = 0.967$, $rmse = 0.011$, $k_s = 4.7$ mm, $n1=15$, $n2=20$

Location 1 represents the upstream area where the water surface profile remains uniform. The results for $\Delta y / d_{90}$, k_s, and τ_b are 0.85, 4.7 mm, and 1.56 N/m^2, respectively. The bed shear stress calculated using the log law is 10% lower compared with the bed shear stress ($\tau_b = 1.72$ N/m²) obtained from the depth-slope method The measured data are somewhat scattered, and the best-fit line does not achieve an r^2 value higher than 99%. This can be attributed to a large gravel protruding above the bed in the measurement area.
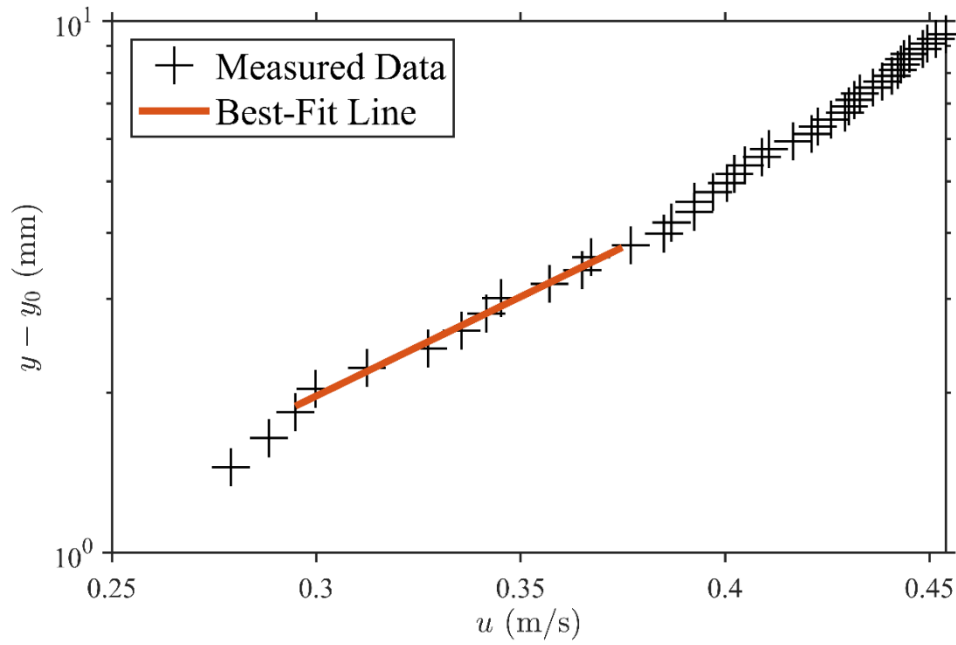
Figure 4.26 Mean velocity profile at location 2 in semi log plot; $u* = 0.0465$ m/s, $\tau_b = 2.15$ N/m^2,
$r^2 = 0.991$, *rmse* = 0.0241, k_s =4.5 mm, *n1*=3, *n2*=13

Location 2 is the location right before the roughness transition. The water surface profile exhibits an M2 curve. The depth-slope method is not applicable in this region. The results for $\Delta y/d_{90}$, k_s, and τ_b from the log law method are 0.58, 4.5 mm, and 2.15 N/m^2, respectively.
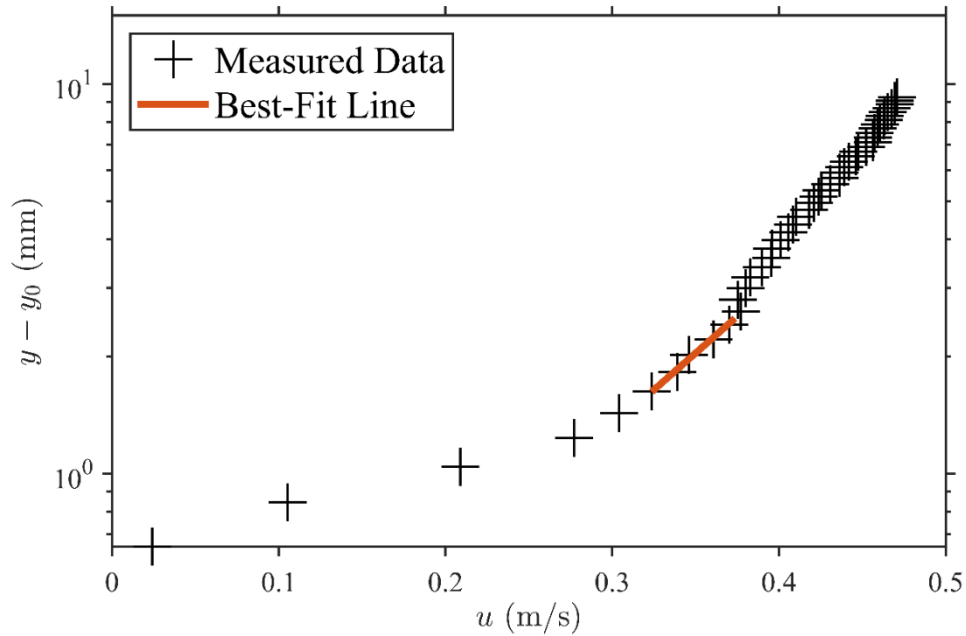
Figure 4.27 Mean velocity profile at location 3 in semi log plot; $u* = 0.0461$ m/s, $\tau_b = 2.11$ N/m^2, $r^2 = 0.992$, *rmse* = 0.0172, k_s =2.9 mm, *n1*=6, *n2*=11

Location 3 is just downstream of the transition. The water surface profile exhibits an N-curve; however, the bed shear stress calculated using the log law at location 3 is different from that calculated by the depth-slope method. The results for $\Delta y/d_{90}$, k_s, and τ_b are 0.65, 2.9 mm, and 2.11 N/m^2, respectively. The bed shear stress determined using the log law method is about 35% higher than the value of 1.36 N/m^2 obtained using Eq. (1), which suggests that, unlike the water surface profile, the velocity profile has not achieved the equilibrium equation.

Figure 4.28 Mean velocity profile at location 4 in semi log plot; $u* = 0.0396$ m/s, $\tau_b = 1.56$ N/m^2, $r^2 = 0.993$, $rmse = 0.0305$, $k_s = 2.9$mm, $n1=6$, $n2=17$

Location 4 is about 12 times the uniform depth downstream of the roughness transition. The flow depth is uniform. The results for $\Delta y / d_{90}$, k_s, and τ_b are 0.32, 2.9 mm, and 1.56 N/m^2, respectively. The bed shear stress determined using the log law method is about 12% higher than the value of 1.36 N/m^2 obtained using the depth-slope method.
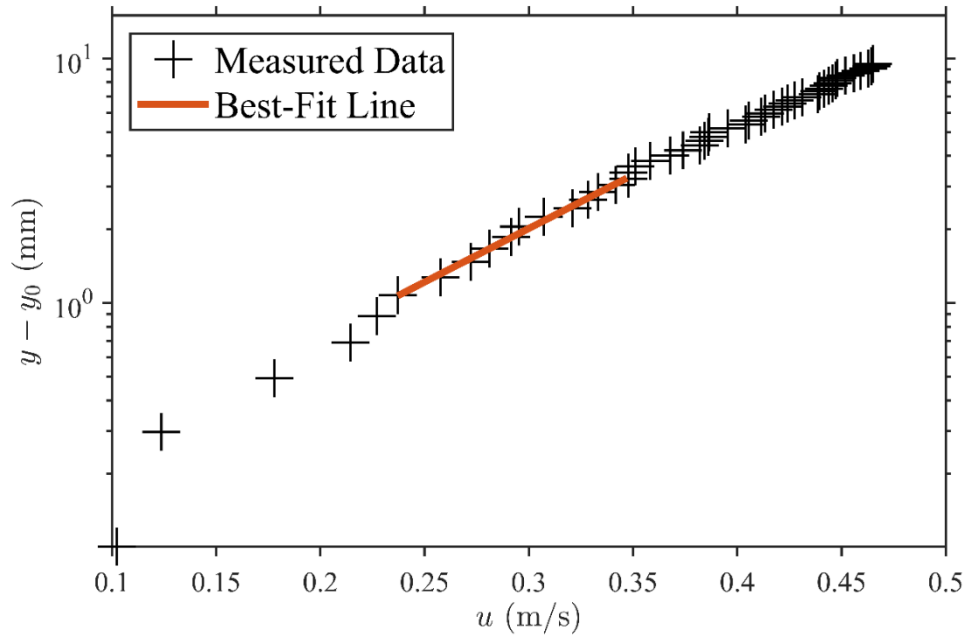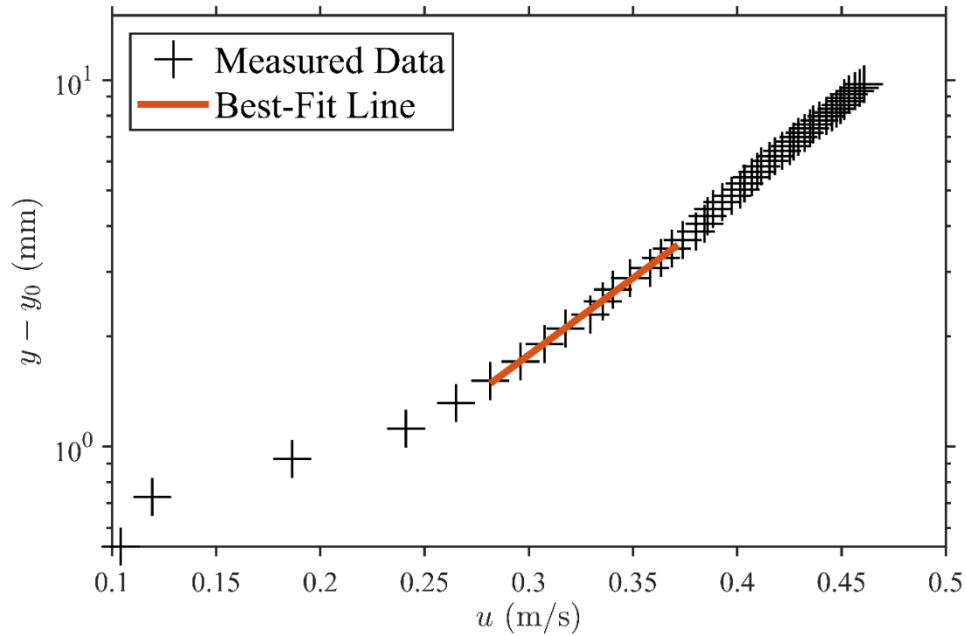
Figure 4.29 Mean velocity profile at location 5 in semi log plot; $u* = 0.0414$ m/s, $\tau_b = 1.70$ N/m^2, $r^2 = 0.997$, $rmse = 0.0154$, $k_s = 2.9$ mm, $n1=6$, $n2=17$

Location 5 is about 25 times the uniform depth downstream of the roughness transition, and the flow depth is uniform. The results for $\Delta y/d_{90}$, k_s, and τ_b are 0.67, 2.9 mm, and 1.70 N/m^2, respectively. The bed shear stress determined using the log law method is about 20% higher than the value of 1.36 N/m^2 obtained using the depth-slope method.
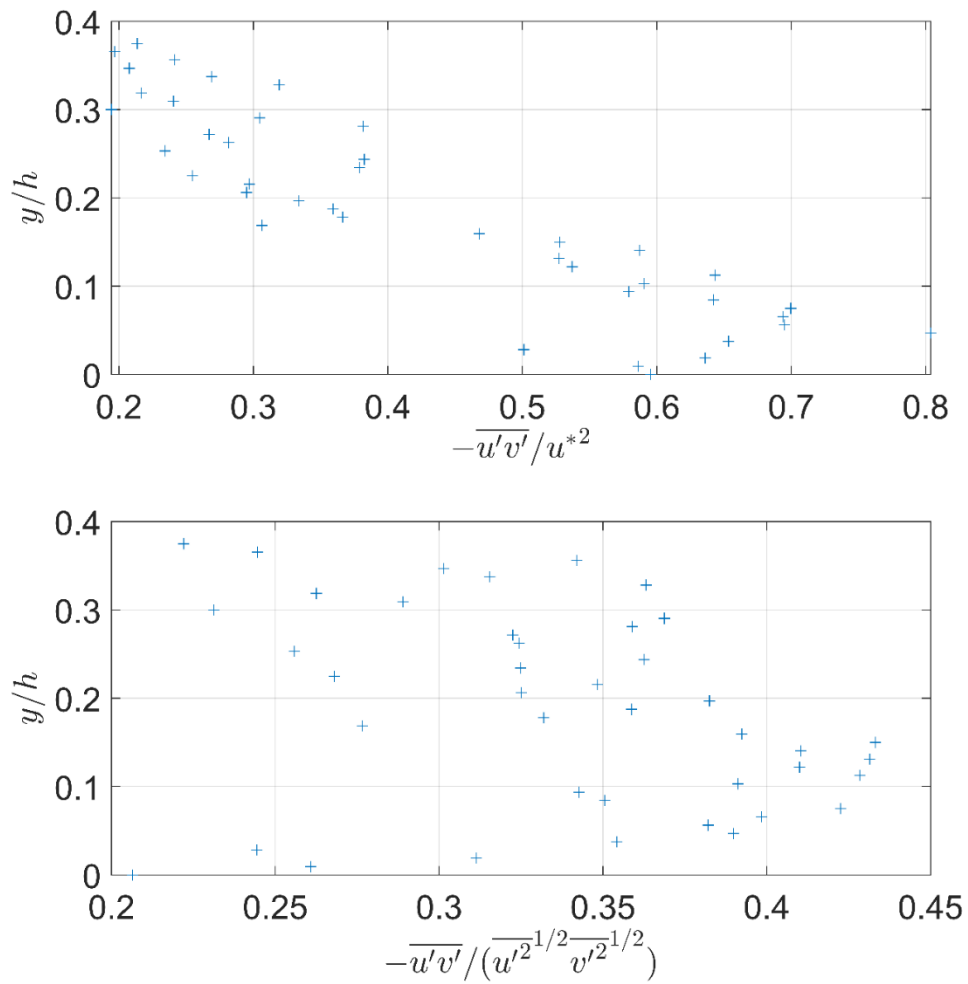
Figure 4.30 Measured Reynolds stress profile at location 1; $u^* = 0.0396$ m/s (from log law), $h = 20.9$ mm

Figure 4.30 is a plot of $-\overline{u'v'}/u^*$ versus y/h at location 1, with $h = 20.9$ mm denoting the effective flow depth. The Reynolds stress distribution has large scatter because the ensemble average was computed with fewer than 300 valid velocity fields out of 900 obtained from the three trials. Because of this, the bed shear stress was not determined by Reynolds stress extrapolation.
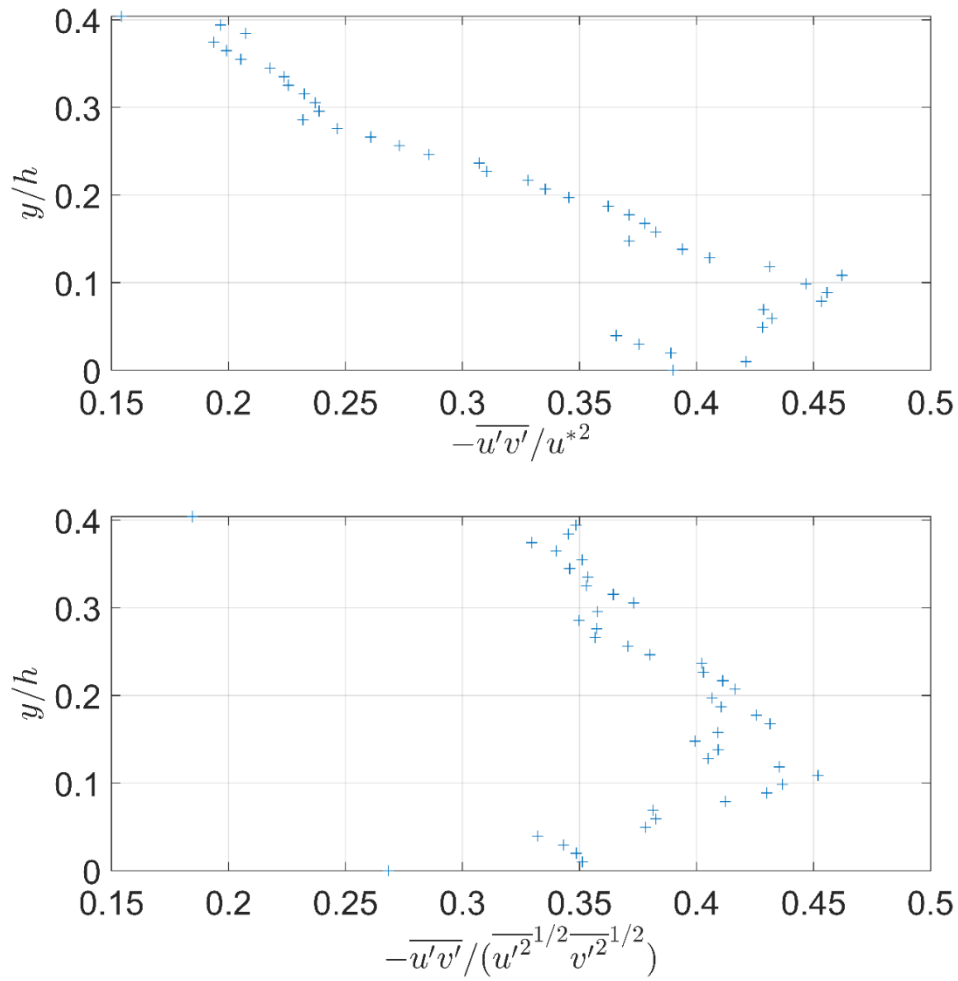
Figure 4.31 Measured Reynolds stress profile at location 2; u^* = 0.0465 m/s (from log law), h = 19.8 mm

Figure 4.31 is a plot of the normalized Reynolds stress $-\overline{u'v'}/u^*$ versus dimensionless distance y/h at location 2, where h (= 19.8 mm) denotes the effective flow depth. The Reynolds stress method was not used to determine the bed shear stress because the flow depth was non-uniform under the M2 profile.

Figure 4.32 Measured Reynolds stress profile at location 3; τ_b = 1.19 N/m^2 (u_r^* = 0.0346 m/s), h = 16.8 mm

Figure 4.32 is a plot of the normalized Reynolds stress $-\overline{u'v'}/u_r^{*2}$ versus dimensionless distance y/h at location 3, where h (= 16.8 mm) denotes the effective flow depth. A value of τ_b = 1.19 N/m^2 is found for the bed shear stress by linearly extrapolating a best-fit line through the data points to y =0. The bed shear stress obtained from the Reynolds stress method is much lower than the value of 2.11 N/m^2 obtained using the log law method.

Figure 4.33 Measured Reynolds stress profile at location 4; u^* = 0.0396 m/s (from log law), h = 16.8 mm

Figure 4.33 presents the distribution of $-\overline{u'v'}/u^*$ at location 4 about 12 times the normal depth after the roughness transition with $h = 16.8$ mm. The measured data are very scattered. This is because there are fewer than 300 valid vector fields for computing the Reynolds stress. Thus, the bed shear stress was not determined using the Reynolds stress method.
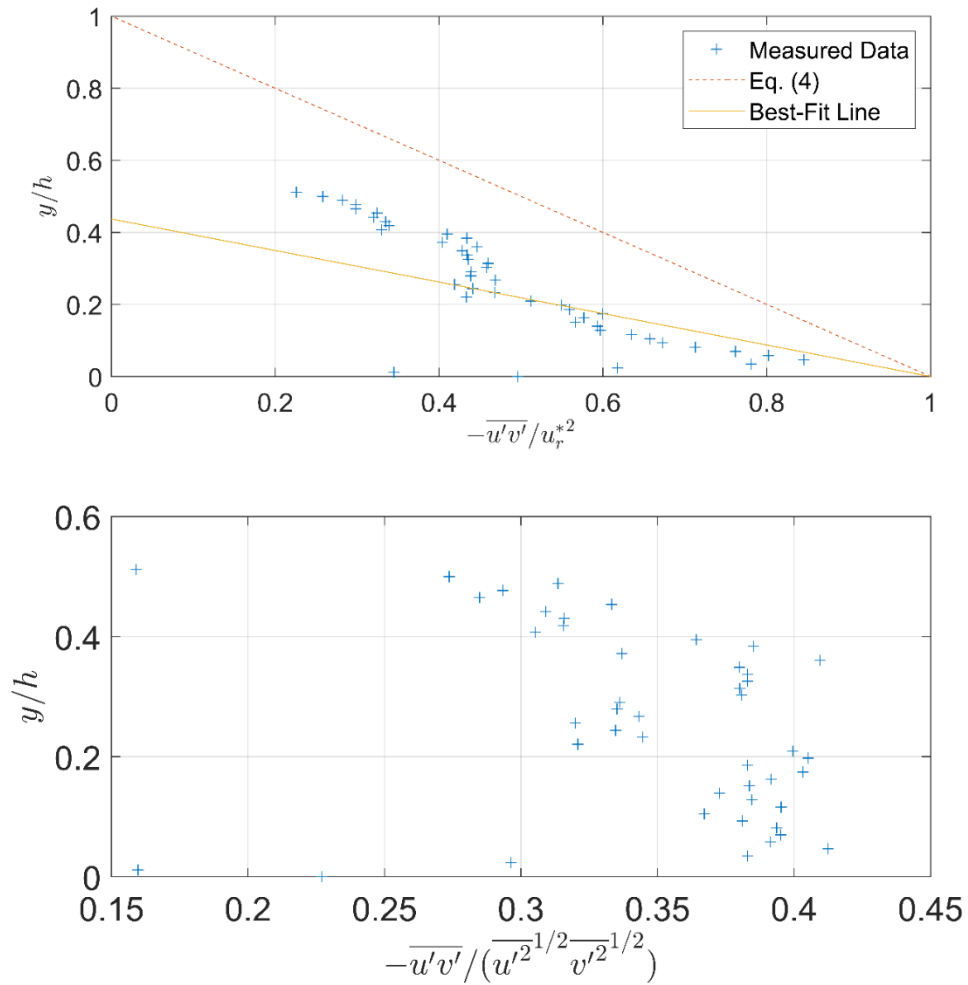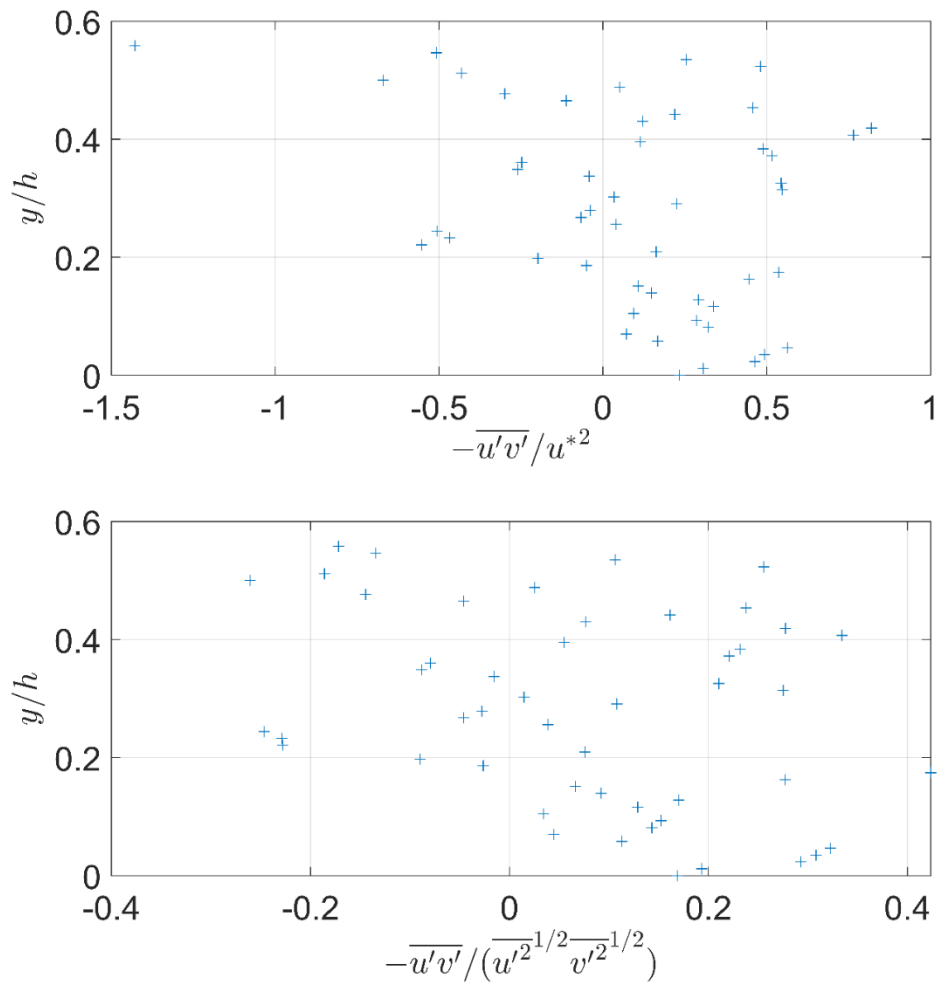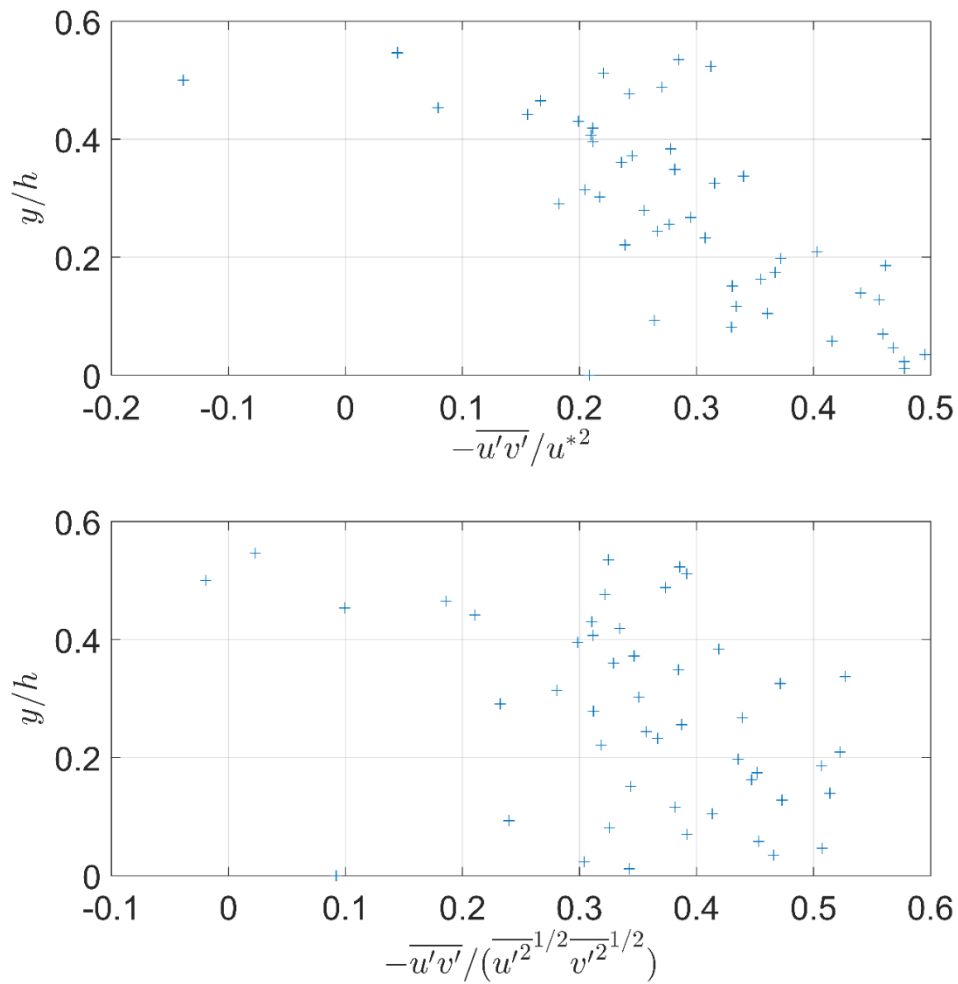
Figure 4.34 Measured Reynolds stress profile at location 5; $u^* = 0.0414$ m/s (from log law), $h = 16.8$ mm

Figure 4.34 is a plot of the normalized Reynolds stress $-\overline{u'v'}/u^*$ versus dimensionless distance y/h at location 5, where h ($= 16.8$ mm) is the effective flow depth. The measured Reynolds stress $-\overline{u'v'}/u^*$ exhibits a considerable amount of scatter. Therefore, the bed shear stress was not determined using the Reynolds stress method. The correlation between u' and v' (lower plot) also exhibits a significant amount of scatter, with values considerably below the range of 0.4 to 0.5 observed in fully turbulent flow in open channels.

Table 4.6 Summary of bed shear stress values (in N/m^2) obtained using various methods in case C

Location	1	2	3	4	5
Bed Material	Gravel	Gravel	Sand	Sand	Sand
Water Surface Profile	N	M2	N	N	N
τ_b (Eq. 1)	1.72	NA	1.36	1.36	1.36
τ_b (Eq. 2)	NA	NA	NA	NA	NA
τ_b (Eq. 3)	1.56	2.15	2.11	1.56	1.7
τ_b (Eq. 4)	NA	NA	1.19	NA	NA

Table 4.6 summarizes the bed shear stresses at the five measurement locations obtained using various methods. While examining the results from Eq. (3) it is evident that in Channel 1, location 2 has a lower water depth than location 1, resulting in higher bed shear stress at location 2. In Channel 2, the water surface elevation exhibits an N curve. The measured bed shear stress at locations 4 and 5 does not differ significantly. The bed shear stress at location 3 is higher than at locations 4 and 5, possibly due to flow history effect carrying from the gravel bed upstream.

4.4   Case D

In case D, the water surface profile changed from an N curve on a smooth bed to an S3 curve on a bed made of glass beads. Table 4.7 summarizes the flow conditions at the five PIV measurement locations, and Figure 4.35 shows the measured water surface profile through the transition.

Table 4.7 Experimental conditions in case D

Location	1	2	3	4	5
Distance from Transition Point (mm)	-162	-32	32	262	397
Bed Material	Acrylic	Acrylic	Glass Bead	Glass Bead	Glass Bead
Water Surface Profile	N	N	S3	N	N
Flow Condition	Supercritical	Supercritical	Supercritical	Supercritical	Supercritical
Froude Number	1.50	1.45	1.32	1.21	1.26
Flow Depth h (mm)	27.9	28.7	30.5	32.3	31.5
$\dfrac{w}{h}$	5.5	5.3	5.0	4.7	4.8

Note: Distance is measured from the roughness transition to the center of the FOV of the PIV camera
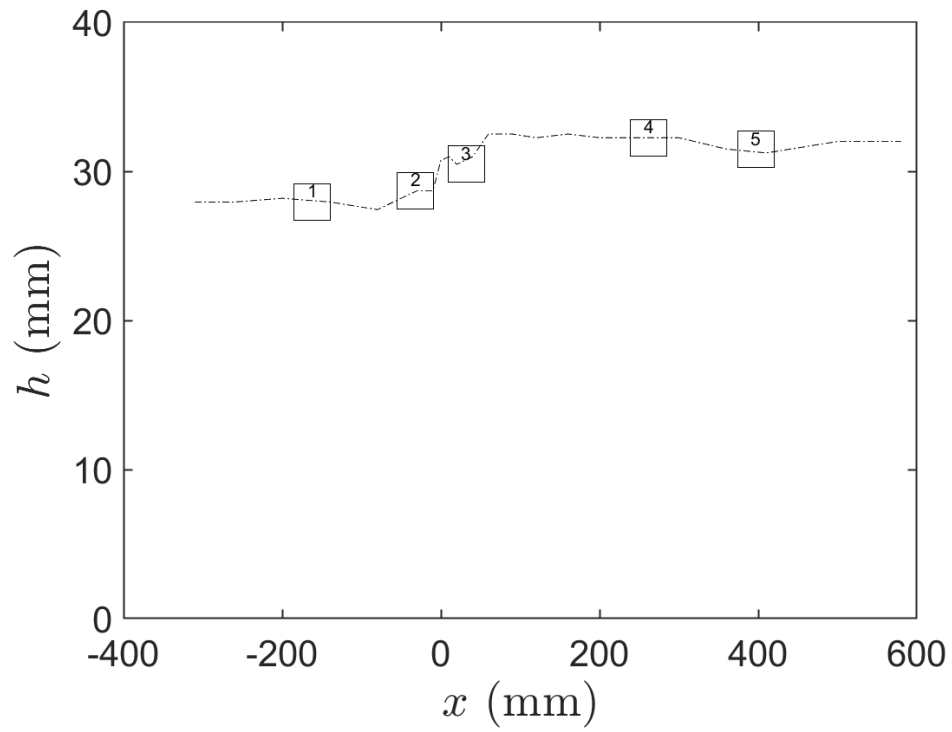
Figure 4.35 Measured water surface profile in case D. The origin $x = 0$ represents the transition point, and $\boldsymbol{h}$ is the effective depth. Negative distance indicates the acrylic bed section when going upstream, and positive distance represents the glass bead section when going downstream. The location of each FOV is marked in the figure.
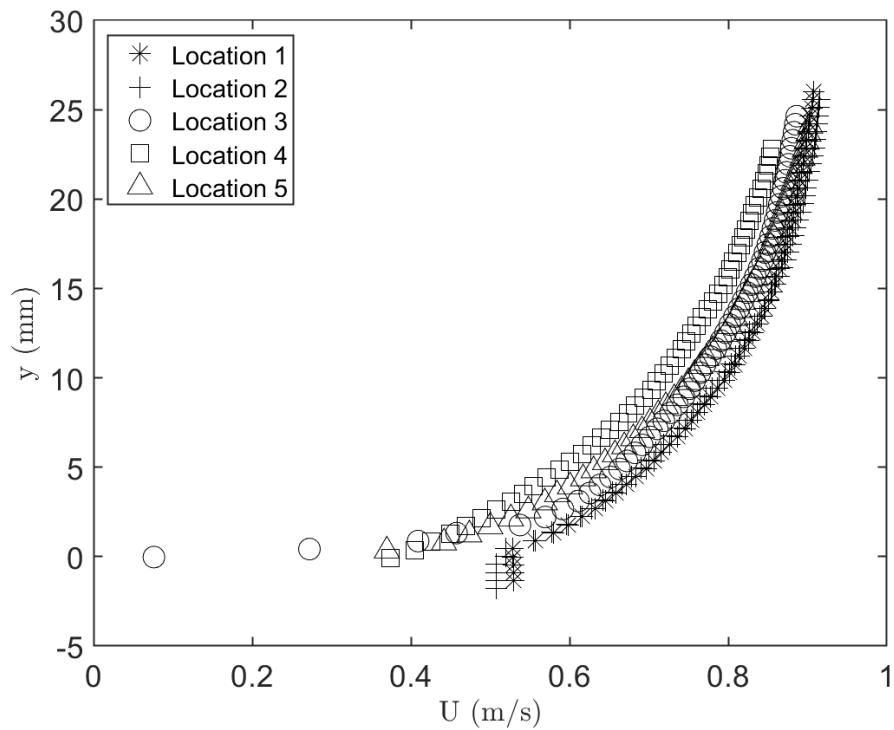
Figure 4.36 Mean velocity profiles at different channel locations

Figure 4.36 shows the measured velocity profiles from upstream (location 1) to downstream (location 5). The velocity profiles at locations 1 and 2 are similar, which is consistent with the uniform flow in Channel 1. At location 3 after the transition, measured velocities decrease adjacent to the bed due to the increase in bed roughness but also away from the bed due to the increase in flow depth. Flow velocity continues to decrease from location 3 to location 4 due to the increase in flow depth. The measured velocities are slightly higher at location 5 than at location 3, but the differences are not large and could be caused by small variations in the flow depth or non-uniform velocity distribution across the narrow channel.
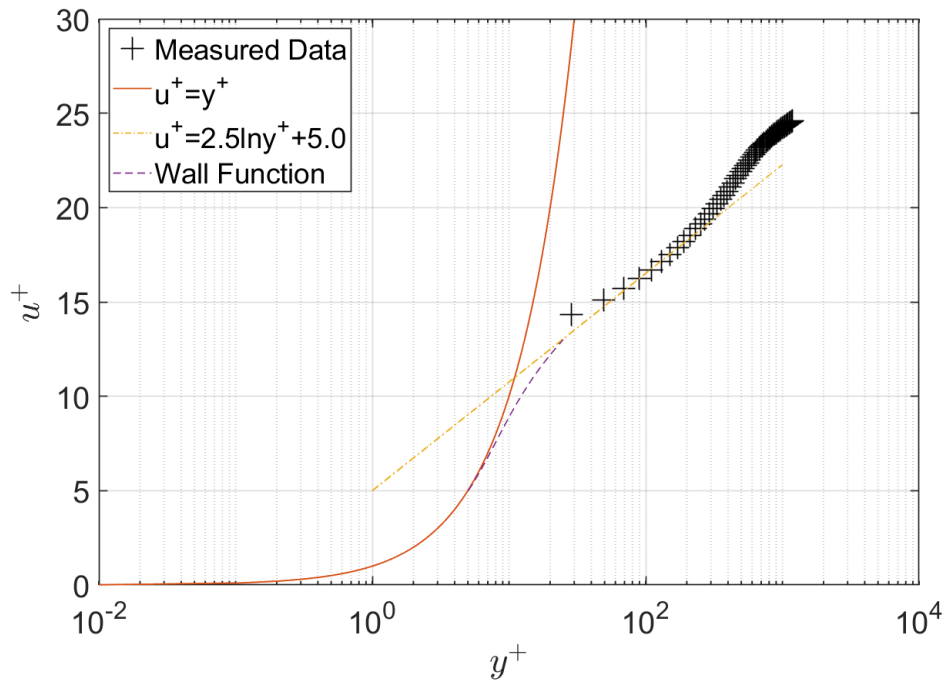
Figure 4.37 Mean velocity profile at location 1 in semi log plot; $u* = 0.0369$ m/s, $\tau_b = 1.36$ N/m^2

At location 1, the water surface profile follows an N curve. Figure 4.37 shows that the logarithmic law is fully established. The bed shear stress obtained using the log law is 32% lower compared with a bed shear stress of 1.80 N/m² obtained using the depth-slope method.
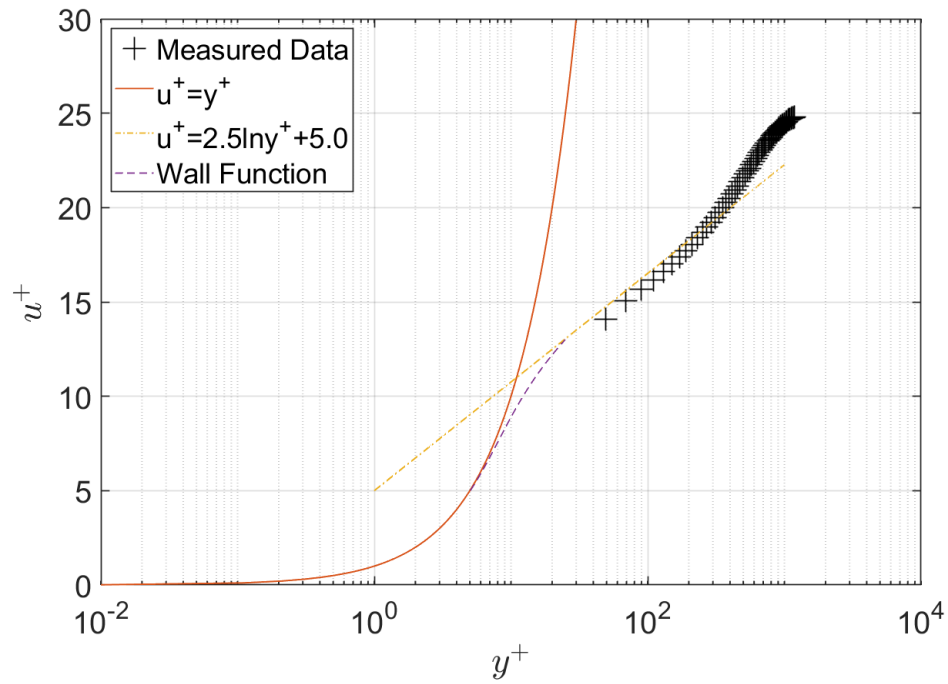
Figure 4.38 Mean velocity profile at location 2 in semi log plot; $u* = 0.0369$ m/s, $\boldsymbol{\tau_b} = 1.36$ N/m^2

At location 2, the water surface profile follows an N curve. Figure 4.38 shows that the logarithmic law is fully established. The bed shear stress obtained using the log law is the same as that at location 1 and is 35% lower than the bed shear stress ($\tau_b = 1.83$ N/m²) obtained using the depth-slope method.
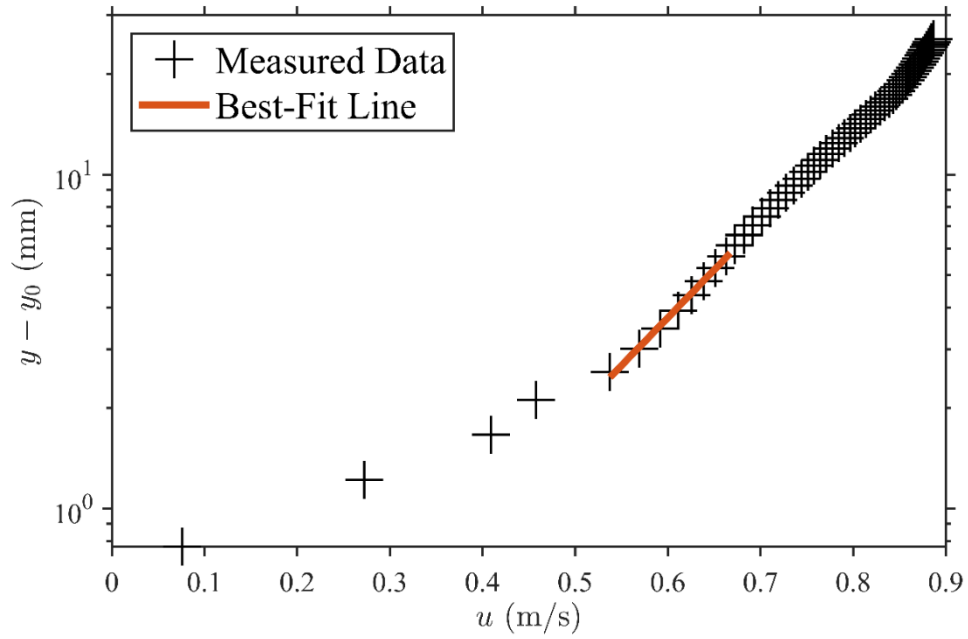
Figure 4.39 Mean velocity profile at location 3 in semi log plot; $u* = 0.0607$ m/s, $\boldsymbol{\tau_b} = 3.67$ N/m^2, $r^2 = 0.995$, *rmse = 0.022*, $\boldsymbol{k_s} = 2.1$ mm, *n1 = 5, n2 =13*

Location 3 is located just after the roughness transition. The water surface profile exhibits an S3 curve and Eq. (1) is not valid in this region. The results for $\Delta y/d_{90}$, k_s, and τ_b obtained using Eq. (3) are 0.79, 2.1 mm, and 3.67 N/m^2, respectively.
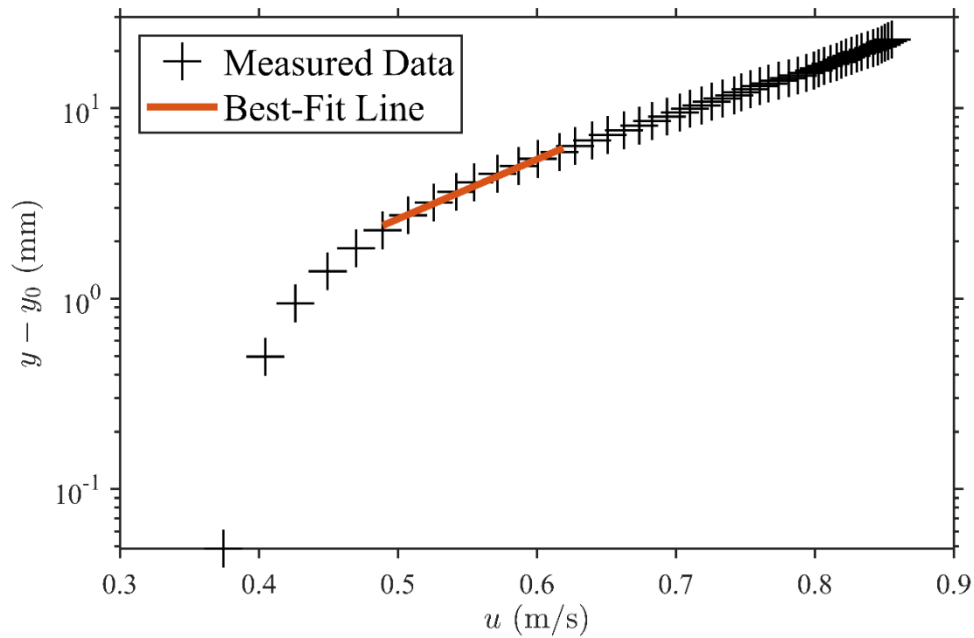
Figure 4.40 Mean velocity profile at location 4 in semi log plot; $u* = 0.0555$ m/s, $\boldsymbol{\tau_b} = 3.07$ N/m², $r^2 = 0.995$, *rmse* $= 0.0348$, $\boldsymbol{k_s} = 2.1$ mm, *n1* $= 6$, *n2* $= 15$

The water surface profile at location 4 exhibits an N curve. The results for $\Delta y/d_{90}$, k_s, and τ_b obtained using Eq. (3) are 0.49, 2.1 mm, and 3.07 N/m², respectively. The local bed shear stress obtained using the log law method is much higher than the bed shear stress of 2.31 N/m² obtained using the depth-slope method.
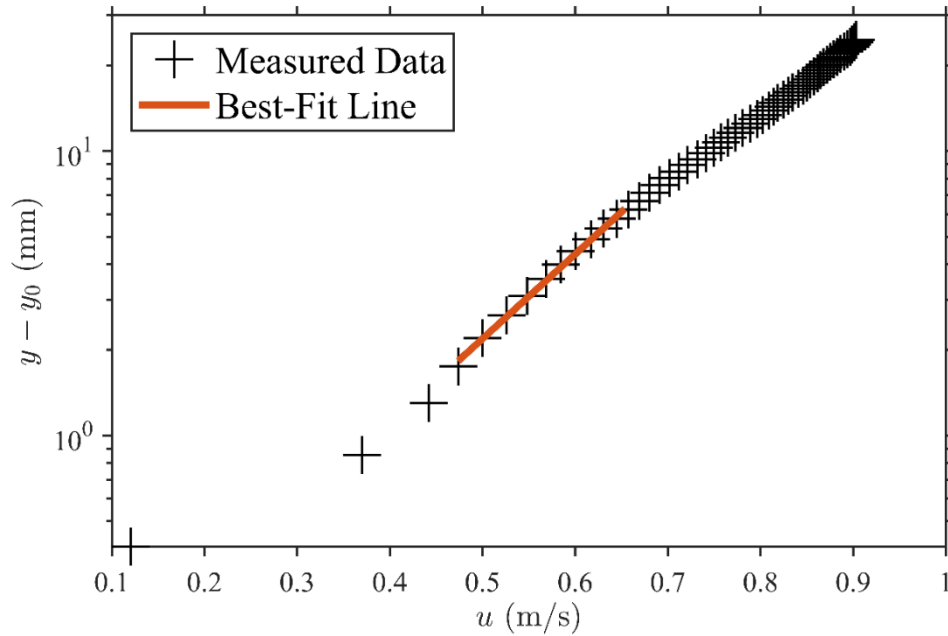
Figure 4.41 Mean velocity profile at location 5 in semi log plot; $u^* = 0.0584$ m/s, $\boldsymbol{\tau_b} = 3.4$ N/m^2, $r^2 = 0.997$, *rmse* = 0.0227, $\boldsymbol{k_s} = 2.1$ mm, *n1* = 4, *n2* = 14

The water source surface profile at location 5 exhibits an N curve. The results for $\Delta y/d_{90}$, k_s, and τ_b obtained using Eq. (3) are 0.52, 2.1 mm, and 3.4 N/m^2, respectively. As with location 4, the local bed shear stress obtained using the log law method is much higher than the bed shear stress obtained using the depth-slope method (2.22 N/m^2).
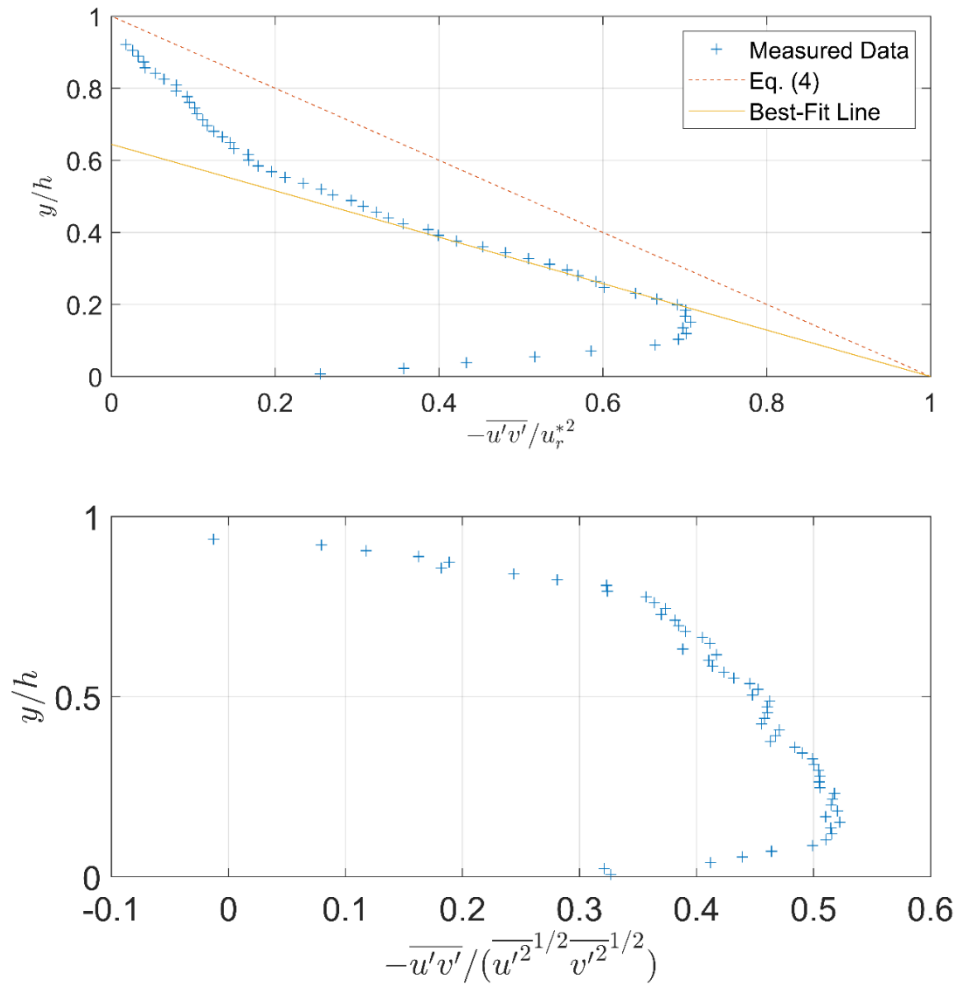
Figure 4.42 Measured Reynolds stress profile at location 1; τ_b = 1.18 N/m² (u_r^* = **0.0344** m/s), $h = 27.9$ mm

Figure 4.42 is a plot of $-\overline{u'v'}/u_r^{*2}$ versus y/h at location 1 , with $h = 27.9$ mm. The bed shear stress obtained by extrapolating the measured Reynolds stresses to the bed is 1.18 N/m², which is lower than the value of 1.36 N/m² obtained using Eq. (2). It is also seen that the decrease in $-\overline{u'v'}/u_r^{*2}$ is faster in the lower half of the water column but slower near the free surface than predicted by Eq. (4). The shape of the measured Reynolds stress distribution is like that described in Auel et al. (2014) for supercritical flows in narrow channels and is attributed to the presence of secondary currents. The latter occurs when the w/h ratio is less than 5. The ratio of w/h is around 5 in case D, therefore sidewall and three-dimensional flow effects were likely present.
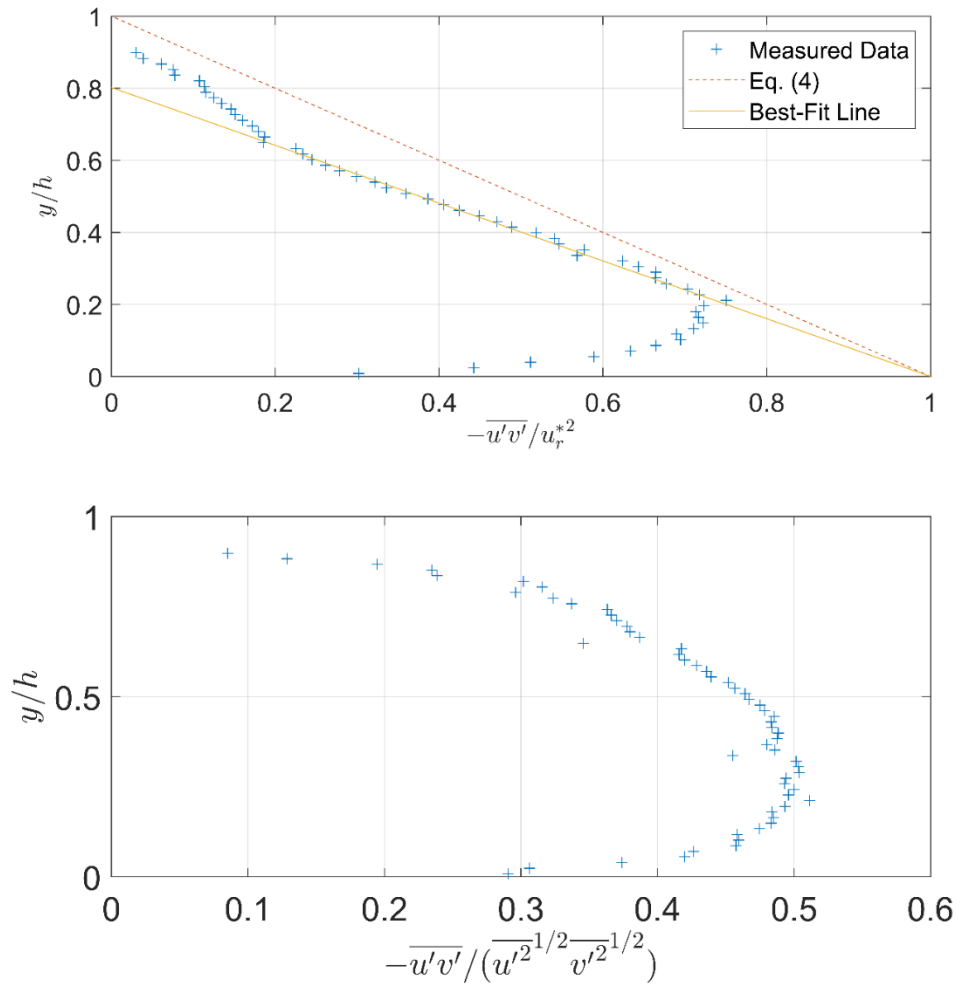
Figure 4.43 Measured Reynolds stress profile at location 2; τ_b = 1.12 N/m² (u_r^* = **0.0335** m/s), h = 28.7 mm

Figure 4.43 is a plot of $-\overline{u'v'}/u_r^{*2}$ versus y/h at location 2, with h = 28.7 mm. The bed shear stress obtained by extrapolating the measured Reynolds stresses to the bed is 1.12 N/m². The latter is essentially the same as the value of 1.18 N/m² obtained at location 1 since the flow is uniform.
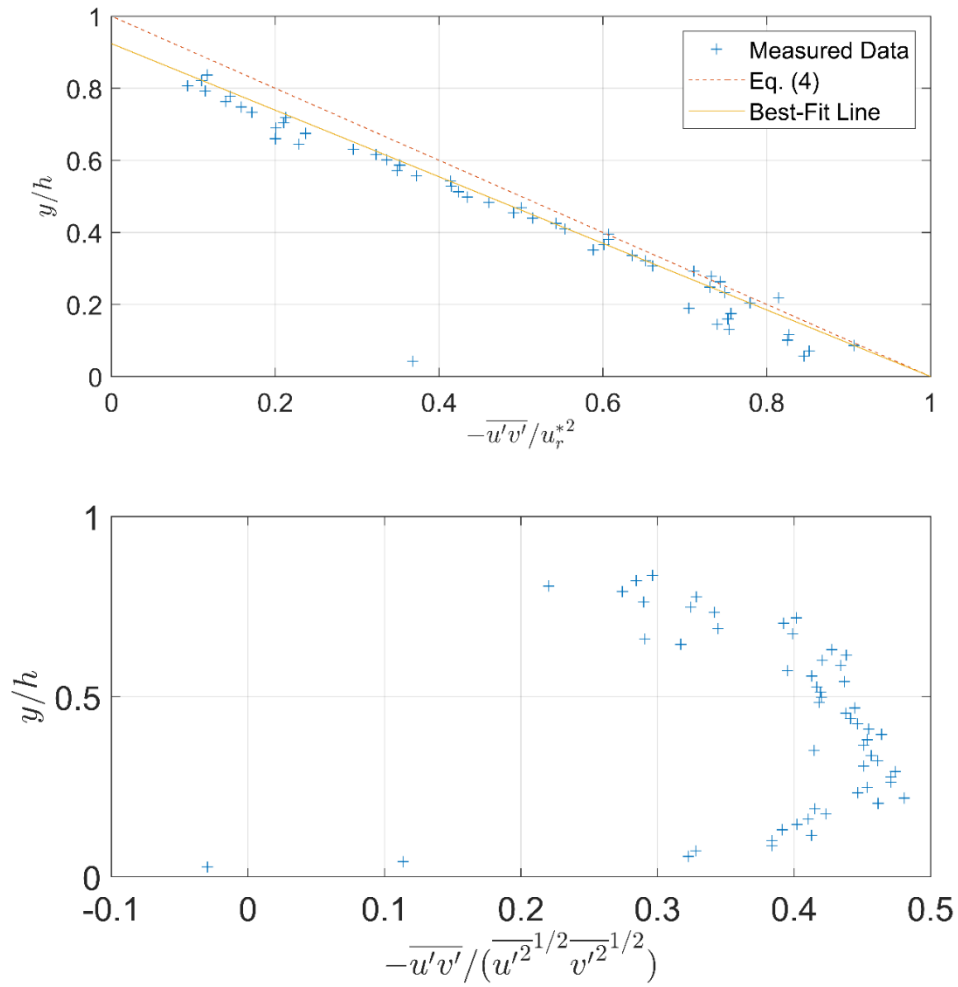
Figure 4.44 Measured Reynolds stress profile at location 3; $\tau_b = 1.12$ N/m^2 ($u_r^* = 0.0335$ m/s), $h = 30.5$ mm

Figure 4.44 is a plot of $-\overline{u'v'}/u_r^{*2}$ versus y/h at location 3, with $h = 30.5$ mm. The bed shear stress obtained by extrapolating the measured Reynolds stresses to the bottom is 1.12 N/m^2.
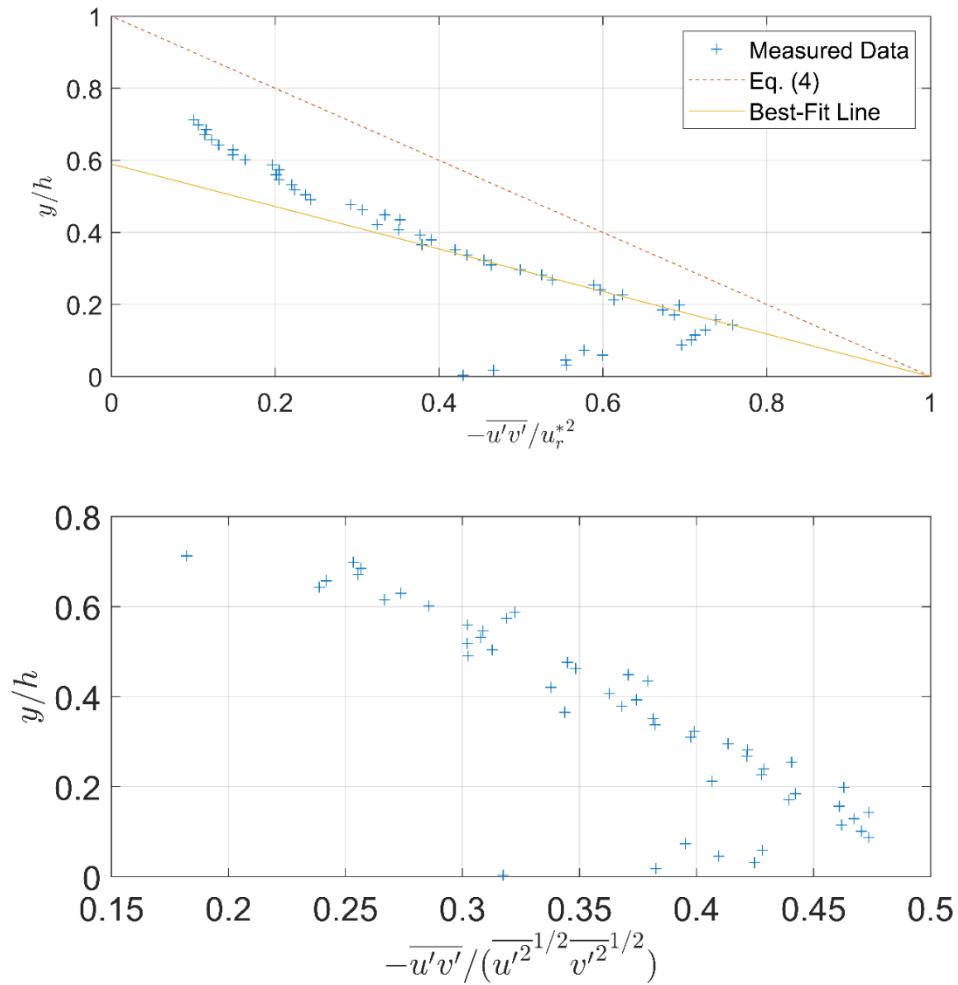
Figure 4.45 Measured Reynolds stress profile at location 4; τ_b = 1.98 N/m² (u_r^* = 0.0446 m/s), h = 32.3 mm

Figure 4.45 is a plot of $-\overline{u'v'}/u_r^{*2}$ versus y/h at location 4, with $h = 32.3$ mm. The bed shear stress obtained by extrapolating the measured Reynolds stresses to the bottom is 1.98 N/m², which is much lower than the value of 3.07 N/m² obtained using log law method.
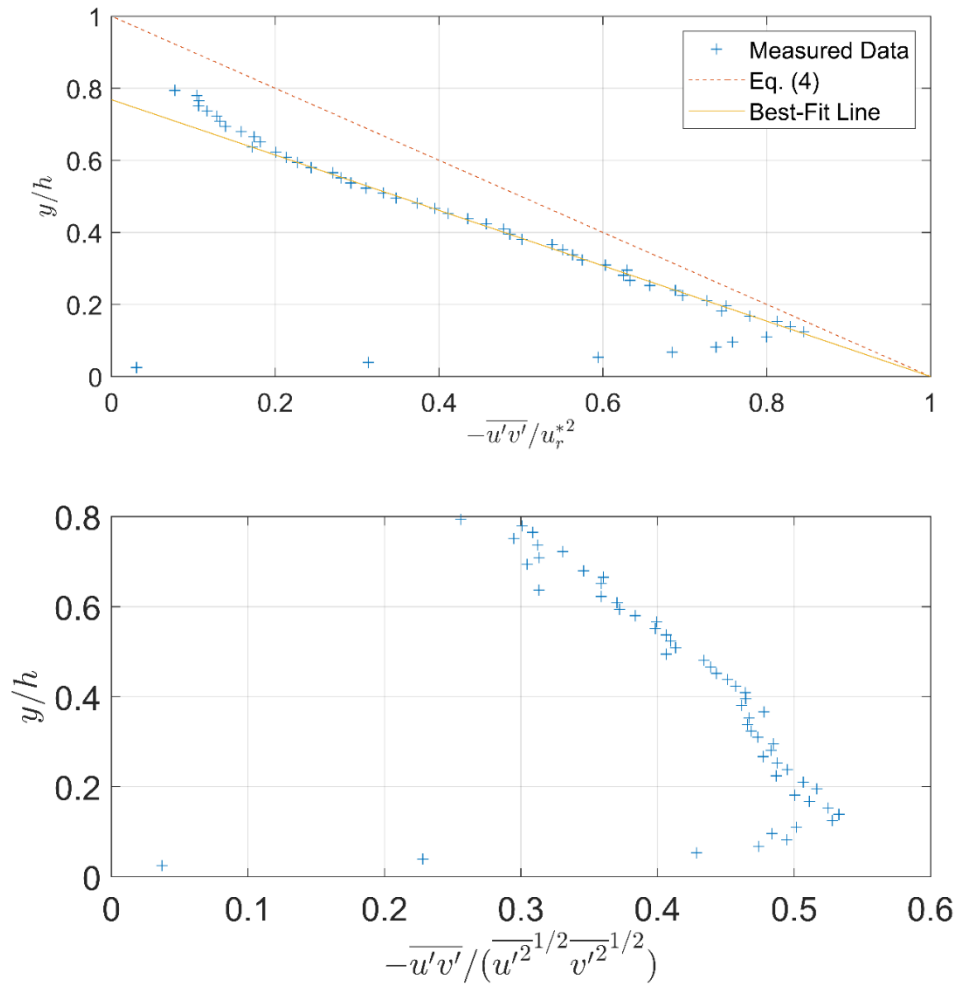
Figure 4.46 Measured Reynolds stress profile at location 5; τ_b = 1.91 N/m^2 ($u_r^* = 0.0438$ m/s), h = 31.5 mm

Figure 4.46 is a plot of $-\overline{u'v'}/u_r^{*2}$ versus y/h at location 2, with h = 31.5 mm. The bed shear stress obtained by extrapolating the measured Reynolds stresses to the bottom is 1.91 N/m^2.

Table 4.8 Summary of bed shear stress values (in N/m^2) obtained using various methods in case D

Location	1	2	3	4	5
Bed Material	Acrylic	Acrylic	Glass Bead	Glass Bead	Glass Bead
Water Surface Profile	N	N	S3	N	N
τ_b (Eq. 1)	1.80	1.83	NA	2.31	2.22
τ_b (Eq. 2)	1.36	1.36	NA	NA	NA
τ_b (Eq. 3)	NA	NA	3.67	3.07	3.4
τ_b (Eq. 4)	1.18	1.12	1.12	1.98	1.91

Table 4.8 summarizes the bed shear stresses at the five measurement locations obtained using the various methods. Locations 1 and 2 have similar bed shear stress values because the water depth is uniform in Channel 1. In Channel 2, the results from Eq. (3) show that location 3 has a higher bed shear stress than at locations 4 and 5 due to the increasing flow depth under the S3 profile, whereas the bed shear stress is similar at locations 4 and 5 due to the uniform depth. The bed shear stress variation obtained using Eq. (4) follows a similar trend except at location 3. The latter may be attributed to Eq. (4) being only valid in uniform flow. It is also seen that Eq. (4) produces lower bed shear stress values compared with the other methods.

4.5 Case E

In case E, the water surface profile changes from an M1 curve to an N curve as the flow transitions from a sand bed to a gravel bed. Table 4.9 summarizes the flow conditions at the four PIV measurement locations, and Figure 4.47 shows the measured water surface profile from upstream to downstream.

Table 4.9 Experimental conditions in case E

Location	1	2	3	4
Distance from Transition Point (mm)	-132	-22.5	22	292
Bed Material	Sand	Sand	Gravel	Gravel
Water Surface Profile	M1	M1	N	N
Flow Condition	Subcritical	Subcritical	Subcritical	Subcritical
Froude Number	0.66	0.60	0.62	0.71
Flow Depth $h(mm)$	26.0	27.7	27.2	24.7
$\dfrac{w}{h}$	5.87	5.49	5.6	6.17

Note: Distance is measured from the roughness transition to the center of the FOV of the PIV camera
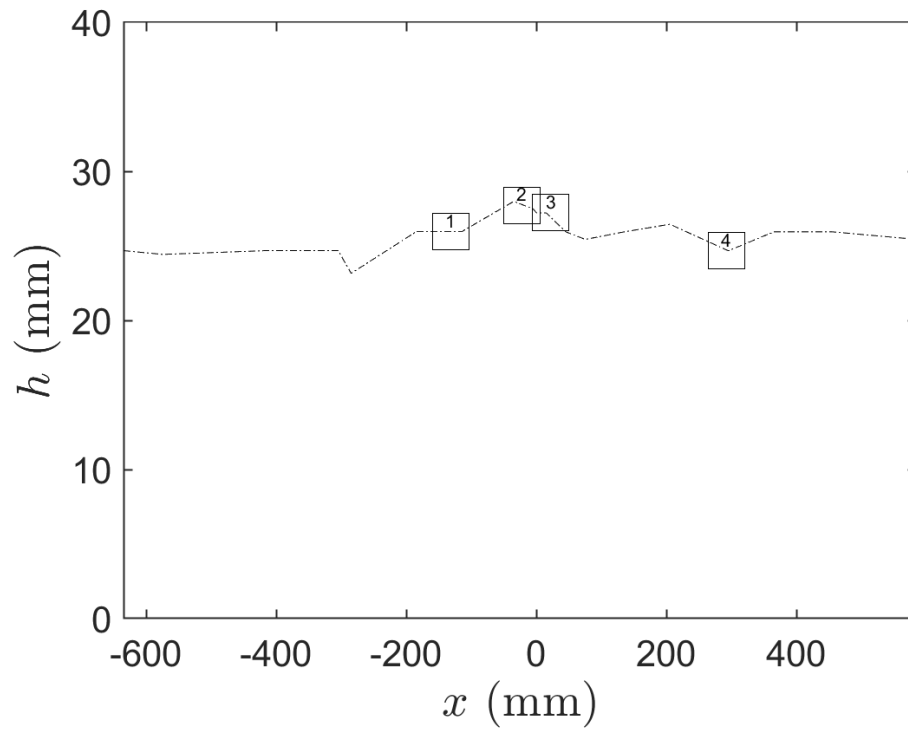
Figure 4.47 Measured water surface profile in case E. The origin $x = 0$ represents the transition point, and $\boldsymbol{h}$ is the effective depth. Negative distance indicates the sand bed section when going upstream, and positive distance represents the gravel bed section when going downstream. The location of each FOV is marked in the figure.
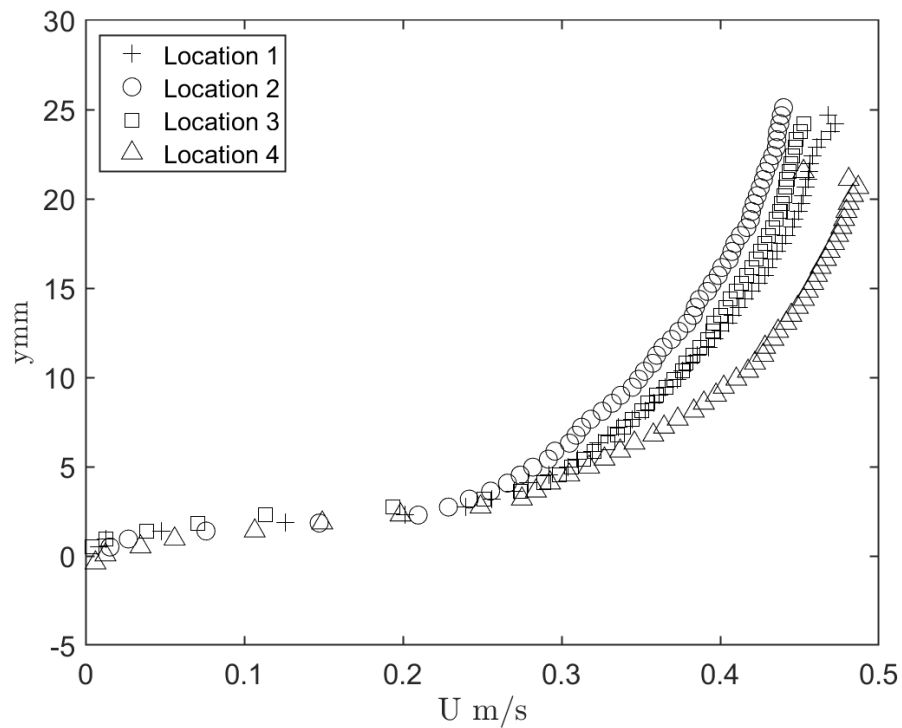
Figure 4.48 Mean velocity profiles at different channel locations

Figure 4.48 shows the mean velocity profiles at the different measurement locations. Flow velocity decreases from location 1 to location 2 due to the increase in flow depth under the M1 profile. As the bed roughness increases, flow velocity decreases due to increase in bed friction. Therefore, the velocity near the bed decreases at locations 3 when compared with locations 1 and 2 but increases away from the bed to maintain conservation of mass. The large increase in velocity from location 3 to location 4 is not expected and may be related to the dip in the water surface profile at location 4 seen in Figure 4.47.
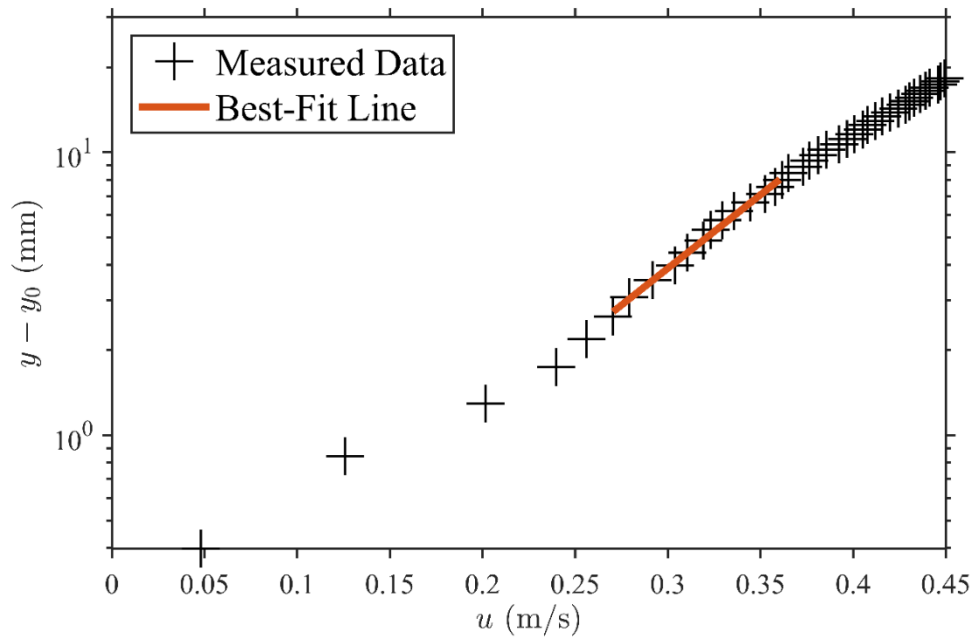
Figure 4.49 Mean velocity profile at location 1 in semi log plot; $u^* = 0.0334$ m/s, $\tau_b = 1.11$ N/m^2, $r^2 = 0.994$, $rmse = 0.0282$, $k_s = 3.2$ mm, $n1 = 8$, $n2 = 20$

Location 1 represents the upstream region where the water surface profile exhibits an M1 curve. Eq. (1) is not valid in this region. The results for $\Delta y / d_{90}$, k_s, and τ_b from Eq. (3) are 0.46, 3.2 mm, and 1.1 N/m^2, respectively.
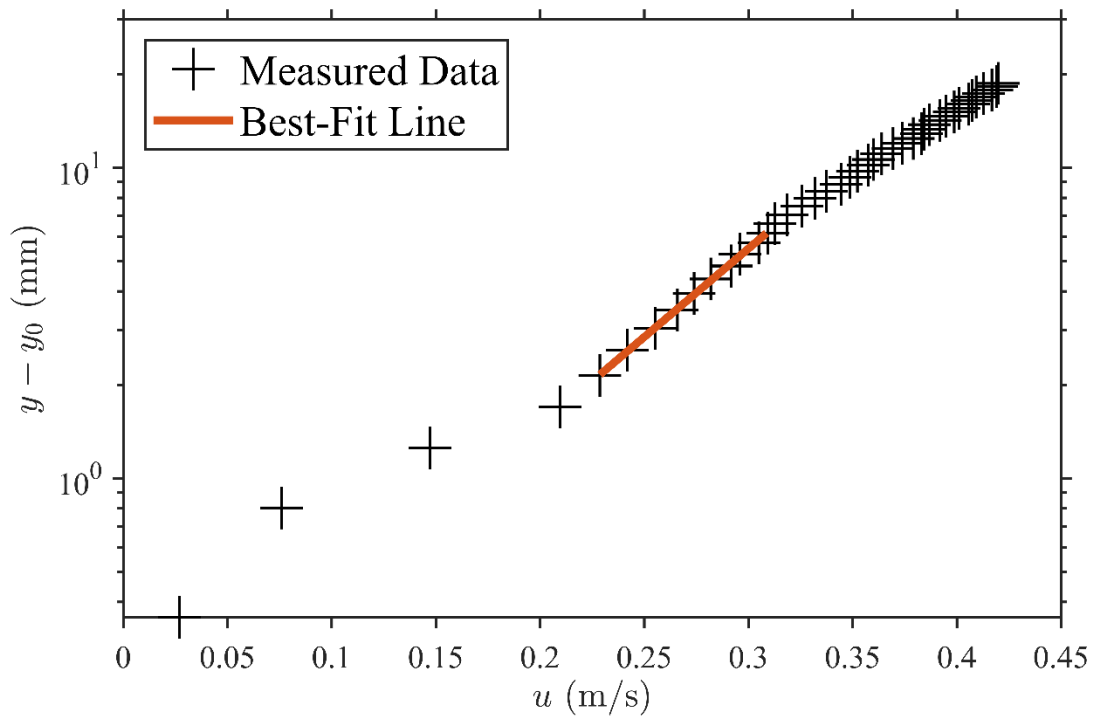
Figure 4.50 Mean velocity profile at location 2 in semi log plot; $u* = 0.0305$ m/s, $\tau_b = 0.93$ N/m^2,
$r^2 = 0.998$, $rmse = 0.0152$, $k_s = 3.2$ mm, $n1 = 6$, $n2 = 16$

Location 2 is the location right before the transition. The water surface profile exhibits an M1 curve.
The results for $\Delta y/d_{90}$, k_s, and τ_b from Eq. (3) are 0.7, 3.2 mm, and 0.93 N/m^2, respectively.

Figure 4.51 Mean velocity profile at location 3 in semi log plot; $u* = 0.0373$ m/s, $\tau_b = 1.39$ N/m^2, $r^2 = 0.998$, *rmse* $= 0.0096$, $\boldsymbol{k_s}$=5.80 mm, *n1=9, n2=16*

Location 3 is just downstream of the roughness transition. The water surface profile exhibits an N curve. The results for $\Delta y/d_{90}$, k_s, and τ_b from Eq. (3) are 0.96, 5.8 mm, and 1.39 N/m^2, respectively. The bed shear stress determined using the log law method is about 5% lower than the value of 1.46 N/m^2 obtained from the depth-slope method (Eq. 1).
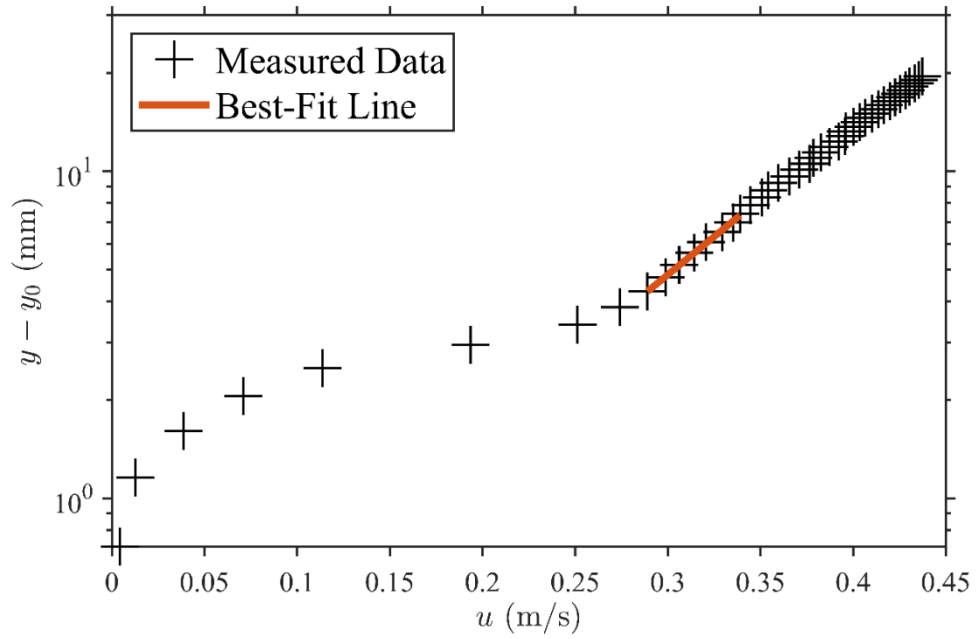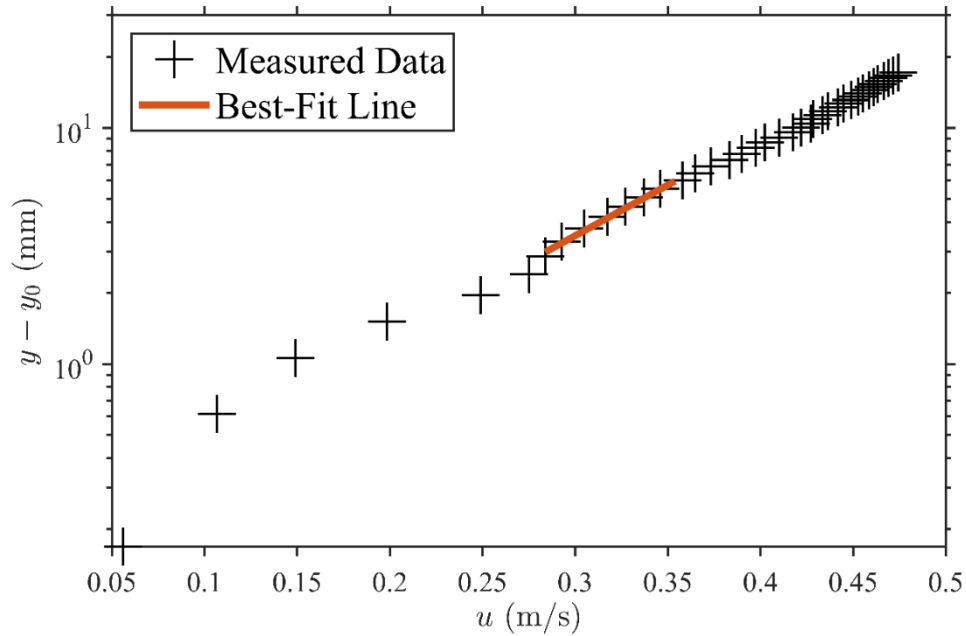
Figure 4.52 Mean velocity profile at location 4 in semi log plot; $u* = 0.0405$ m/s, $\tau_b = 1.63$ N/m^2, $r^2 = 0.991$, $rmse = 0.027$, $k_s = 5.4$ mm, $n1=11$, $n2=18$

Location 4 is located farther downstream from the roughness transition. The water surface profile exhibits an N curve. The results for $\Delta y/d_{90}$, k_s, and τ_b from Eq. (3) are 0.4, 5.40 mm, and 1.63 N/m^2, respectively. The bed shear stress obtained using the log law method is about 25% higher than the value of 1.3 N/m^2 obtained using the depth-slope method.
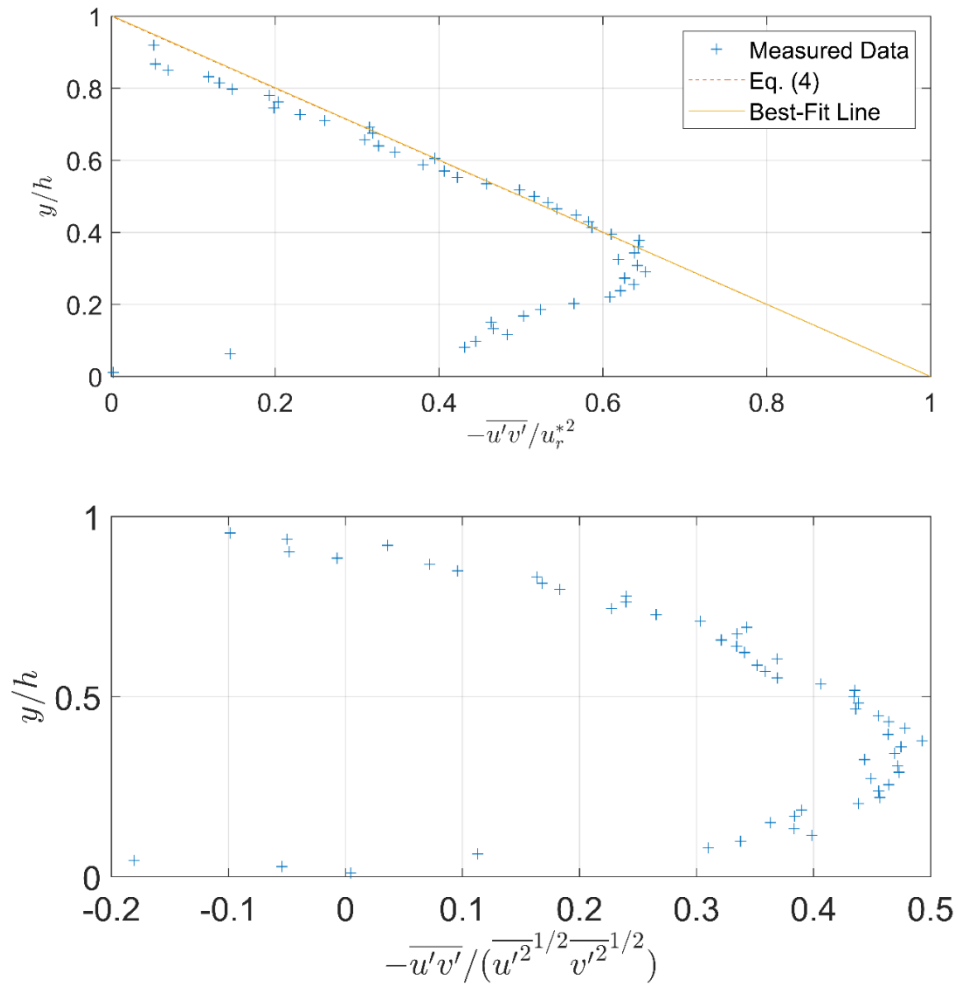
Figure 4.53 Measured Reynolds stress profile at location 1; τ_b = 0.86 N/m², (u_r^* = **0.0293** m/s), h = 25.6 mm

Figure 4.53 is a plot of $-\overline{u'v'}/u_r^{*2}$ versus y/h at location 1, with $h = 25.6$ mm. There is good correlation between the turbulence velocities u' and v'; the values of $R_{u'v'}$ away from the bed are between 0.4 and 0.5 (lower plot). The bed shear stress obtained by extrapolating the measured Reynolds stresses to the bottom is 0.86 N/m².
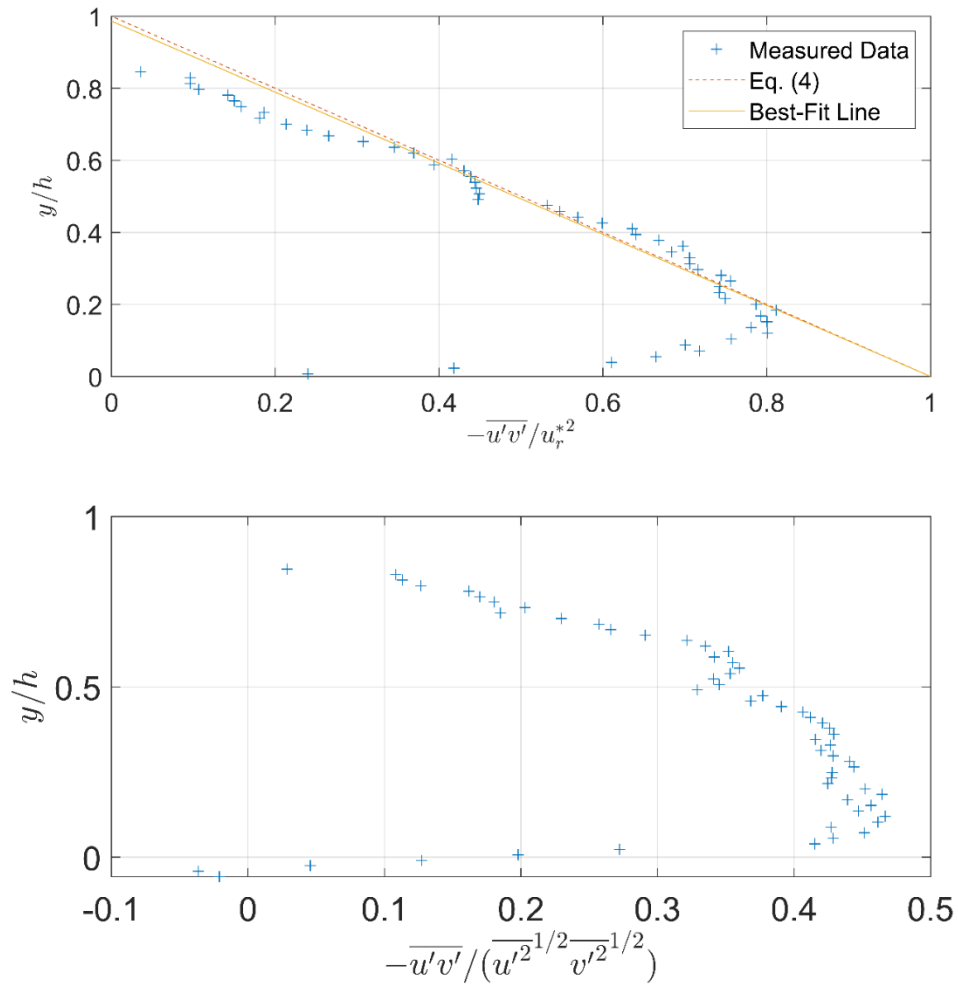
Figure 4.54 Measured Reynolds stress profile at location 2; τ_b = 0.67 N/m², (u_r^* = 0.0259 m/s), h = 27.7 mm

Fig. 4.54 is a plot of $-\overline{u'v'}/u_r^{*2}$ versus y/h at location 2, with $h = 27.7$ mm. There is good correlation between the turbulence velocities u' and v'; the values of $R_{u'v'}$ away from the bed are between 0.4 and 0.5 (lower plot). The bed shear stress obtained by extrapolating the measured Reynolds stress to the bottom is 0.67 N/m².
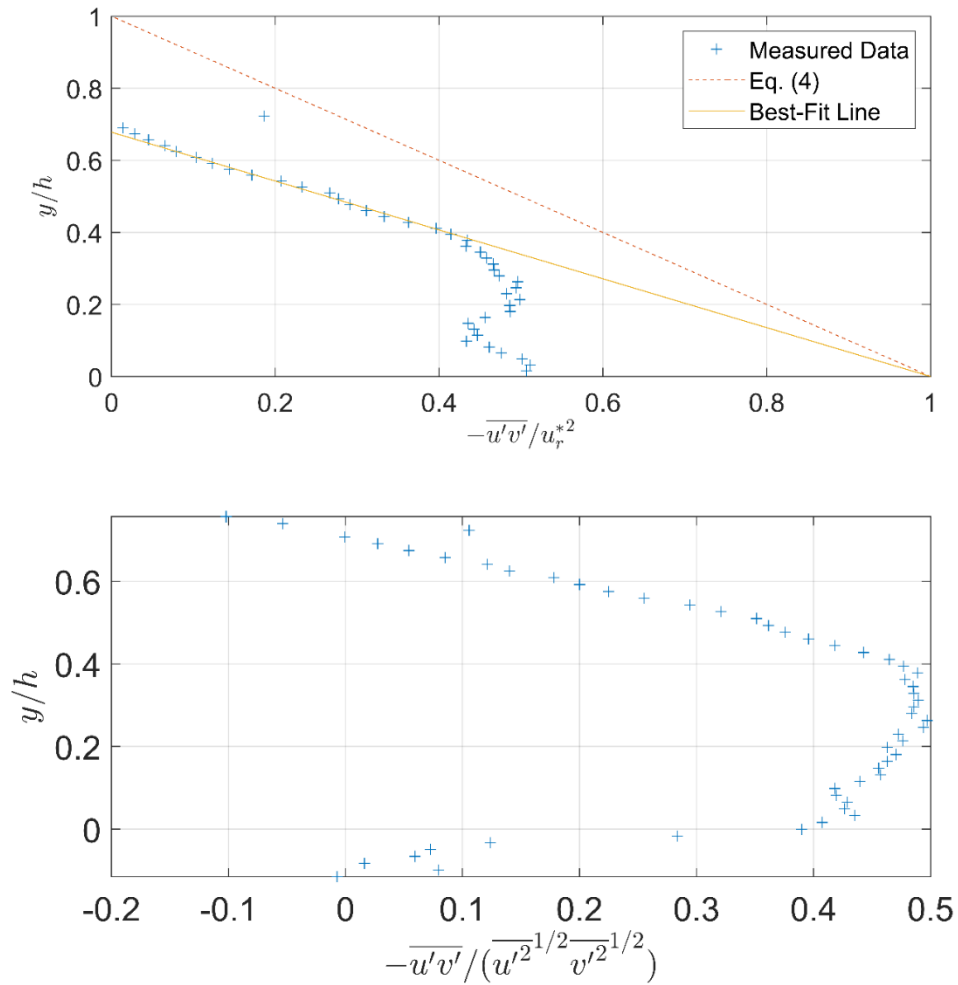
Figure 4.55 Measured Reynolds stress profile at location 3; τ_b = 1.07 N/m² ($\boldsymbol{u_r^*}$ = **0.0328** m/s), $\boldsymbol{h}$ = 27.2 mm

Figure 4.55 is a plot of $-\overline{u'v'}/u_r^{*2}$ versus y/h at location 3, with $h = 27.2$ mm. There is good correlation between the turbulence velocities u' and v'; the values of $R_{u'v'}$ away from the bed are between 0.4 and 0.5 (lower plot). The bed shear stress obtained by extrapolating the measured Reynolds stress to the bottom is 1.07 N/m².
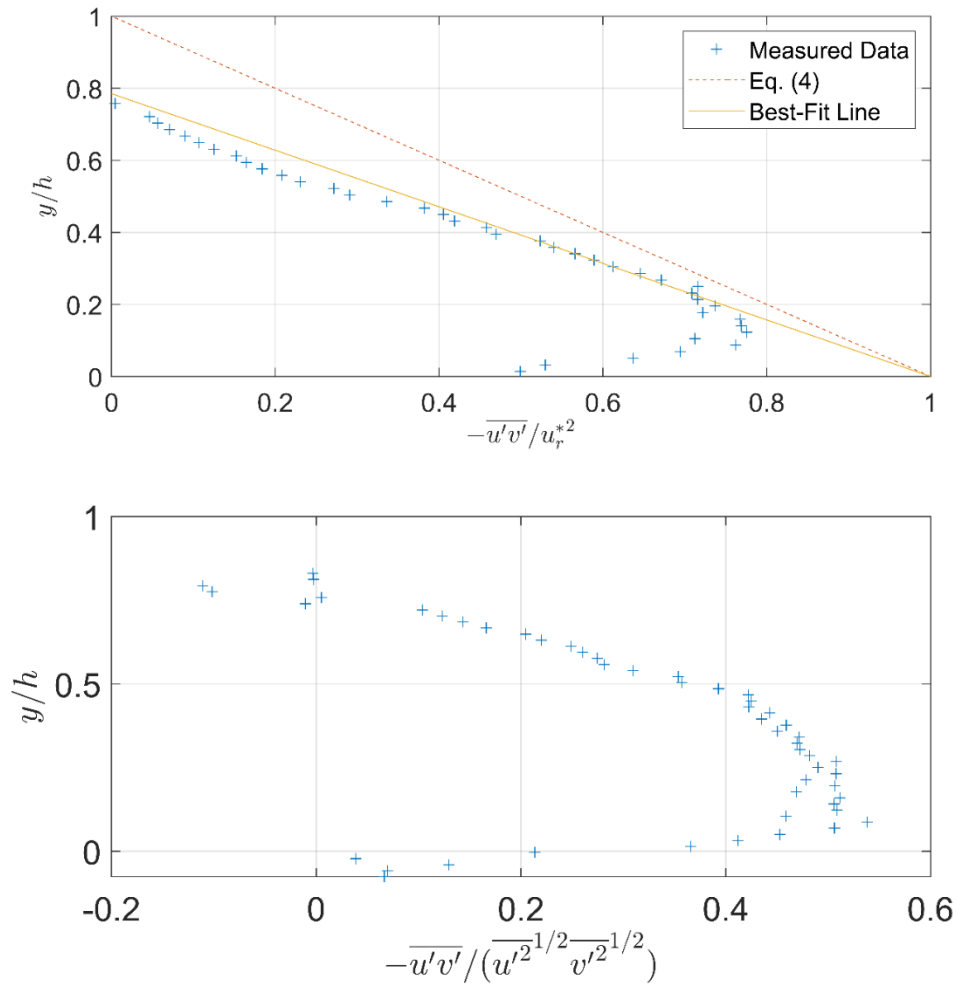
Figure 4.56 Measured Reynolds stress profile at location 4; τ_b = 1.02 N/m^2 (u_r^* = **0.0320** m/s), h = 24.7 mm

Figure 4.56 is a plot of $-\overline{u'v'}/u_r^{*2}$ versus y/h at location 4, with h = 24.7 mm. There is good correlation between the turbulence velocities u' and v'; the values of $R_{u'v'}$ away from the bed are between 0.4 and 0.5 (lower plot). The bed shear stress obtained by extrapolating the measured Reynolds stress to the bottom is 1.02 N/m^2.

Table 4.10 Summary of bed shear stress values (in N/m^2) obtained using various methods in case E

| Location	1	2	3	4
Bed Material	Sand	Sand	Rock	Rock
Water Surface Profile	M1	M1	N	N
τ_b (Eq. 1)	NA	NA	1.46	1.3
τ_b (Eq. 2)	NA	NA	NA	NA
τ_b (Eq. 3)	1.11	0.93	1.39	1.63
τ_b (Eq. 4)	0.86	0.67	1.07	1.02

Table 4.10 summarizes the bed shear stresses at the four measurement locations obtained using various methods. This case closely resembles the one discussed in Chen and Chiew (2003). The primary difference lies in the methodology used to determine y_0. As discussed earlier, in the case of Eq. (3), bed shear stress was determined by adjusting y_0 following the method in Ting and Kern (2022) instead of using a fixed value as in Chen and Chiew (2003). As a result, our results differ significantly from the findings by Chen and Chiew (2003). Table 4.10 shows that bed shear stress primarily depends on local water depth and bed roughness, with the bed shear stress adjusting to the roughness transition and reaching equilibrium much more quickly under an N curve after the roughness transition. As in the other cases, Eq. (4) generally produces bed shear stress values lower than the other methods.

5.   DISCUSSION

5.1   Effects of Bed Roughness and Water Depth on Bed Shear Stress

The main objective of this study was to investigate the effects of bed roughness and water surface profile on the bed shear stress in gradually varied flow due to a sudden change in bed roughness.

Loureiro et al. (2010) conducted experiments in closed conduit flow, specifically wind tunnel flow (in the absence of a free surface). They found that when transitioning from a rough bed to a smooth bed, the boundary layer develops near the bed immediately, and the bed shear stress attains equilibrium almost immediately.

Chen and Chiew (2003) conducted experiments in open-channel flows transitioning from a sand bed to a marble bed. They found that bed shear stress and equivalent roughness k_s change gradually as the flow goes through the transition.

This study observed that the development of bed shear stress through roughness transition was dependent on both the local water depth and bed roughness. In cases A and B, unlike the trend observed by Loureiro et al. (2010), different locations downstream of the transition did not exhibit the same bed shear stress, as the latter was influenced by the local water depth at each location. In both cases, the local water depth was higher near the transition than farther downstream, which is the reason why the bed shear stresses did not reach equilibrium immediately, in contrast to the closed conduit flow investigated by Loureiro et al. (2010). In case C, however, the bed shear stress obtained using the log law is similar at different locations in Channel 2 because the flow was uniform. Likewise, in case D, the location closer to the transition experiences higher bed shear stress compared with the downstream location because of the S3 profile. Therefore, the development of bed shear stress depends on the local water depth and may not reach equilibrium condition immediately after a roughness transition until the flow depth becomes uniform.

The experimental conditions in case E resemble those investigated by Chen and Chiew (2003), with the flow transitioning from an M1 profile to an N curve. However, this study yielded results different from the findings of Chen and Chiew (2003). In case E, the bed shear stress adjusted to the transition promptly and attained equilibrium because the flow depth was uniform in Channel 2. This contrasts with the trend observed by Chen and Chiew (2003), where the bed shear stress gradually increased along the channel after the transition. The different results in the two studies are related to the determination of the elevation of the theoretical bed on the rough bed.

5.2   Elevation of Theoretical Bed

Chen and Chiew (2003) took the height of the theoretical bed y_0 to be at the top of the rough bed and determined the values of u^* and k_s by fitting Eq. (3) to the measured velocities in the region where $y/h \leq 0.2$. Figure 3 of their paper shows that as x increases on the rough bed, the velocity u decreases adjacent to the bed but increases away from the bed (to maintain conservation of mass). This causes the velocity gradient du/dy to increase with x in the logarithmic region. The latter is related to the friction velocity u^* by Middleton and Southard (1984):

$$\frac{du}{dy} = \frac{u^*}{\kappa(y - y_0)} \tag{6}$$

Upon integration, Eq. (6) yields the familiar logarithmic law on a rough bed, which can also be represented by Eq. (3). Eq. (6) shows that for a given value of $y - y_0$ in the logarithmic region, the value of u^* must increase if du/dy increases. Eq. (3) then shows that the value of $\ln k_s - \kappa B$ must increase with x because u^* increases and u decreases with x. Hence, both u^* and k_s will increase with x if y_0 is held constant at different streamwise locations on the rough bed. This paper uses y_0 as a fitting parameter and does not employ a fixed value of y_0 along the channel, thus leading to different results from Chen and Chiew (2003). The difference in results between the two approaches is demonstrated in Appendix A using the measured data by Chen and Chiew (2003).

5.3 Effect of Channel Width to Water Depth Ratio

When Eq. (1) is applied to a smooth channel to calculate the bed shear stress, it assumes an even distribution of bed shear stress on both the smooth bed and side walls, yielding an overall average bed shear stress in a uniform flow. However, bed shear stress calculations based on measured velocity profiles depend on the local values where the velocity profile is taken (Auel et al., 2014). As a result, this thesis observed that the bed shear stress obtained using one equation is sometimes higher than that obtained using another equation. This discrepancy may be because Eq. (2), (3), and (4) are all based on the local values where the velocity profile is measured, which may not be uniform across the channel if secondary currents are present.

The channel-width-to-flow-depth aspect ratio plays a significant role in determining the flow patterns. In narrow channels, where the width-to-depth ratio is small (typically 4–5), the highest velocities are concentrated around the centerline of the channel (see Figure 3 in Auel et al., 2014). Narrow channels exhibit the presence of secondary currents near the side walls, resulting in complex three-dimensional flow patterns (Auel et al., 2014). These flow characteristics also have notable effects on the turbulence distributions and Reynolds stress. Therefore, the values of bed shear stress obtained using Eq. (2), (3), and (4) depend on where the velocity profile is measured in the channel, whether it is in the middle or near the side wall. Since the channel used in this study was narrow, it was likely that the velocity profiles obtained in all five cases were affected by secondary currents to some degree. This observation is reflected in the results, as different methods yielded somewhat different bed shear stress values.

5.4 Reynolds Stress

A recurring pattern observed in this study is that the Reynolds stress method consistently underestimates the bed shear stress when compared with the other methods. This may also be attributed to the influence of secondary currents in narrow channels (refer to Figure 15 in Auel et al., 2014). It was suspected in this study that, since all the experiments involved narrow channels, measured Reynolds stress distributions would deviate from the linear trend due to secondary currents as observed by Auel et al. (2013), consequently leading to an underprediction of bed shear stress in comparison with the other methods.

6.   SUMMARY AND CONCLUSIONS

The following conclusions can be drawn from this study:

1. The value of the k_s/d_{90} ratio depends on the h/d_{90} ratio. An increasing trend was observed in the k_s/d_{90} ratio as the h/d_{90} ratio increases in the uniform flow experiments until the k_s/d_{90} ratio reaches a value between 2 and 2.5 when the h/d_{90} ratio is above 15.
2. Significant differences were observed in the bed shear stresses calculated using the depth-slope method and the mean velocity profile when dealing with narrow channels and supercritical flows.
3. This study found that in open-channel (free-surface) flow, the development of the bed shear stress was related to both the water surface profile and bed roughness. The new boundary layer started to develop immediately, but the velocity profile was not fully established for some distance downstream. In both rough-to-smooth (RTS) and smooth-to-rough (STR) transitions, the bed shear stress development closely followed the variation in local water depth, ultimately reaching equilibrium when the local water depth became uniform.
4. It was found that the choice of displacement height on a rough bed strongly affected the value of bed shear stress obtained using the logarithmic law, and thus the development of bed shear stress in STR transitions.

7. RECOMMENDATIONS FOR FUTURE WORK

This study has focused on the development of the mean velocity profile and bed shear stress near roughness transitions. There is still much to be learned regarding the profiles of Reynolds stress and turbulence intensities. Additional studies are needed to gain a deeper understanding of these flow parameters. Furthermore, the implementation of direct methods for measuring bed shear stress on the smooth bed in the transition zone could provide additional insights into flow dynamics during the transitional phase.

8. REFERENCES

Akan, A. O. (2006). *Open Channel Hydraulics*, 1st Edition, Butterworth-Heinemann, 376 pages.

Antonia, R. A., and Luxton, R. E. (1972). "The response of a turbulent boundary layer to a step change in surface roughness. Part 2. Rough-to-smooth." *Journal of Fluid Mechanics*, 63(4), 737-757, https://doi.org/10.1017/S002211207200045X

Auel C., Albayrak I., and Boes R. M. (2014). "Turbulence characteristics in supercritical open channel flows: effects of Froude number and aspect ratio." *Journal of Hydraulic Engineering*, 140(4), https://doi.org/10.1061/(ASCE)HY.1943-7900.0000841.

Camenen, B., Bayram, A., and Larson, M. (2006). "Equivalent roughness height for plane bed under steady flow." *Journal of Hydraulic Engineering*, 132:1146-1158. https://doi.org/10.1061/(ASCE)0733-9429(2006)132:11(1146)

Chen, X., and Chiew, Y. M. (2003). "Response of velocity and turbulence to sudden change of bed roughness in open-channel flow." *Journal of Hydraulic Engineering*, 129(1), 35-43, https://doi.org/10.1061/(ASCE)0733-9429(2003)129:1(35).

Cheng, N-S (2011). "Revisited Vanoni-Brooks sidewall correction." *International Journal of Sediment Research*, 26, 524-528.

Hino, M., Kashiwayanagi, M., Nakayama, A., and Hara, T. (1983). "Experiments on the turbulence statistics and the structure of a reciprocating oscillatory flow." *Journal of Fluid Mechanics*, 131, 363-400, https://doi.org/10.1017/S0022112083001378.

INSIGHT 4G™ User's Guide (2019). Insight 4G Global Imaging, Acquisition, Analysis and Display Software. TSI Incorporated.

Jensen, B. L., Sumer, B. M., and Fredsøe, J. (1989). "Turbulent oscillatory boundary layers at high Reynolds numbers." *Journal of Fluid Mechanics*, 206, 265-297, https://doi.org/10.1017/S0022112089002302.

Kadivar, M., Tormey, D., and McGranaghan, G. (2021). "A review on turbulent flow over rough surfaces: Fundamentals and theories." *International Journal of Thermofluids*, 10, 1000777.

Kamphuis, J. W. (1974). "Determination of sand roughness for fixed beds." *Journal of Hydraulic Research*, https://doi.org/10.1080/00221687409499737.

Kiger, K. (2015). "PIV basics: Correlation." In SEDITRANS summer school on measurement techniques for turbulent open-channel flows. http://www.civil.ist.utl.pt/~ruif/SUMMER_SCHOOL/presentations/PIV_basics_correlation_final.pdf .

Lee, C-H (2018). "Rough boundary treatment method for the shear-stress transport k - ω model." *Engineering Applications of Computational Fluid Mechanics*, doi.org/10.1080/19942060.2017.1410497.

Li, M., de Silva, C. N., Rouhi, A., Baidya, R., Chung, D., Marusic, I., and Hutchins, N.

(2019). "Recovery of wall-shear stress to equilibrium flow conditions after a

rough-to-smooth step change in turbulent boundary layers." *Journal of Fluid Mechanics*, 872, 472-491, https://doi.org/10.1017/jfm.2019.351.

Loureiro, J. B. R., Sousa, F. B. C. C., Zotin, J. K. Z., and Silva Freire, A. P. (2010). "The distribution of wall shear stress downstream of a change in roughness." *International Journal of Heat and Fluid Flow*, 31, 785-793.

Middleton, G. V., and Southard, J. (1984). "Mechanics of Sediment Movement." *SEPM for Sedimentary Geology Short Course Number 3*, 2nd edition.

Nezu, I., Tominaga, A., and Nakagawa, H. (1993). "Field measurements of secondary currents in straight rivers." *Journal of Hydraulic Engineering*, 119(5), 598-614.

O'Donoghue, T., Davies, A. G., and Bhawanin, M. (2021). "Measurement and prediction of bottom boundary layer hydrodynamics under modulated oscillatory flows." *Coastal Engineering*, 169, 103954.

Rathore, V., Penna, N., Dey, S. and Gaudio, R. (2022). "Response of open-channel flow to a sudden change from smooth to rough bed." *Environmental Fluid Mechanics*, 22, 87-112, https://doi.org/10.1007/s10652-021-09830-5.

Spalding, D. B. (1961). "A single formula for the law of the wall." *Journal of Applied Mechanics*, 28(3), 455-458, https://doi.org/10.1115/1.3641728.

Sumer, B. M., and Fuhrman, D. R. (2020). *Turbulence in coastal and civil engineering* (Vol. 51). World Scientific.

Ting, F. C. (2006). "Large-scale turbulence under a solitary wave." *Coastal Engineering*, 53(5-6), 441-462,

Ting, F. C. K., and Kern, G. (2022). "Finding the bed shear stress on a rough bed using the log law." *Journal of Waterway, Port, Coastal, and Ocean Engineering*, 148(4), 04022008, https://doi.org/10.1061/(ASCE)WW.1943-5460.0000707

Van der A, D., O'Donoghue, T., Davies, A., and Ribberink, J. (2011). "Experimental study of the turbulent boundary layer in acceleration-skewed oscillatory flow." *Journal of Fluid Mechanics*, 684, 251-283, https://doi:10.1017/jfm.2011.300.

9. APPENDIX A. EFFECT OF DISPLACEMENT HEIGHT

Chen and Chiew (2003) took the displacement height y_0 to be at the top of the rough (marble) bed (i.e., $y_0 = 0$) and determined the values of u^* and k_s by fitting Eq. (3) to the measured velocities in the region where $y/h \leq 0.2$. The mean velocity profiles at different locations for case C shown in Figure 3 of their paper are reproduced here in Figure A1. It shows that as x increases on the marble bed, the mean velocity u decreases adjacent to the bed but increases away from the bed (to maintain conservation of mass).
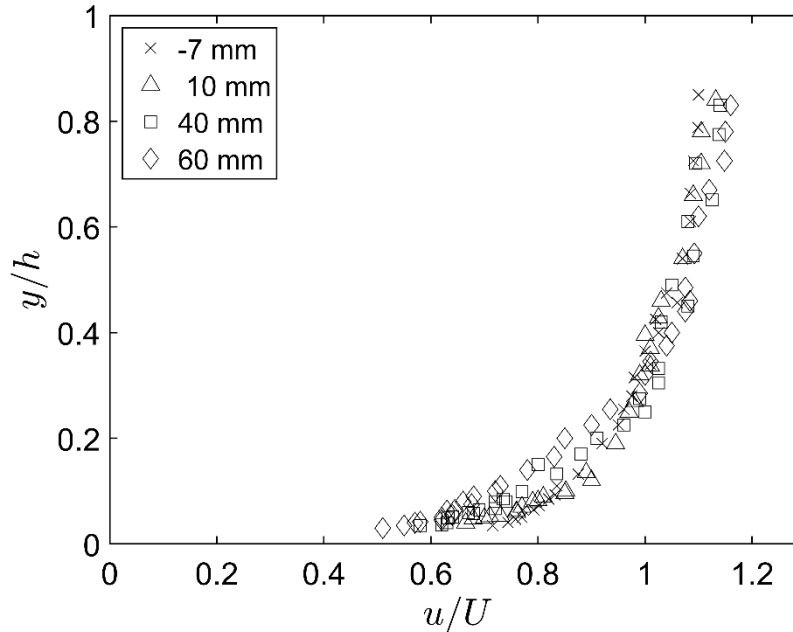
Figure A1 Horizontal mean velocity profiles at different locations in case C of Chen and Chiew (2003)

Figure A2 compares the variations of k_s and u_* with x obtained using two different methods. When y_0 is held fixed at $y = 0$, both k_s and u_* increase gradually with x. The values of k_s and u_* increase from 0.11 cm and 1.16 cm/s, respectively, at $x = 10$ cm to 0.91 cm and 1.63 cm/s, respectively, at $x = 60$ cm. These results are like those shown in Figures. 6 and 7 of Chen and Chiew (2003). However, if k_s is held fixed at the mean diameter of the marbles (1.12 cm) and the value of y_0 is allowed to vary, Figure A2 shows that the value of u^* decreases slightly from 1.8 to 1.7 cm/s between $x = 10$ and 60 cm. In Figure A2, the value of k_s for the sand bed before the transition is taken as 2 mm or twice the mean bed roughness height (Kamphuis, 1973). The above analysis shows that holding the value of y_0 constant may cause the values of k_s and u^* to vary in a pre-determined manner under certain flow conditions.
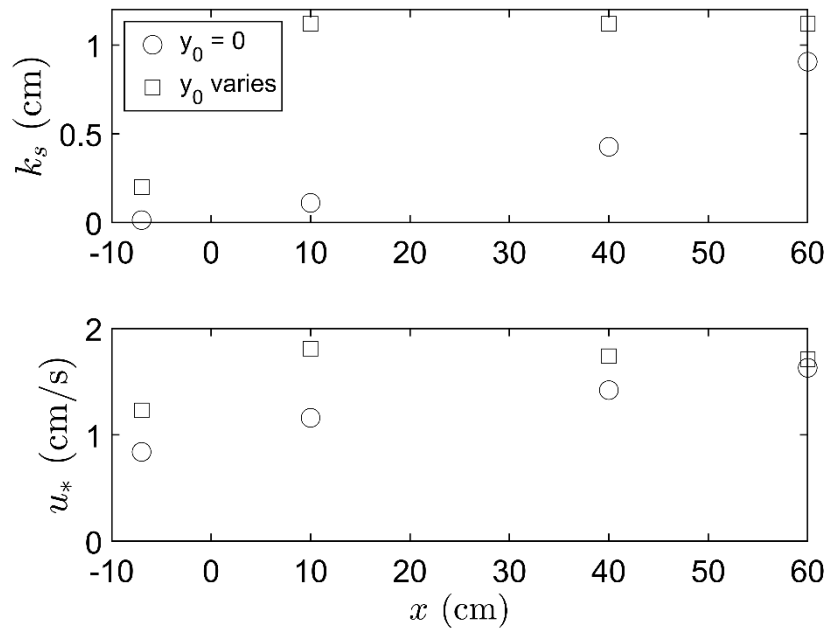
Figure A2 Variations of equivalent roughness height and friction velocity with channel distance in case C of Chen and Chiew (2003)